IRAQI JOURNAL OF APPLIED PHYSICS

The *Iraqi Journal of Applied Physics (IJAP)* is a peer reviewed journal of high quality devoted to the publication of original research papers from applied physics and their broad range of applications. IJAP publishes quality original research papers, comprehensive review articles, survey articles, book reviews, dissertation abstracts in physics and its applications in the broadest sense. It is intended that the journal may act as an interdisciplinary forum for Physics and its applications. Innovative applications and material that brings together diverse areas of Physics are particularly welcome. Review articles in selected areas are published from time to time. It aims to disseminate knowledge; provide a learned reference in the field; and establish channels of communication between academic and research experts, policy makers and executives in industry, commerce and investment institutions. IJAP is a quarterly specialized periodical dedicated to publishing original papers, letters and reviews in: Applied & Nonlinear Optics, Applied Mechanics & Thermodynamics, Digital & Optical Communications, Electronic Materials & Devices, Laser Physics & Applications, Plasma Physics & Applications, Quantum Physics & Spectroscopy, Semiconductors & Optoelectronics, Solid State Physics & Applications, Alternative & Renewable Energy, and Environmental Science & Technology.

ISSN (Print): 1813-2065, ISSN (Online): 2309-1673

Editorial Office:
P. O. Box 88052, Baghdad 12631, IRAQ
Website: www.iraqiphysicsjournal.com
Emails: info@iraqiphysicsjournal.com, editor_ijap@yahoo.co.uk, ijap.editor@gmail.com,

SPONSORED AND PUBLISHED BY
AMERICAN QUALITY FOR SCIENTIFIC PUBLISHING INC.
1479 South De Gaulle Ct, Aurora, CO 80018, United States

IRAQI JOURNAL OF APPLIED PHYSICS

ISSN (Print): 1813-2065, ISSN (Online): 2309-1673

INSTRUCTIONS TO AUTHORS

CONTRIBUTIONS

Contributions to be published in this journal should be original research works, i.e., those not already published or submitted for publication elsewhere, individual papers or letters to editor.
Manuscripts should be submitted to the editor at the mailing address:

Iraqi Journal of Applied Physics, Editorial Board, P. O. Box 88052, Baghdad 12631, IRAQ
Website: www.iraqiphysicsjournal.com
Email: info@iraqiphysicsjournal.com, editor_ijap@yahoo.co.uk, ijap.editor@gmail.com

MANUSCRIPTS

Two hard copies with soft Word copy on a CD or DVD should be submitted to Editor in the following configuration:

- **One-column** Double-spaced one-side A4 size with 2.5 cm margins of all sides
- Times New Roman font (16pt bold for title, 14pt bold for names, 12pt bold for headings, 12pt regular for text)
- Manuscripts presented in English only are accepted.
- English abstract not exceed 150 words
- 4 keywords (at least) should be maintained on (PACS preferred)
- Author(s) should express all quantities in SI units
- Equations should be written in equation form (*italic* and symbolic) NOT in plain text
- Tables and Figures should be separated from text and placed in new pages after the references
- Charts should be indicated by the software used for generating them (e.g., Excel, MATLAB, Grapher, etc.)
- Figures and diagrams can be submitted in original colored forms for assessment and they will be returned to authors after provide printable copies
- Only original or high-resolution scanner photos are accepted
- For electronic submission, articles should be formatted with MS-Word software.

AUTHOR NAMES AND AFFILIATIONS

It is IJAP policy that all those who have participated significantly in the technical aspects of a paper be recognized as co-authors or cited in the acknowledgments. In the case of a paper with more than one author, correspondence concerning the paper will be sent to the first author unless staff is advised otherwise.
Author name should consist of first name, middle initial, last name. The author affiliation should consist of the following, as applicable, in the order noted:
- Company or college (with department name or company division), Postal address, City, Governorate or State, zip code, Country name, contacting telephone number, and e-mail

REFERENCES

The references should be brought at the end of the article, and numbered in the order of their appearance in the paper. The reference list should be cited in accordance with the following examples:
[1] X. Ning, R. Benford and M.R. Lovell, "On the Sliding Friction Characteristics of Unidirectional Continuous FRP Composites", *J. Tribol. Func. Mater.*, 124(1) (2002) 5-13.
[2] M. Barnes, "Stresses in Solenoids", *J. Appl. Phys.*, 48(5) (2001) 2000–2008.
[3] J. Jones, **"Contact Mechanics"**, Cambridge University Press (Cambridge, UK) (2000), Ch.6, p.56.
[4] Y. Lee, S.A. Korpela and R. Horne, "Structure of Multi-Cellular Natural Convection in a Tall Vertical Annulus", Proceedings of 7th International Heat Transfer Conference, U. Grigul et al., eds., Hemisphere (Washington DC), 2 (1982) 221–226.
[5] M. Hashish, "Waterjet Technology Development", High Pressure Technology, PVP-Vol. 406 (2000) 135-140.
[6] D.W. Watson, "Thermodynamic Analysis", ASME Paper No. 97-GT-288 (1997).
[7] C.Y. Tung, "Evaporative Heat Transfer in the Contact Line of a Mixture", Ph.D. thesis, Rensselaer Polytechnic Institute, Troy, NY (1982).

PROOFS

Authors will receive proofs of papers and are requested to return one corrected copy as a WORD file on a compact disc (CD) or by email. New materials inserted in the original text without Editor's permission may cause rejection of paper unless the handling editor is informed.

COPYRIGHT FORM

Author(s) will be asked to sign the IJAP Copyright Form and hence transfer copyrights of the article to the Journal soon after acceptance of it. This will ensure the widest possible dissemination of information.

OFFPRINTS

Authors will receive electronic offprint free of charge and any additional reprints can be ordered.

SUBSCRIPTION AND ORDERS

Annual fees (4 issues per year) of subscription are:
50 US$ for individuals inside Iraq; **200** US$ for institutions inside Iraq;
100 US$ for individuals abroad; **300** US$ for institutions abroad.

IJAP in 19 years

By
Oday A. Hammadi
Editor-In-Chief, IJAP

In August 2004, the Iraqi Journal of Applied Physics, abbreviated as IJAP, was established and registered with ISSN 1813-2065 as a scientific periodical sponsored and published by the Iraqi Society for Alternative and Renewable Energy Sources and Techniques (I.S.A.R.E.S.T.) in Baghdad, Iraq. IJAP was started to publish articles in nine disciplines of applied physics; Applied & Nonlinear Optics, Applied Mechanics & Thermodynamics, Digital & Optical Communications, Electronic Materials & Devices, Laser Physics & Applications, Plasma Physics & Applications, Quantum Physics & Spectroscopy, Semiconductors & Optoelectronics, Solid State Physics & Applications. In January 2005, the first issue of IJAP was released. That issue included eight articles, four in Arabic and four in English. This was the last time to publish articles in Arabic. The first Editorial Board of IJAP contained of Dr. W.K. Hamoudi as the Editor-In-Chief (EIC), Dr. R.A. Ismail, Dr. D.N. Raouf, Dr. R.A. Khamis, and Mr. O.A. Hammadi as the Managing Editor. The first Advisory Board of IJAP contained fourteen members, twelve of them were from Iraqi universities and two from foreign universities. All editorial works were performed using the postal address 55159, Baghdad 12001, Iraq while online correspondences were carried out using two Yahoo email addresses; editor_ijap@yahoo.co.uk and irq_appl_phys@yahoo.com.

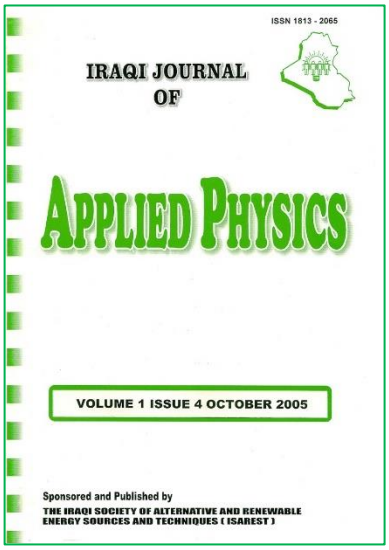

Soon later, the Advisory Board of IJAP was reconfigured to contain sixteen members, eight of them were from Iraqi universities while the other were from foreign institutions. This was the first time for a scientific periodical in Iraq to have advisory board with 50% of its members are from foreign institutions. This gave a big support for IJAP to receive manuscripts from foreign authors as well. The manuscript entitled "Key mechanisms of the nonlinear amplification: physics and applications" was received from the United Kingdom and published in the second issue of the first volume released in June 2005. By April 2005, a new postal address was registered for IJAP as P. O. Box 55259, Baghdad 12001, Iraq. IJAP was tightly concerned to announce for the scientific activities of I.S.A.R.E.S.T. By December 2005, IJAP has published four issues with a total of 20 articles and 136 pages and two more Advisors from foreign institutions have joined the Advisory Board of IJAP.

In 2006, Iraq has witnessed dramatic events that led to the deterioration of the general situation in the country, and this greatly affected the work of institutions in general, including the IJAP. However, the work continued to release two issues only with 15 articles and 70 pages. As the life in Iraq was approximately stopped over 2007, IJAP has published four issues, each of them included one review article, with 171 pages in total. These reviews have saved IJAP from that difficult situation.

In 2008, some kind of recovery was observed in Iraq and IJAP has published four issues with 22 articles and 173 pages. Also, IJAP has published two indexes on the subjects and authors within 2005-2008. These indexes have appeared in the last issue of volume 4 released in December 2008. This was the first time to see such indexes in a scientific periodical journal in Iraq and this will be a main part of the last issue of each volume of IJAP. In 2009, three new advisors from foreign institutions have joined the Advisory Board of IJAP, which has published three issues with 20 articles and 168 pages. In 2010, Dr. D.N. Raouf has been named as the EIC and IJAP has published four issues with 21 articles and 168 pages. In 2011, IJAP has published three issues with 16 articles and 140 pages. In 2012, Dr. R.A. Khamis has been named as the Editor-In-Chief and IJAP has published four issues with 20 articles and 160 pages.

In 2013, Dr. R.A. Ismail has been named as the EIC and the Editorial Board has been extended to include 8 members. The three new members were Mr. H.M. Mikhlif named as the Associate Editor, Miss. R.A. Markub named as the Middle East Coordinator, and Dr. IF. Ramley named as the Industrial Relation Coordinator. By January 2013, IJAP has released its own website www.iraqiphysicsjournal.com that was granted by Mr. Ahmed Farid and designed by Mr. Wisam M. Rahim. Therefore, IJAP has started to use new email addresses such as info@iraqiphysicsjournal.com in addition to the Yahoo emails. These procedures have transferred the work of IJAP to a higher level as the total number of articles published in 2013 was 43 with 157 pages. In May 2013, IJAP was honored in the Iraqi Science Day as the best scientific journal and a certificate was received from the Iraqi Ministry of Higher Education and Scientific Research.

In 2014, Dr. W.K. Hamoudi has been named as the EIC for the second time. The Editorial Board has decided to release an electronic (online) copy of IJAP, which was registered as ISSN 2309-1673. IJAP has published four issues with 39 articles and 177 pages, which was the highest within 2005-2014. In April 2014, six advisors were selected to join the Editorial Board of IJAP to include 14 members, while the Advisory Board contained 19 members, 12 of them (i.e., 63%) were from foreign institutions. As well, the Editorial Board has decided to add a new discipline (Computers and Networks) to the disciplines dedicated by IJAP. In May 2014, IJAP was honored again in the Iraqi Science Day as the best scientific journal and a certificate was received from the Iraqi Ministry of Higher Education and Scientific Research.

In December 2014, the Editorial Board of IJAP has lost its member R.A. Markub, whose name was highlighted with black in the first issue of volume 11 released in January 2015. In March 2015, the Editorial Board has decided to add new discipline (Alternative and Renewable Energy) to the disciplines dedicated by IJAP. In September 2015, three new advisors from the United States have joined the Advisory Board of IJAP. During 2015, IJAP has appeared in many online libraries and databases over the world as the number of articles received from foreign countries continued to increase. By December 2015, IJAP has published the maximum number of article (47) with total pages of 168. This was a real achievement. However, IJAP was excluded from the qualifications for the Iraqi Science Day because it was not published an Iraqi academic institution!

In 2016, Dr. R.A. Ismail has been named as the EIC for the second time. In April 2016, Dr. R.A. Khamis has replaced Dr. Ismail as the EIC due to some health difficulties and this was the second time for Dr. Khamis to be the EIC of IJAP. By December 2016, IJAP has published 28 articles with 154 pages.

In 2017, the first issue of volume 13 of IJAP was not released due to some administrative problems prevented the Editorial Board from preparing it. Also, IJAP has witnessed a decrease in the number of received manuscripts and hence published articles. By December 2017, IJAP has published three issues only with 11 articles and 132 pages. The administrative problems have continued during 2018 to cause IJAP to release two issues only of volume 14 with 11 articles and 156 pages. In April 2018, the Advisory Board of IJAP has lost Dr. M.M. Elias.

In 2019, the administrative work in IJAP was sufficiently reformed and four issues of volume 15 were released with 28 articles and 168 pages. In 2020, the volume 16 including 4 issues was released with 20 articles and 168 pages. IJAP has started the suggestion process for Scopus index as all requirements were prepared. In 2021, IJAP has released 4 issues of volume 17 with 23 articles and 132 pages. In July 2021, the suggestion of IJAP was accepted to be indexed by Scopus. This achievement would strongly introduce IJAP to the community of physics and their applications in Iraq and Middle East.

In January 2022, the Editorial Board has decided to exclude the discipline of Computers and Networks from the disciplines dedicated by IJAP as no enough manuscripts were received during 2014-2021. As well, IJAP has started the suggestion process for Web-Of-Science index. In August 2022, I.S.A.R.E.S.T., the sponsor and publisher of IJAP, has been canceled according to an official decision and IJAP Editorial Board has been informed to change its publisher within 3 months or IJAP would be canceled too. This decision posed a real challenge to the work of IJAP. Immediately, the Editorial Board began communicating with many parties to find an alternative publisher for I.S.A.R.E.S.T. Finally, the Editorial Board of IJAP concluded an agreement with a U.S. publishing incorporation to become the new publisher of IJAP for a renewable period of one year, while IJAP retained a self-sponsoring capacity. Also, Dr. O.A. Hammadi has been named as the EIC starting from January 2023 and the Editorial Board was reformed to include 7 members only while the other 6 members were appreciated for their contributions during 2014-2022. As well, the Advisory Board was reformed to include 17 members from foreign institutions and all dismissed members were appreciated for their contributions.

 ISSN (print) 1813-2065, (online) 2309-1673

IRAQI JOURNAL OF APPLIED PHYSICS
Vol. 19, No. 1, January-March 2023, pp. 5-12

Characterization of Electrochromism and Photoelectrochromism of N-Doped TiO_2 and Co_3O_4 Thin Films Prepared by DC Reactive Magnetron Sputtering: Comparative Study

Noor Alhuda H. Hashim
Firas J. Kadhim
Zinah S. Abdulsattar

Department of Physics, College of Science, University of Baghdad, Baghdad, IRAQ

In the present work, dc reactive magnetron sputtering technique was employed to deposit the layers of elelctrochromic and photoelectrochromic. In multilayer configuration, a nitrogen-doped titanium dioxide thin film as electrochromic layer (EC) was deposited on indium-tin oxide (ITO) as conducting substrate, and cobalt oxide as ion storage layer (IS) was deposited onto the EC layer. In single layer configuration, cobalt oxide as (EC) layer was deposited on ITO substrate. In both configurations, sodium hydroxide (NaOH) was used as electrolyte solution, while platinum (Pt) sheet was used as anode electrode. Photoelectrochromic device (PECD) with multilayer configuration (glass/ITO/N-dopedTiO_2/Co_3O_4/NaOH/Pt) and electrochromic device (ECD) with single layer configuration (glass/ITO/Co_3O_4/NaOH/Pt) were synthesized and characterized by UV-visible spectroscopy. It was found that the transmittance varied from 50 to 16.5% within 4 s of response time for single layer configuration and from 54 to 26.1% within 3 min of response time for multilayer configuration.

Keywords: Electrochromism; Photoelectrochromic devices; TiO_2; Co_3O_4
Received: 29 November 2022; **Revised:** 12 December; **Accepted:** 19 December 2022

1. Introduction

In the last years, smart windows have gained considerable attention by the international scientific community due to significant energy savings [1]. The phenomenon of color change by chromic materials due to external stimuli, such as electric field, pressure, light, ions, solvent, etc., is called chromism. Chromic materials change the optical properties like transmission, reflectance, absorption, and emittance due to these external stimuli [2]. Electrochromism is the phenomenon exhibited by electrochromic materials that change color when an electric potential is applied [3-5]. While Photoelectrochromism is also the phenomena of changing color of chemical compounds induced by electrochemical oxidation and reduction, under the effect of a variation an electric voltage and/or in the intensity of a light radiation [6]. This chromic effect can be put to practical use in the design of "Smart Window", smart windows that can control the amount of light passing through it based on EC materials [7]. These EC materials are mainly classified into two categories: anodic and cathodic materials [8,9], anodic EC materials, which are coloring under ion extraction "oxidation process" and cathodic EC materials, which are coloring under ion insertion "reduction process" [10]. The inorganic EC materials have a good electrochemical reversibility, chemical stability and high coloring efficiency where organic EC materials display poor durability [11-13]. Titanium dioxide (TiO_2) is an n-type semiconducting material that has superior properties such as non-toxic, high stability and strong oxidizing agent (with large surface area) has very high photocatalytic activity [14-16]. Due to these properties this material has been applied in various applications such as solar cells, sensors, environmental remediation and as cathodic material of electrochromic devices [17]. As titanium dioxide does not absorb visible light, there is several methods to overcome this problem including the doping with non-metallic elements such as nitrogen [18-19]. Cobalt oxide (Co_3O_4) is one of the most important metal oxides, p-type antiferromagnetic semiconductor with direct band gap between 1.48-2.19 eV [20,21]. This oxide has a wide range of applications due optical, magnetic,

electronic, chemical, electrochemical and mechanical properties [22-24]. The preparation and characterization of cobalt oxides Co_3O_4 have been extensively studied due to attractive applications in solar cells, catalysis, batteries, corrosion protective coatings, magnetic nanostructures and magnetic storage systems, electrochromic EC devices. Co_3O_4 has been reported to be a good anodic coloration material for the EC application [25,26]. There are several deposition techniques to prepare oxide thin films such as sputtering, spray pyrolysis, chemical vapor deposition, pulsed laser deposition, electrophoretic deposition, sol-gel process, etc. [27-29]. DC reactive magnetron sputtering technique was employed for the preparation of the EC thin films because it provides high purity, high homogeneity and good control of the structural phase of the deposited film by controlling the gas mixing ratio [30].

In this work, the layers of electrochromic and photoelectrochromic device based on N-doped TiO_2 and Co_3O_4 oxides are prepared by dc reactive magnetron sputtering technique. The optical and structural characteristics of each layers will be studied and optimized to synthesis single layer configuration for ECD and multi-layers configuration for PECD devices and compared coloring-bleaching response for each configurations.

2. Experimental Details

Cobalt oxide was prepared by using dc reactive magnetron sputtering and more information about the preparing conditions of cobalt oxide may be obtained elsewhere [31,32]. A high-purity titanium sheet with 60 mm diameter and 0.5 mm thickness was mounted on the cathode and glass substrate placed on a heat sink was placed on the anode. The optimum preparation conditions include discharge voltage of 2.5 kV and discharge current of 45 mA, while the distance between the target and the substrate was fixed at 4 cm. N-doped TiO_2 thin films were prepared using different Ar:O_2:N_2 gas mixing ratios (40:40:20, 60:30:10: 43:42:15 and 76:19:5) and deposition time of 3 hours.0

Co_3O_4 thin film was deposited on ITO substrate to synthesize the ECD with single layer configuration (glass/ITO/Co_3O_4/NaOH/Pt). The single-layer electrode as the anode and Pt sheet as the cathode were dipped in an electrolyte solution with concentration of 0.5 M NaOH. The electrodes were connected to a 2V dc power supply and in bleached state, the polarity of the electrodes was reversed. The PECD with multilayer configurations (glass/ITO/N-doped TiO_2/Co_3O_4/NaOH/Pt) was synthesized. Firstly, N-doped TiO_2 was deposited on ITO as EC layer, then a layer of Co_3O_4 was deposited on EC layer as IS layer. The multilayer structure as the cathode electrode and Pt as the anode electrode were immersed in an electrolyte solution with concentration of 1 M NaOH. These electrodes were connected to a 5V dc power supply under xenon light irradiation. The colored and bleached states could be obtained when the polarity of voltage is reversed. Figure (1) shows a schematic diagram of the experimental system of PECD with multilayer configuration, which is the same system used for the ECD with single-layer configuration but without light source.

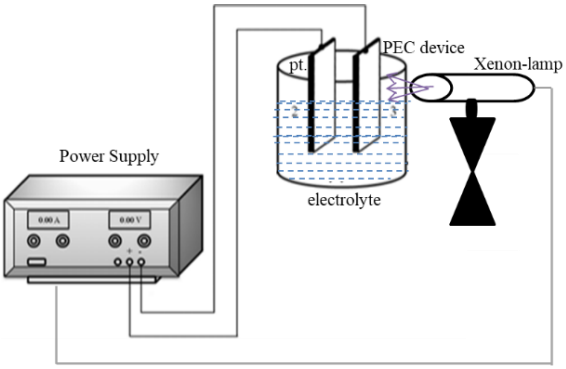

Fig. (1) Schematic diagram of the experimental system of PECD with multilayer configuration

3. Results and Discussion

The crystal structure of the Co_3O_4 thin film prepared using Ar:O_2 gas mixing ratio of 60:40 was investigated by an X-ray Shimadzu Diffractometer using Cu-Kα source (1.54Å). The XRD pattern shows the diffraction peaks which indicate that the crystalline structure of these films constitutes a single phase of Co_3O_4 with a spinel-type structure. The XRD pattern in Fig. (2) shows a major peak at about 37° corresponding to crystal plane of (311). This peak has the highest intensity, indicating the oriented growth of the sample in the (311) direction. Six peaks observed at 31.5°, 37.1°, 38.7°, 45.0°, 55.9°, 59.6°, 65.4° and 77.7° are corresponding to (220), (311), (222), (400), (422), (511), (440) and (533) planes, which indicate the formation of pure Co_3O_4 [33].

Figure (3) shows the XRD pattern of N-doped TiO_2 thin film prepared using Ar:O_2:N_2 gas mixing ratio of 40:40:20 after 3 hours of deposition time with heat sink under the substrate. The diffraction peaks observed at 22.4°, 38.5°, 53.1°, 63.2°, 70.7°,76.3° and 77.9° are assigned to A(101), A(104), A(105), A(204), A(220), A(215) and A(206) planes of anatase phase, respectively. Other peaks observed at 35.3° and 42.1° are corresponding to TiN(111) and TiN(200) according to JCPDS card no. 38-1420 [34]. The diffraction peaks assigned at 36.2° and 40.3° corresponding to crystal planes (101) and (111) were confirmed for the rutile phase according to JCPDS card no. 88-1175 [35]. No peaks belonging to other compounds or impurities were observed, which can be considered as an advantage of the sputtering technique used in this work and the fine control of gas mixing ratio.

 ISSN (print) 1813-2065, (online) 2309-1673

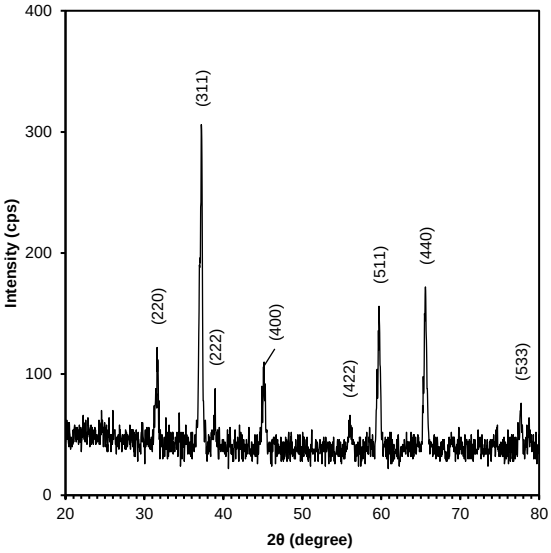

Fig. (2) XRD pattern of Co_3O_4 thin film using gas mixing ratio 60:40

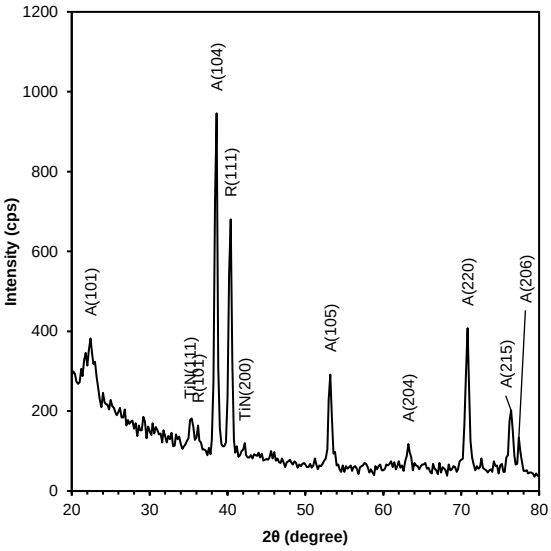

Fig. (3) XRD pattern of N-doped TiO_2 thin film prepared using gas mixing ratio of 40:40:20

The nanoparticle size of the synthesized nanostructured layers were studied by field-emission scanning electron microscopy (FE-SEM). The image in Fig. (4a) with scale of 500 nm shows that the Co_3O_4 nanoparticles are spherical with minimum particle size of 37.32 nm, while the image in Fig. (4b) with the same scale shows the N-doped TiO_2 nanoparticles with minimum particle size of 28.09 nm. The aggregated particles indicates good connectivity between these nanoparticles. The nanoparticles can form complex assemblies referred as aggregates, which typically consist of particles in the nanoscale (5-50 nm). They are held together by weak forces arising from the van der Waals force, which leads to an electrostatics effect through the residual charge of the structure. Ambient humidity plays an important role in determining the fundamental mechanical response and dynamics of these assemblies [36]. The FE-SEM image indicates that the prepared nanoparticles are uniformly distributed. This type of morphology is beneficial to use these nanostructures for EC and PEC devices and supercapacitor application [37,38].

Figure (5) shows the FTIR spectrum recorded in the range 400-4000 cm^{-1} for the Co_3O_4 sample prepared using gas mixing ratio of 60:40 after deposition time of 1 hour. Two strong peaks were observed, the first at 572.82 cm^{-1} was assigned to Co-O stretching vibration mode, in which Co^{3+} is octahedrally coordinated, and the second peak at 663.47 cm^{-1} was assigned to bridging vibration, in which Co^{2+} is tetrahedrally coordinated [39]. This further confirms the formation of Co_3O_4. The peaks seen at 1571.88 and 3436.91 cm^{-1} are ascribed to the OH stretching and bending modes, respectively, of water adsorbed by the Co_3O_4 sample. The peaks at 2408.93 and 1423.37 cm^{-1} are characteristic of asymmetric vibrations of CO_2 and CO^{-2}, respectively, which were also adsorbed from the air [40].

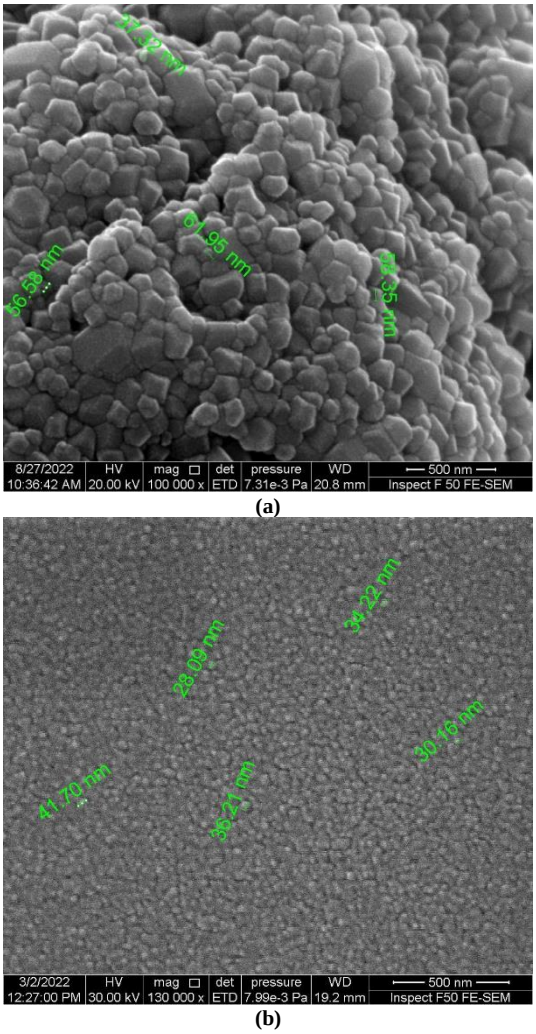

Fig. (4) FE-SEM images of (a) Co_3O_4 sample prepared using 60:40 gas mixing ratio, and (b) N-doped TiO_2 sample prepared using 40:40:20 gas mixing ratio

For the N-doped TiO_2 sample prepared using gas mixing ratio of 40:40:20 after deposition time of 3 hours, the peak seen at 408.91 cm^{-1} is assigned to Ti-O-Ti bonds in the TiO_2 lattice, while the bands ascribed to Ti-O symmetric and asymmetric stretching vibration modes were observed around 447 and 667 cm^{-1}, respectively. The band at 870 cm^{-1} can be ascribed to the vibration of surface absorbed N-O, whereas the Ti-N vibration bands can be observed at around 1250 cm^{-1} in the range of 1080-1474 cm^{-1} [41,42]. The peak at 3450 cm^{-1} is attributed to the stretching and bending vibration of the OH group in water molecules in the atmosphere [43].

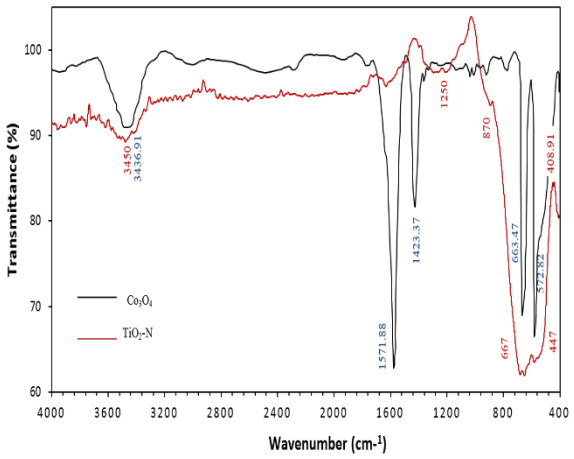

Fig.(5) FTIR spectra of Co_3O_4 sample prepared using gas mixing ratio 60:40 and N-doped TiO_2 sample prepared using gas mixing ratio 40:40:20

The UV-visible absorption spectra within the spectra range of 400-700nm for the Co_3O_4 thin films prepared using different gas mixing ratios are shown in Fig. (6). The absorbance is increasing with increasing oxygen content in the gas mixture and this may be attributed to the formation of more Co_3O_4 nanoparticles. Also, due to increasing oxygen content in the gas mixture, the measurements show very slight blue shift in the absorption edge towards shorter wavelengths [44]. The weak absorption band around 650 nm can be ascribed to the band gap energy transition $p(O^{2-})\rightarrow t_2(Co^{2+})$ [45]. The absorption spectra within the spectral range of 300-700 nm for the N-doped TiO_2 thin films prepared using different doping concentrations of nitrogen are shown in Fig. (7). It is clear that the optical absorption edges are shifted towards longer wavelength (red shift) by increasing the concentration of nitrogen, as they interstitially occupy some positions of oxygen in the TiO_2 lattice [46,47].

The Tauc's equation can be used to determine the energy band gap from the relationship between the photon energy and absorption coefficient as [48]:

$$(\alpha h\nu)^n = A(h\nu - E_g) \qquad (2)$$

where A is a constant, E_g is the energy band gap and n is a constant, taking values of 0.5 or 2 for indirect and direct allowed transitions, respectively

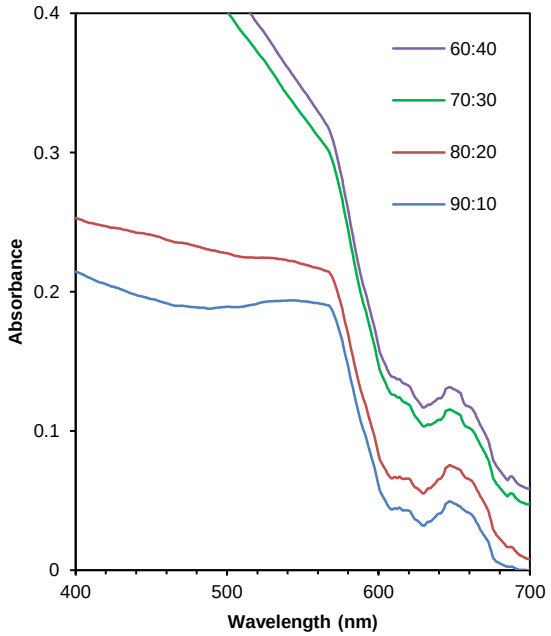

Fig. (6) Absorption spectra of Co_3O_4 thin films prepared by using different gas mixing ratios

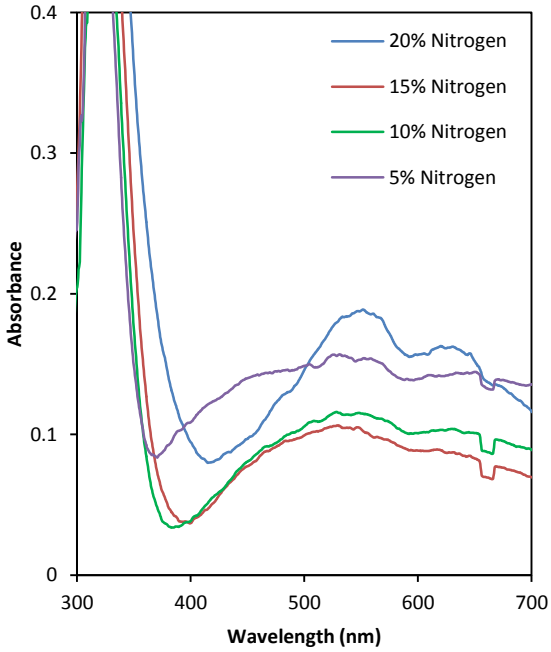

Fig. (7) Absorption spectra of N-doped TiO_2 thin films prepared using different concentrations of nitrogen in the gas mixture

In accordance to the results of absorption, figure (8a) shows that the energy band gap of Co_3O_4 thin film prepared by using 60:40 gas mixing ratio and 1 hour of deposition time is 2.15 eV [49], while figure (8b) shows the energy band gap of N-doped TiO_2 thin films prepared using different concentrations of nitrogen (5, 10, 15 and 20%). The energy band gap was shifted to lower energies and decreased to 2.94 eV due to the contribution of nitrogen dopants in

 ISSN (print) 1813-2065, (online) 2309-1673

TiO_2 nanostructures. The lowest value of E_g was obtained for the sample doped with the highest concentration of nitrogen (20%) as its values were 3.03, 3.12 and 3.17 eV for concentrations of 15, 10 and 5%, respectively.

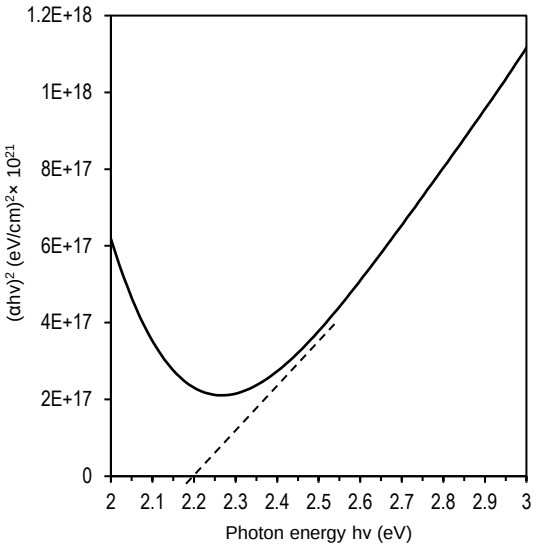

(a)

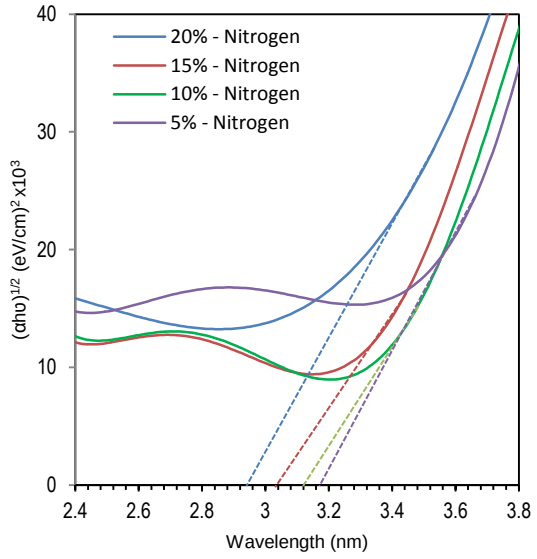

(b)

Fig. (8) Determination of energy band gap for (a) Co_3O_4 sample prepared using gas mixing ratio of 60:40, and (b) N-doped TiO_2 samples using different concentrations of nitrogen in the gas mixture

Figure (9a) shows the optical transmission spectra of single-layer device (ECD) (glass/ITO/Co_3O_4/NaOH/Pt) in the visible region (400-700nm). At colored state, the transmittance decreased to 16.5% as a voltage of +2V was applied. By applying reverse voltage of 2V, the transmittance increased to 50% (bleached state). Colored and bleached states were obtained by redox process within 4 s for each state. The optical transmittance modulation ($\Delta T = T_b - T_c$) is 33.5%.

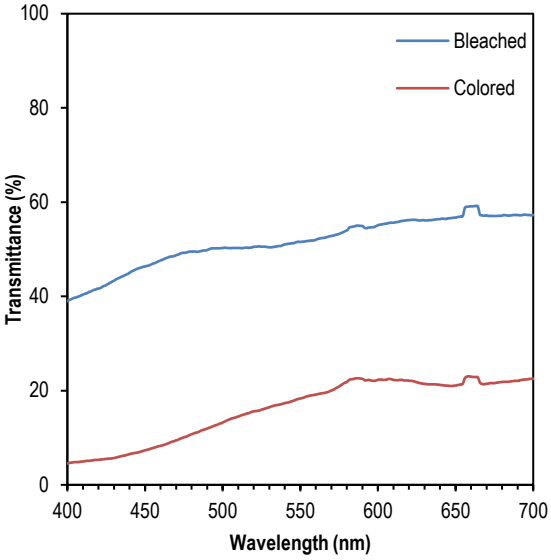

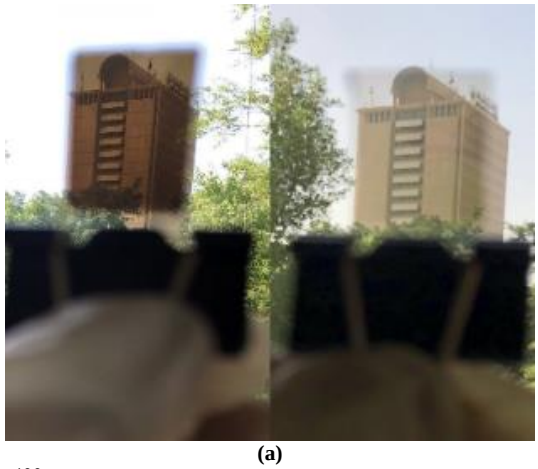

(a)

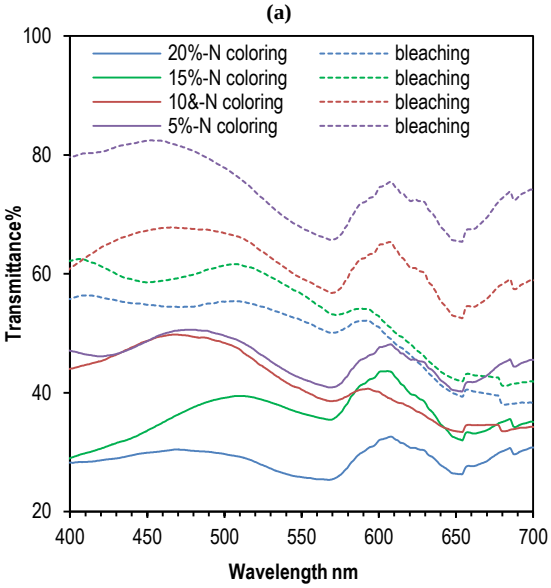

(b)

Fig. (9) Transmission spectra of (a) ECD based on Co_3O_4 as EC layer, and (b) PECD based on N-doped TiO_2 as EC layer with different concentrations of nitrogen and Co_3O_4 as IS layer. The attached photos are for PECD based on N-doped TiO_2 as EC layer with 20% nitrogen and Co_3O_4 as IS layer

For the PECD with multilayer configuration (Glass/ITO/N-doped TiO_2/Co_3O_4/NaOH/Pt), when a voltage of -5V was applied, the transmittance was measured to be 43.2, 41, 36.7 and 26.1% (colored state) for the samples with nitrogen concentration of 5, 10, 15 and 20%, respectively, under xenon light irradiation, as shown in Fig. (9b). By reversing the voltage polarity (bleached state), the transmittance was increased to 54% for the sample with nitrogen concentration of 20%. These states were obtained within 3 minutes, therefore, the optical transmittance modulation ($\Delta T=T_b-T_c$) is 27.9%.

4. Conclusion

In concluding remarks, the layers of PEC and EC devices with different configurations were successfully synthesized by dc reactive magnetron sputtering technique. The concentration of nitrogen in N-doped TiO_2 samples plays an important role in increasing the efficiency of the N-doped TiO_2 as EC layer. The EC device with single layer configuration has a higher coloring efficiency and longer response time than the PEC device with multilayer configuration, as the response time was 4 s for EC device and 3 min for PEC device for both coloring and bleaching states.

References

[1] A. Dokouzis et al., "Photoelectrochromic devices with cobalt redox electrolytes", *Materials Today: Energy*, 15 (2020) 100365.

[2] O.A. Hamadi and K.Z. Yahiya, "Optical and electrical properties of selenium-antimony heterojunction formed on silicon substrate", *Sharjah Univ. J. Pure Appl. Sci.*, 4(2) (2007) 1-11.

[3] J. Mardaljevic, R. K. Waskett and B. Painter, "Electrochromic Glazing in Buildings: A Case Study", in **"Electrochromic Materials and Devices"**, Wiley-VCH Verlag GmbH (2013) 571–592.

[4] C. Costa et al., "Photoelectrochromic devices: Influence of device architecture and electrolyte composition", *Electrochimica Acta*, 219 (2016) 99-106.

[5] K.-D. Li, P.-W. Chen and K.-S. Chang, "Low-Temperature Deposition of Transparent Conducting Films Applied to Flexible Electrochromic Devices", *Materials*, 14(17) (2021) 4959.

[6] Z.S. Abdulsattar and F.J. Kadhim, "Synthesis and Characteristics of Electrochromic Glass with Multi-Layer Configuration Based on glass/ITO/WO_3/ZrO_2/NiO/ITO/glass", *Iraqi J. Appl. Phys.*, 15(4) (2019) 17-22.

[7] P. Bonhote, L. Walder and M. Gratzel, "Electrochromic or photoelectrochromic device", US Patent, No. 6734305, May 2004.

[8] X. Wu, J. Zheng and C. Xu, "Highly Optical Performance Photoelectrochromic Device Based on Br^-/Br_3^- Electrolyte", *Electrochimica Acta*, 191 (2016) 902-907.

[9] M.A. Bhatt and A.R. Tanna, "A Review on Electrochromic Materials for Smart Window Applications: Past, Present and Future", Int. Res. Conf. on Innov. Startup and Invest. (ICOSTART-2019) (Rajkut, India) September 2020.

[10] W. Zhang et al., "Nanostructured inorganic electrochromic materials for light applications", *Nanophot*., 10(2) (2020) 825-850.

[11] B. Li et al., "Recent Advances in Inorganic Electrochromic Materials from Synthesis to Applications: Critical Review on Functional Chemistry and Structure Engineering", *Chemistry - An Asian J.*, 17 (2022) e202200022.

[12] S.-I. Park et al., "A review on fabrication processes for electrochromic devices", *Int. J. Precis. Eng. Manuf. Green Technol.*, 3(4) (2016) 397-421.

[13] F.J. Al-Maliki, O.A. Hammadi and E.A. Al-Oubidy, "Optimization of Rutile/Anatase Ratio in Titanium Dioxide Nanostructures prepared by DC Magnetron Sputtering Technique", *Iraqi J. Sci.*, 60(special issue) (2019) 91-98.

[14] O.A. Hamadi, B.A.M. Bader and A.K. Yousif, "Electrical Characteristics of Silicon p-n Junction Solar Cells Produced by Plasma-Assisted Matrix Etching Technique", *Eng. Technol. J.*, 28 (2008).

[15] E.L. Runnerstrom et al., "Nanostructured electrochromic smart windows: Traditional materials and NIR-selective plasmonic nanocrystals", *Chem. Commun.*, 50(73) (2014) 10555-10572.

[16] O. Carp, C.L. Huisman and A. Reller, "Photoinduced reactivity of titanium dioxide", *Prog. in Solid State Chem.*, 32 (2004) 33-117.

 ISSN (print) 1813-2065, (online) 2309-1673

[17] M.A. Aziz and F.J. Kadhim, "Characteristics of Multilayer glass/ITO/N:TiO_2/NiO/KOH/Pt/glass Photoelectrochromic Device Synthesized by Reactive Magnetron Sputtering", *Iraqi J. Appl. Phys.*, 18(3) (2022) 11-17.
[18] F.J. Kadhim, O.A. Hammadi and N.H. Mutesher, "Photocatalytic activity of TiO_2/SiO_2 nanocomposites synthesized by reactive magnetron sputtering technique", *J. Nanophot.*, 16(2) (2022) 026005 DOI: 10.1117/1.JNP.16.026005
[19] O.A. Hammadi, "Effects of Extraction Parameters on Particle Size of Titanium Dioxide Nanopowders Prepared by Physical Vapor Deposition Technique", *Plasmonics*, 15(6) (2020) 1747-1754.
[20] V. Patil et al., "Synthesis and Characterization of Co_3O_4 Thin Film", *Soft Nanosci. Lett.*, 2(1) (2012) 1-7.
[21] A.E. Kaloyeros et al., "Review–cobalt thin films: trends in processing technologies and emerging applications", *ECS J. Solid State Sci. Technol.*, 8 (2019) 119-152.
[22] L.D. Kadam, S.H. Pawar and P.S. Patil, "Studies on ionic intercalation properties of cobalt oxide thin films prepared by spray pyrolysis technique", *Mater. Chem. Phys.*, 68(1-3) (2001) 280-282.
[23] L. Li et al., "Low Ni-doped Co_3O_4 porous nanoplates for enhanced hydrogen and oxygen evolution reaction", *J. Alloys Comp.*, 823 (2020) 153750.
[24] P.N. Shelke et al., "Synthesis, characterization and optical properties of selective Co_3O_4 films 1-D interlinked nanowires prepared by spray pyrolysis technique", *Fuel*, 112 (2013) 542-549.
[25] R. Drasovean, S. Condurache-Bota and N. Tigau, "Structural and electrical characterization of cobalt oxide semiconductors", *J. Sci. Arts*, 2(13) (2010) 379-384.
[26] F.J. Al-Maliki, O.A. Hammadi, B.T. Chiad and E.A. Al-Oubidy, "Enhanced photocatalytic activity of Ag-doped TiO_2 nanoparticles synthesized by DC Reactive Magnetron Co-Sputtering Technique", *Opt. Quantum Electron.*, 52 (2020) 188.
[27] R. Hippler et al., "Deposition of cobalt oxide films by reactive pulsed magnetron sputtering", *Surf. Coat. Technol.*, 405 (2021) 126590.
[28] J. Alami, "Plasma Characterization and Thin Film Growth and Analysis in Highly Ionized Magnetron Sputtering", Linköping Studies in Sci. Technol., Diss. No. 948 (2005) ISBN 91-85299-40-5.
[29] O.A. Hammadi and N.E. Naji, "Fabrication and Characterization of Polycrystalline Nickel Cobaltite Nanostructures Prepared by Plasma Sputtering as Gas Sensor", *Phot. Sen.*, 8(1) (2018) 43-47.
[30] N.H. Hashim and F.J. Kadhim, "Structural and Optical Characteristics of Co_3O_4 Nanostructures Prepared By DC Reactive Magnetron Sputtering", *Iraqi J. Appl. Phys.*, 18(4) (2022) 31-36.
[31] H.E. Swnason et al., "Standard X-Ray Diffraction Powder Patterns", International Center for Diffraction Data (ICDD) (Washington DC, 1971), NBS monograph 25, Sec. 9, p. 29
[32] K. Thamaphat, P. Limsuwan and B. Ngotawornchai, "Phase Characterization of TiO_2 Powder by XRD and TEM", *Kasetsart J. (Nat. Sci.)*, 42 (2008) 357-361.
[33] C. Li et al., "*in situ* growth of TiO_2 on TiN nanoparticles for nonnoble-metal plasmonic photocatalysis", *RSC Advances*, 6 (2016) 72659-72669.
[34] S.C. Endres, L.C. Ciacch and L. Madler, "A review of contact force models between nanoparticles in agglomerates, aggregates and films", *J. Aerosol Sci.*, 153 (2021) 105719.
[35] R. Lakra et al., "Synthesis and characterization of cobalt oxide (Co_3O_4) nanoparticles", *Mater. Today: Proc.*, 2 September 2020, 269-271.
[36] O.A. Hamadi, "The fundamentals of plasma-assisted CVD technique employed in thin films production", *Iraqi J. Appl. Phys. Lett.*, 1(2) (2008) 3-8.
[37] A. Hodaei, A.S. Dezfuli and H.R. Naderi, "A high-performance supercapacitor based on N-doped TiO_2 nanoparticles", *J. Mater. Sci.: Materials in Electronics*, 29 (2018) 14596-14604.
[38] K. Maaz, **"Cobalt"**, InTech Open (Croatia, 2017), Ch. 4, p. 56.
[39] A.N. Naveen and S. Selladurai, "Investigation on physiochemical properties of Mn substituted spinel cobalt oxide for supercapacitor applications", *Electrochimica Acta*, 125 (2014) 404-414.
[40] Asraa M. Hameed and Mohammed A. Hameed, "Highly-Pure Nanostructured Metal Oxide Multilayer Structure Prepared by DC Reactive Magnetron Sputtering Technique", *Iraqi J. Appl. Phys.*, 18(4) (2022) 9-14.
[41] Y. Huo et al., "Highly active $TiO_{2-x-y}N_xF_y$ visible photocatalyst prepared under supercritical conditions in NH_4F/EtOH fluid", *Appl. Catal. B, Environ.*, 89(3-4) (2009) 543-550.
[42] F.J. Al-Maliki and N.H. Al-Lamey, "Synthesis of Tb-doped titanium dioxide nanostructures by sol– gel method for environmental photocatalysis applications", *J. Sol-Gel Sci. Technol.*, 81 (2017) 276-283.
[43] S. Baset et al., "Size measurement of metal and semiconductor nanoparticles via UV-vis absorption spectra", *Dig. J. Nanomater. Biostruct.*, 6(1) (2011) 1-8.

[44] W.M. Haynes, **"CRC Handbook of Chemistry and Physics"**, 92nd ed., Taylor & Francis Group (NY, 2012), Ch. 10, pp. 93-146.
[45] O.A. Hammadi, F.J. AL-Maliki and E.A. Al-Oubidy, "Photocatalytic Activity of Nitrogen-Doped Titanium Dioxide Nanostructures Synthesized by DC Reactive Magnetron Sputtering Technique", *Nonl. Opt. Quant. Opt.*, 52 (2019) 1-12.
[46] R. Saravanan, **"Novel Ceramic Materials"**, Materials Research Forum LLC (Millersville PA, 2016), Vol. 2, Ch. 4, p. 49.
[47] E.A. Al-Oubidy and F.J. Al-Maliki, "Photocatalytic activity of anatase titanium dioxide nanostructures prepared by reactive magnetron sputtering technique", *Opt. Quantum Electron.*, 51(1-2) (2019) 23.
[48] M. Yarestani et al., "Hydrothermal synthesis of cobalt oxide nanoparticles: Its optical and magnetic properties'', *Iran J. Sci.*, 25(4): 339-343 (2014)
[49] F.J. Al-Maliki and E.A. Al-Oubidy, "Effect of gas mixing ratio on structural characteristics of titanium dioxide nanostructures synthesized by DC reactive magnetron sputtering", *Physica B: Cond. Matter*, 555 (2019) 18-20.

 ISSN (print) 1813-2065, (online) 2309-1673 PRINTED IN IRAQ

IRAQI JOURNAL OF APPLIED PHYSICS
Vol. 19, No. 1, January-March 2023, pp. 13-20

Isolation of Fungi from Petroleum-Contaminated Soil and Evaluation of Their Ability to Degrade Crude Oil

Mohammed Y. Khdiar [1,5]
Atheer A. Mahmood[2]
Liwaa A. Shihab[1]
Giles E. St. J. Hardy[3,4]

[1] *Department of Biology, College of Education, Al-Iraqia University, Baghdad, IRAQ*
[2] *Department of Chemistry, College of Education, Al-Iraqia University, Baghdad, IRAQ*
[3] *Phytophthora Science and Management, Centre for Climate Impacted Terrestrial Ecosystems, Harry Butler Institute, Murdoch University, WA 6150, AUSTRALIA*
[4] *ArborCarbon Pty. Ltd., Centre for Terrestrial Ecosystem Science and Sustainability, Harry Butler Institute, Murdoch University, WA 6150, AUSTRALIA*
[5] *Green Gold for Sustainable Development, Baghdad, IRAQ*

Petroleum waste is a significant problem facing the environment caused by excessive and random use of petroleum or its derivatives. Interestingly, microorganisms have become the main factor in petroleum degradation. In this study, fungi were isolated from petroleum waste soils and evaluated for their ability to degrade moderate crude oil (MCO) and light crude oil (LCO) as the first step of environmental cleanup from petroleum waste. Twenty-one petroleum contamination sites in the north of Baghdad were studied. The serial dilution method was used to isolate fungi from soil. Colony forming units (CFU) of fungal community and the percentage of fungal genera and species frequently isolated per site were calculated. The physiochemical characteristics, electrical conductivity (EC), hydrogen ion (pH) and soil temperature were measured. Based on their growth rates, ten fungal species isolated from the contaminated soils were evaluated for their ability to decompose crude oil samples in the solid media. The American Petroleum Institute gravity (API gravity), asphaltene, saturated, aromatic, and other characteristics of both crude oils were determined by gas chromatography–mass spectrometry (GC-MS).
A larger number of fungi were recorded from the contaminated soils. Aspergillus species was the most common genus recorded. Site S13 recorded the highest number of fungal communities ($115x10^6$ CFU/gm). The pH ranged from 7 to 9.3, EC ranged from 0.1 to 0.8, and temperature between 22.4 to 24.9 °C. All ten fungal species could decompose crude oil. Through growth rate, Paecilomyces variotii had the highest ability to decompose the two types of oil crude (FGR at 7.8) followed by Fusarium pallidoroseum (FGR at 6.5 of MCO and LCO at 7.2). While Aspergillus flavus had the lowest growth on the MCO medium (FGR at 4.8) and Emericella nidulans had the lowest growth on the LCO medium (FGR at 4.5).

Keywords: Biodegradation; *Aspergillus; Paecilomyces variotii;* Physiochemical properties
Received: 26 December 2022; **Revised:** 18 January 2023; **Accepted:** 25 January 2023

1. Introduction

Pollution is a central threat to ecosystems, human health, and other organisms [1]. Hydrocarbon pollutants are one of the most common environmental problems causing water and land pollution [2]. Petroleum is a complex mixture of hydrocarbons and other organic compounds [3]. Indeed, petroleum contamination changes some physicochemical characteristics of the surrounding environment, such as pH, EC, and temperature [4]. Large concentrations are also highly toxic to many organisms, including humans [5].

The interest in the biodegradation or bioremediation of pollutants has grown significantly due to the need to find sustainable means for environmental cleanup [6]. Bioremediation attempts to utilize the endurance features of microorganisms and their significant ability to eliminate many pollutants, including petroleum and other toxic pollutants [7]. Recently, the main mechanism used to clean up environments polluted by petroleum products is microbial degradation [8].

Existing research mentions the critical role of fungi in the bioremediation of crude oil-polluted soils or water [9–11]. Fungi are important organisms with high capability for hydrocarbon degradation, particularly in soils. The main objective of this study was to evaluate the ability of fungi isolated from petroleum-contaminated soil to biodegrade petroleum hydrocarbons. Subsequently, these fungi could be used for environmental cleanup from petroleum waste.

2. Materials and Methods

2.1 Samples Collection

Twenty-one petroleum-contaminated sites in Al-Taji north of Baghdad were sampled (Table 1). At each site, six to seven small samples (approximately 150 g each) were randomly collected from the soil surface (0-30 cm depth) and combined in sterile bags. At each site and 200 meters away from pollution point, uncontaminated soil was also collected and combined together at one sample. These were transported immediately to the laboratory.

Table (1) Site number, GPS details and soil type for each of the 21 sites sampled

Site No.	GPS site		Type of soil
S1	33.584954	44.277516	Loam
S2	33.564359	44.248677	Loam
S3	33.58714	44.320088	Loam
S4	33.517429	44.283009	Loam
S5	33.556921	44.88252	Loam
S6	33.524299	44.199925	Loam
S7	33.489947	44.210225	Loam
S8	33.465892	44.196492	Loam
S9	33.43o944	44.193745	Loam
S10	33.59738	44.320088	Loam
S11	33.420628	44.223957	Loam
S12	33.416616	44.272709	Loam
S13	33.569853	44.232185	Loam
S14	33.538953	44.274757	Loam
S15	33.539677	44.281312	Loam
S16	33.536954	44.280228	Loam
S17	33.535454	44.278533	Loam
S18	33.592735	44.315612	Loam
S19	33.407218	44.182746	Loam
S20	33.412377	44.27201	Loam
S21	33.413658	44.277568	Loam

2.2 Isolation and Identification of Fungi

For fungal isolation, the serial-dilution method was used. 1ml dilutions of 10-6 and 10-3 were plated onto 10 cm diameter Petri-plates containing potato dextrose agar (PDA) prepared according to the manufacturer's (MilliporeSigma) instructions (39g in1leter). The plates were incubated in the dark at 25°C for 7 days and the number of colony-forming units was recorded. Fungal isolates were identified according to microscopic observations and cultural characteristics, and were classified according to taxonomic keys [12-23].

2.3 Primary Screening procedure

The enrichment procedure was used to estimate the biodegradability of isolated fungi using the modified Hanson technique [24]. A 0.5 cm diameter disc of these fungi (7-days-old) was transferred to Bushnell Haas agar medium (Magnesium sulphate 0.2, Calcium chloride anhydrous 0.02, Potassium dihydrogen phosphate 1, Dipotassium hydrogen phosphate 1, Ammonium nitrate 1, Ferric chloride 0.05, Agar 20) in Petri dishes supplemented with 0.1% (v/v) of Tween 80, 1% MCO, or LCO. MCO and LCO were obtained from the Basrah refinery, and their properties were analyzed by GC-MS. All Petri dishes (3 replicates of each species) were incubated for 20 days at 30±2°C. Fungal growth rates (FGR) were calculated by measuring the diameter of growth after 20 days.

2.4 Physicochemical properties of soil

Physical-chemical properties of the contaminated soils were tested in the laboratory [25]. The soil extract was a 1:1 (W/V) soil/water mixture. The pH, temperature, and electrical conductivity (EC) of each soil were measured using a pH and temperature meter (pH meter S400) and EC meter (TDS Meter, BEP-M510). These results were compared with uncontaminated soil collected from the same area.

2.5 Data analysis

The average colony growth of each site was calculated. In addition, the ratio of each genus and species, the number of each isolate of each genus, and species and CFU were calculated according to the equations shown in the Appendix [26]. Multiple regression analysis was used to calculate the interaction between soil physicochemical properties and the presence of fungi, variation in fungal communities and colony forming units.

3. Results

Eight fungal genera and ten species were isolated from the 21 contaminated sites. These were *Aspergillus flavus, A. terreus, A. niger, Paecilomyces variotii, Bipolaris hawaiiensis, E. nidulans, Fusarium pallidoroseum, Cladosporium herbarum, Ulocladium atrum,* and *Penicillium chrysogenum*. In contrast, *Trichoderma harzianum* and *A. niger* were isolated from the uncontaminated soil samples. *Aspergillus* was the most frequently isolated genus at 57%, followed by *Penicillium chrysogenum* at 23.81% (Fig. 1), whereas four genera, *Paecilomyces, Bipolaris, Fusarium* and *Ulocladium* were less (< 5%) frequently recorded (Fig. 1). *A. flavus* and *P. chrysogenum* were the most frequently (23.81%) isolated species (Fig. 1).

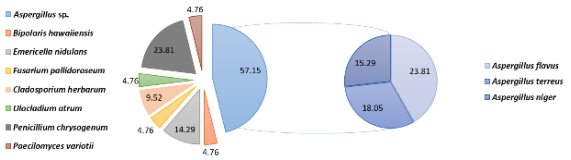

Fig. (1) The percentage of fungal genera and species most frequently isolated from soils contaminated with petroleum waste

A. flavus also had the highest percentage presence at sites S_4 (Fig. 2). However, *A. flavus* was the least capable of degrading the MCO (3±0.5mm), and with the second-lowest ability to degrade the LCO (4.8±0.5mm) in the preliminary screening test (Fig. 3). Out of the *Aspergillus* species, *A. terreus* was the second most frequently isolated at 18.05% and degraded the MCO (6±0.3mm) and the LCO (6.5±0.3mm) (Fig. 3) slightly more efficiently than the other two species. *A. niger* had the highest percentage presence at sites S_{15} and S_{17} (Fig. 2) and grew on the MCO and the LCO media at 6±0.3mm and 6.5±0.4mm, respectively (Fig. 3).

P. variotii was capable of degrading both types of crude oil with growth diameters at 7.8±0.1 (Fig. 3) followed by *F. pallidoroseum*, which degraded the MCO and LCO at rates of 6.5±0.4 mm and 7.2±0.1 mm, respectively.

 ISSN (print) 1813-2065, (online) 2309-1673

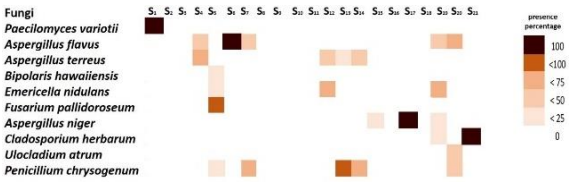

Fig. (2) Heatmap showing the percentage of fungi species present in each soil black oil waste site. White squares represent the absence of fungi, and dark red squares represent the highest rate of presence

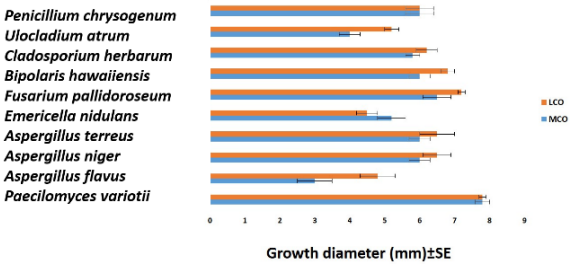

Fig. (3) Mean growth diameter (mm ± SE) for ten fungi species grown on moderate crude oil (MCO) and light crude oil (LCO) media over 20 days at 25°C in the dark

The CFU values varied significantly between sites (Table 2). The highest number of CFU was recorded at site S_{13} at $106x10^6$ CFU/g soil, followed by site S_5 at $10x10^6$ CFU/g soil (Table 3). At the same time, no fungi were recorded at eight of the 21 sites.

Table (2) Fungi species, their number and colony forming units that were isolated from each contaminated oil site

Site No.	No. fungi	Fungi	CFU x10^6
S1	1	*Paecilomyces variotii*	1
S2			0
S3			0
S4	2	*Aspergillus flavus* *Aspergillus terreus*	0.03
S5	4	*Bipolaris hawaiiensis* *Emericella nidulans* *Fusarium pallidoroseum* *Penicillium chrysogenum*	10
S6	1	*A. flavus*	1
S7	2	*A. flavus* *P. chrysogenum*	1
S8			0
S9			0
S10			0
S11			0
S12	2	*E. nidulans, A. terreus*	2
S13	2	*A. terreus, P. chrysogenum*	106
S13		*A. terreus, P. chrysogenum*	
S14	2	*A. terreus, P. chrysogenum*	7
S15	1	*A. niger*	1
S16			0
S17	1	*Aspergillus niger*	1
S18			0
S19	4	*A. niger, A. flavus* *E. nidulans, C. herbarum*	4
S20	3	*A. flavus, U. atrum* *P. chrysogenum*	1
S21	1	*C. herbarum*	1
		Total average =	**6.5**

Regarding soil physicochemical properties, the pH of all soil sites ranged from 7.0 to 9.2 (Table 3). In contrast, the pH of uncontaminated soil was 6.5 (Table 3). EC of the sites ranged from 0.12 to 0.8., compared to 0.16 in the uncontaminated soil (Table 3). The soil temperatures were calculated immediately after they were collected and ranged from 22.4–24.9°C. This compared to 23.1°C for the uncontaminated soil (Table 3). The correlation data showed that the relationship between pH and the presence of fungi was poor ($p < 0.1$) with a high impact ($R2 = 0.41$) (Table 4 Supplementary 1).

Table (3) Physiochemical properties of the soil at each site

Site No.	EC	pH	°C
Control	0.16	6.5	23.1
S1	0.16	7.2	23.0
S2	0.80	8.9	23.0
S3	0.32	9.2	22.5
S4	0.18	8.4	23.3
S5	0.60	8.8	24.9
S6	0.34	8.9	23.3
S7	0.46	9.0	23.6
S8	0.12	9.1	22.7
S9	0.80	9.1	22.9
S10	0.24	9.1	22.4
S11	0.20	8.4	23.6
S12	0.40	8.9	24.0
S13	0.54	8.0	23.6
S14	0.16	9.1	23.6
S15	0.32	8.9	22.4
S16	0.60	9.0	22.6
S17	0.14	9.1	23.5
S18	0.20	9.2	23.0
S19	0.18	9.0	24.0
S20	0.18	9.0	23.0
S21	0.32	7.8	23

In contrast, there was no effect of either temperature or EC on the presence of fungi (Table 4 and Supplementary 1). Concerning variations in fungal communities and the effect of soil physicochemical properties on them, the results showed a small relationship ($p < 0.1$) with a high impact ($R^2 = 0.66$) between EC and variation in the fungal communities (Table 5 and Fig. 5c). In comparison, there was no effect of pH and temperature on the variation of the fungal communities (Table 5 and Supplementary 2). Finally, the relationship between soil physicochemical properties and CFU showed that pH significantly affected the fungal community ($R^2 = 0.57$, $p = 0.0003$) (Table 6 and Supplementary 2). At the same time, EC and temperature had no effect.

Table (4) Multiple regression analysis showing correlation between the three physicochemical variables and the fungal species based on their presence or absence. Significant values shown in bold text

Factor	*df*	*SS*	*MS*	*F-value*	R2	P-value
pH	3	3.14	1.05	4.01	0.41	**0.07**
Residuals	17	4.43	0.26			
Total	20	7.57				
EC	3	2.84	0.95	3.40	0.38	0.19
Residuals	17	4.73	0.28			
Total	20	7.57				
Temperature °C	3	1.93	0.64	1.92	0.25	0.16
Residuals	17	5.69	0.33			
Total	20	7.62				

Table (5) Multiple regression analysis showing correlation between the three physicochemical variables and the variation in fungal communities. Significant values shown in bold text

Factor	*df*	*SS*	*MS*	*F-value*	R2	P-value
pH	3	4.22	1.41	7.16	0.56	0.81
Residuals	17	3.34	0.20			
Total	20	7.57				
EC	3	4.99	1.66	10.96	0.66	**0.07**
Residuals	17	2.58	0.15			
Total	20	7.57				
Temperature °C	3	0.59	0.20	0.47	0.08	0.26
Residuals	17	7.03	0.41			
Total	20	7.62				

The GC-MS results showed differences between LCO and MCO concerning the aromatic and saturated compounds (Table 7).

Table (6) Multiple regression analysis showing correlation between the three physicochemical variables and colony forming units (CFU). Significant values shown in bold text

Factor	*df*	*SS*	*MS*	*F-value*	R2	P-value
pH	3	4.29	1.43	7.43	0.57	**0.0003**
Residuals	17	3.27	0.19			
Total	20	7.57				
EC	3	0.63	0.21	0.51	0.08	0.44
Residuals	17	6.94	0.41			
Total	20	7.57				
Temperature °C	3	0.64	0.21	0.52	0.08	0.60
Residuals	17	6.98	0.41			
Total	20	7.62				

Table (7) Geochemical summary of the two crude oils that were analyzed by GC-MS, including the American Petroleum Institute gravity (API Gravity), n-Paraffin/Naphthene (n-P/N) and percentages of sulfur, asphaltene, carbon isotopes 15, and aromatic and saturated hydrocarbons

Crude oil types	API Gravity	n-P/N	%S	% Asphaltene	%C15	% Aromatic	% Saturated
LCO	36.7	0.89	0.94	0.6	53.9	30.6	62.3
MCO	27.5	0.48	2.26	7.2	35.9	36.9	43.2

4. Discussion

Bioremediation is an important branch of biotechnology that uses different organisms, including microorganisms and plants, to clean up environments and degrade contaminants to levels with minimal toxicity [27]. Compared to traditional bioremediation techniques, fungi are the most efficient petroleum degraders [28].

The preliminary step for using fungi in bioremediation and biodegradation of petroleum is isolating and identifying fungi associated with petroleum-polluted areas, and conducting primary screening to evaluate their ability for biodegradation. This study isolated 10 species belonging to eight fungal genera from 21 sites with petroleum-contaminated soil north of Baghdad. They have previously been isolated from petroleum-contaminated soils [29-31]. *Aspergillus* was the most frequently isolated genus among the eight fungal genera in this study. Filamentous fungi play a significant role in biodegrading petroleum and its derivatives [32]. *Aspergillus* and *Penicillium* are the filamentous fungi most frequently isolated from petroleum-contaminated soils worldwide [33]. *Aspergillus* species have been documented as possible candidates for biodegradation of a broad range of petroleum hydrocarbons in the environment [34, 35]. The main reason for the ability of *Aspergillus* to biodegrade petroleum could be that this genus can degrade both aromatic and saturated hydrocarbons [33].

In the present study, *Aspergillus* was represented by three species, *A. flavus*, *A. terreus* and *A. niger*. *A. flavus* was the dominant species at site S_6 and was the most frequently isolated species. This species was previously isolated from different petroleum polluted sites [29, 36]. However, in the present study, *A. flavus* was the least capable of degrading the MCO and the second less capable of degrading the LCO. This finding is somewhat counterintuitive and contrary to previous studies, which have demonstrated that *A. flavus* has the highest ability to degrade crude oil at several concentrations of crude oil derivatives [29]. Considerably more work will need to be done to determine the ability of *A. flavus* for degrading different petroleum kinds.

A. terreus was isolated from a petroleum-contaminated site in a previous study [37], and has a high capacity to degrade heavy oil [38], and other aromatic hydrocarbons [39]. In the current study, *A. terreus* was the third most frequently isolated species and degraded both the MCO and the LCO.

A. niger recorded the highest percentage presence at sites S_{15} and S_{17} and was capable of degrading the MCO and the LCO. These results reflect those of Gesinde et al., [40] , who also found that *A. niger* had the highest capability of degrading four kinds of crude oil, Arabian light, Durb oil, Bonny light, and Escravos light.

Interestingly, *P. variotii* had the highest capacity to degrade the two kinds of crude oil. This species also dominated site S_1 in this study. A possible explanation for this might be that *P. variotii* has a high capacity to degrade different hydrocarbons, whether aromatic or saturated. Despite the significant differences between LCO and MCO concerning the aromatic and saturated compounds, shown by GC-MS, *P. variotii* was capable of degrading them both. Consequently, *P. variotii* could be a potential candidate for eliminating oil spills.

Another species with a strong ability to degrade the oils was *F. pallidoroseum*, with the second-highest capability of degrading the MCO and LCO. This result is not surprising as *Fusarium* spp., *Aspergillus* spp. and *Penicillium* spp. have been listed as species with significant abilities to biodegrade hydrocarbons [41, 42].

All the fungal species except *E. nidulans* could degrade the LCO more efficiently than the MCO. The most likely reasons for this result are that LCO contains many hydrocarbons, which are easy to

 ISSN (print) 1813-2065, (online) 2309-1673

decompose by fungi. Secondly, the density of LCO is less than MCO; thus, LCO has less viscosity. Thirdly, MCO has a large amount of asphaltene that could make it more resist biodegradation [43]. However, the high ability of some of these fungi, such as *P. variotii* and *F. pallidoroseum*, as biodegraders of LCO and MCO is an important issue for future research.

5.1 Fungal community

Petroleum waste degradation through the microbial community of soil depends on many factors, including abundance, the kind and catabolic performance of microorganisms, and environmental conditions and chemical structure of the compounds to be biodegraded [44]. On the other hand, crude oil pollutants are a crucial issue for the abundance of microorganisms in the soil. In this study, the results of CFU showed significant variation between the sites, with the mean total of colony forming units being $6.5x10^6$ CFU/g soil. This finding is consistent with that of Cheraghi [4] who mentioned that the lower populations of fungi and bacteria in petroleum-contaminated soil could be due to changes in soil texture and chemical content resulting from the petroleum wastes. However, the number of fungi in the soil is still in the accepted range 10^3 to 10^8 CFU/g soil [45]. Site S_{13} had the highest number of CFU followed by site S_5. Whereas at eight of the sites, no fungi were recorded. This outcome may be due to the toxicity resulting from the petroleum contaminants [46, 47], or because the properties of the soil, such as pH, moisture and organic content, are altered [5, 48].

5.2 Physicochemical properties of soil

Soil physicochemical properties significantly affect microbial degradation of hydrocarbons [49]. One of the most important factors of soil is pH value because it affects numerous chemical processes in soils [50]. The pH is considered a determining factor in soil pollutants destination, their decomposition, and leakage in the soil [4] Comparison of the findings with those of other studies confirms the pH of the soil was impacted by the wastes in oil crude and its derivatives [4, 51–53]. The second factor is electrical conductivity (EC) which represents the concentration of ions in soil [4]. The fluctuations in the EC results in current research indicate that oil crude may influence soil ionic stability. The third factor studied in this study was soil temperature (°C), and the results revealed no effect of oil crude on soil temperature.

The most striking results to emerge from the data are the correlation between soil physicochemical properties and the presence of fungi, variation in the fungal communities, and CFU. The results of relationship between pH and presence fungi revealed a small relationship ($p < 0.1$) with a high impact ($R2 = 0.41$). This outcome confirms that soil pH values can slightly affect the presence and absence of fungi. The correlation between soil physicochemical properties and variation of the communities showed a small relationship ($p < 0.1$) with a high impact ($R2 = 0.66$) between EC and variation of the fungal communities. This outcome confirms that the EC value of soil contributes to some variation in the composition of the fungal communities in soil. This finding was not surprising, as EC was reported as one of the factors affecting the microbial community in different types of soil [54, 55]. The outcome of pH is contrary to that of Lloret et al., [55] who found that pH had the highest impact on the fungal communities. This could be because fungi can grow in a wide range of pH [56].

What is interesting in these results is that the relationship between pH and the CFU was statistically very highly significant. This result reflects another study that found that microbial biomass was impacted by soil pH [57].

Indeed, physicochemical properties could have an impact on fungi in soil whatever the presence of fungi or variation in the fungal communities or CFU.

6. Conclusion

The purpose of the current study was to isolate fungi from soils contaminated with crude oil and evaluate their capability to degrade two kinds of Iraqi crude oil (moderate and light). *A. flavus, A. terreus, A. niger, P. variotii, B. hawaiiensis, E. nidulans, F. pallidoroseum, C. herbarum, U. atrum* and *P. chrysogenum* belonging to eight fungal genera were isolated from different soil sites north of Baghdad that were contaminated with crude oil. This study has shown that all these species can degrade both kinds of crude oil. The research has also shown that *P. variotii* has the highest ability to degrade the two kinds of crude oil. This species requires further study. Related to soil physicochemical properties, pH can influence the presence of fungi, and has a significant effect on CFU. Whereas EC can influence the composition of fungal communities in soil. These findings need more research in future to determine the best conditions for fungi to effectively eliminate crude oil waste.

References

[1] I. Manisalidis et al., "Environmental and health impacts of air pollution: a review", *Front. public Heal.*, 14 (2020).

[2] A.A. Adekunle and O.A. Adebambo, "Petroleum Hydrocarbon Utilization by Fungi Isolated From Detarium Senegalense (J. F Gmelin) Seeds", *J. Am. Sci.*, 3(1) (2007) 69-76.

[3] J.D. van Hamme, A. Singh and O.P. Ward, "Recent Advances in Petroleum Microbiology", *Microbiol. Mol. Biol. Rev.*, 67(4) (2003) 503-549.

[4] M. Cheraghi, "Biochemical and Physical Characterization of Petroleum Hydrocarbon Contaminated Soils in Tehran", 5 (2015) 199-208.

[5] M. Khan et al., "Microbial diversity changes with rhizosphere and hydrocarbons in contrasting soils", *Ecotoxicol. Environ. Saf.*, 56 (2018) 434-442.
[6] S. Mondal and D. Palit, **"Sustainable Agriculture, Forest and Environmental Management"**, Springer (2019).
[7] M.A. Malla et al., "Understanding and designing the strategies for the microbe-mediated remediation of environmental contaminants using omics approaches" *Front. Microbiol.*, 9(6) (2018) article 1132.
[8] S.J. Varjani, "Microbial degradation of petroleum hydrocarbons", *Bioresour. Technol.*, 233 (2016) 277-286.
[9] V. Catania et al., "Innovative, ecofriendly biosorbent-biodegrading biofilms for bioremediation of oil-contaminated water", *N. Biotechnol.*, 58 (2020) 25-31.
[10] R. Thenmozhi et al., "Studies on Mycoremediation of used engine oil contaminated soil samples", *Pelagia Res. Libr. Adv. Appl. Sci. Res.*, 4(2) (2013) 110-118.
[11] A.M. Mukred et al., "Development of Three Bacteria Consortium for the Bioremediation of Crude Petroleum-oil in Contaminated Water", *Online J. Biol. Sci.*, 8(4) (2008) 73-79.
[12] K. Bensch et al., "The genus cladosporium", *Stud. Mycol.*, 72 (2012) 1-401.
[13] D. Liu and J. Gray, "4 Bipolaris and Drechslera", in **"Mol. Detect. Hum. Fungal Pathog"**, CRC Press (FL, 2011) 49-53.
[14] K.H. Domsch, W. Gams and T.H. Anderson, **"Compendium of Soil Fungi"**, Academic Press,(London, 1980).
[15] C. Booth, **"The Genus Fusarium",** Commonwearth Mycological Institute, Key, Surrey (England, 1971).
[16] H. Afzal, S. Shazad and S.Q.U. Nisa, "Morphological identification of aspergillus species from the soil of larkana district (Sindh, Pakistan)", *Asian J. Agric. Biol.*, 1(3) (2013) 105-117.
[17] N. McClenny, "Laboratory detection and identification of Aspergillus species by microscopic observation and culture: The traditional approach", *Med. Mycol.*, 43(1) (2005) 125-128.
[18] D.N.R. Sari and S.D. Anitasari, "Isolation of Indigenous Fungi in River Containing Ammonia from Rubber Industry Waste in Jember", *J. Multidiscip. Appl. Nat. Sci.*, vol. 2 (1) (2002) 58-64.
[19] T.T.T. Nguyen, N.C. Paul and H.B. Lee, "Characterization of Paecilomyces variotii and Talaromyces amestolkiae in Korea based on the morphological characteristics and multigene phylogenetic analyses", *Mycobiol.*, 44(4) (2016) 248-259.
[20] F. Fierro et al., "Penicillium chrysogenum, a Vintage Model with a Cutting-Edge Profile in Biotechnology", *Microorgan.*, 10(3) (2022) 573.
[21] T. Bose, S. Ghosh and S.N. Ghosh, "First report of Fusarium pallidoroseum (Cooke) Sacc. causing wilt disease of Chlorophytum nepalense (Lindley) Baker", *J. Mycopathol. Res*, 48(1) (2010) 111-114.
[22] K.B. Raper and D.I. Fennell, "The genus Aspergilius.," *The genus Aspergilius.*, (1965) 238–268.
[23] E. G. Simmons, "Typification of Alternaria, Stemphylium, and Ulocladium," *Mycologia*, 59(1) (1967) 67–92.
[24] G. Zafra et al., "Isolation and selection of a highly tolerant microbial consortium with potential for PAH biodegradation from heavy crude oil-contaminated soils", *Water. Air. Soil Pollut.*, 225(2) (2014) 1-18.
[25] R. Burt, "Kellogg soil survey laboratory methods manual. Soil Survey Investigations Report no. 42, Version 5.0," *Lincoln USDA*, (2014) 1–219.
[26] T.C. Tseng, J.C. Tu and S.S. Tzean, "Mycoflora and mycotoxins in dry bean (Phaseolus vulgaris) produced in Taiwan and in Ontario, Canada", *Bot. Bull. Acad. Sin.*, 36(4) (1995) 229–234.
[27] M. Vidali, "Bioremediation. An overview", *Pure Appl. Chem.*, 73(7) (2001) 1163-1172.
[28] M. Vanishree, A.J. Thatheyus and D. Ramya, "Biodegradation of Petrol Using the Fungus Penicillium sp.", *Sci. Int.*, 2(1) (2014) 26-31.
[29] A. Hashem, "Bioremediation of Petroleum Contaminated Soils in the Arabian Gulf Region: A Review", *J. King Abdulaziz Univ.*, 19(1) (2007) 81-91.
[30] H.F. Deli, "Assessment of the Ability of Fungi Isolates Bipolaris hawaiiensis and Emericella nidulans Isolated from Soils Containing Petroleum Waste in the Analysis of Crude Oil ", *Al-Mustansiriyah J. Sci.*, 25(3) (2014) 7-12.
[31] A. Benguenab and A. Chibani, "Biodegradation of petroleum hydrocarbons by filamentous fungi (Aspergillus ustus and Purpureocillium lilacinum) isolated from used engine oil contaminated soil", *Acta Ecol. Sin.*, 41(5) (2021) 416-423.
[32] G. Saratale et al., "Biodegradation of kerosene by Aspergillus ochraceus NCIM-1146", *J. Basic Microbiol.*, 47(5) (2007) 400-405.
[33] E.O. dos Santos et al., "Pre-screening of filamentous fungi isolated from a contaminated site in Southern Brazil for bioaugmentation purposes", *African J. Biotechnol.*, 7(9) (2008) 1314-1317.
[34] J.-S. Ye et al., "Biodegradation of anthracene by Aspergillus fumigatus", *J. Hazard. Mater.*, 185(1) (2011) 174-181.
[35] J. Zhang et al., "Degradation of crude oil by fungal enzyme preparations from Aspergillus

 ISSN (print) 1813-2065, (online) 2309-1673 PRINTED IN IRAQ

spp. for potential use in enhanced oil recovery", *J. Chem. Technol. Biotechnol.*, 91(4) (2016) 865-875.
[36] F. Kota et al., "Bioremediation of Crude Oil by Different Fungal Genera", *Asian J. Plant Biol.*, 2(1) (2014) 16-23.
[37] V. Balaji, P. Arulazhagan and P. Ebenezer, "Enzymatic bioremediation of polyaromatic hydrocarbons by fungal consortia enriched from petroleum contaminated soil and oil seeds", *J. Environ. Biol.*, 35(3) (2014) 521-529.
[38] J. Zhang et al., "Microbial enhanced heavy oil recovery through biodegradation using fungal extracellular enzymes from Aspergillus spp.", *preprint from Res. Sq.*, (2020) 1-27.
[39] M.I.A. Ali, N.M. Khalil and M.N. Abd El-Ghany, "Biodegradation of some polycyclic aromatic hydrocarbons by Aspergillus terreus", *African J. Microbiol. Res.*, 6(16) (2012) 3783-3790.
[40] A.F. Gesinde et al., "Bioremediation of some Nigerian and Arabian crude oils by fungal isolates", *Int. J. Pure Appl. Sci.*, 2(3) (2008) 37-44.
[41] O. Obire and E.C. Anyanwu, "Impact of various concentrations of crude oil on fungal populations of soil", *Int. J. Environ. Sci. Technol.*, 6(2) (2009) 211-218.
[42] A.A. Adekunle and T.F. Oluyode, "Biodegradation of crude petroleum and petroleum products by fungi isolated from two oil seeds (melon and soybean)", *J. Env. Biol.*, 26(1) (2005) 37-42.
[43] T. Tavassoli et al., "Asphaltene biodegradation using microorganisms isolated from oil samples", *Fuel*, 93 (2012) 142-148.
[44] A.K. Haritash and C.P. Kaushik, "Biodegradation aspects of Polycyclic Aromatic Hydrocarbons (PAHs): A review", *J. Hazard. Mater.*, 169(1-3) (2009) 1-15.
[45] I.N. Ogunmwonyi et al., "Microbial analysis of different top soil samples of selected site in Obafemi Awolowo University, Nigeria", *Sci. Res. Essays*, 3(3) (2008) 120-124.
[46] R. Margesin, A. Zimmerbauer and F. Schinner, "Monitoring of bioremediation by soil biological activities," *Chemosphere*, 40(4) (2000) 339-346.
[47] P. Olga et al., "Screening method for detection of hydrocarbon-oxidizing bacteria in oil-contaminated water and soil specimens", *J. Microbiol. Methods*, 74(2-3) (2008) 110-113.
[48] Q. Tian et al., "Land-use types and soil chemical properties influence soil microbial communities in the semiarid Loess Plateau region in China", *Sci. Rep.*, 7(1) (2017) 1-9.
[49] B.W. Bogan and W.R. Sullivan, "Physicochemical soil parameters affecting sequestration and mycobacterial biodegradation of polycyclic aromatic hydrocarbons in soil", *Chemosphere*, 52(10) (2003) 1717-1726.
[50] M.E. Ojewumi et al., "A bioremediation study of raw and treated crude petroleum oil polluted soil with Aspergillus niger and Pseudomonas aeruginosa", *J. Ecol. Eng.*, 19(2) (2018) 226-235.
[51] L.C. Osuji et al., "An appraisal of the impact of petroleum hydrocarbons on soil fertility: the Owaza experience", *African J. Agric. Res.*, 2(7) (2007) 318-324.
[52] J.G. Bundy, G.I. Paton and C.D. Campbell, "Microbial communities in different soil types do not converge after diesel contamination", *J. Appl. Microbiol.*, 92(2) (2002) 276-288.
[53] O. Obire and O. Nwaubeta, "Effects of refined petroleum hydrocarbon on soil physicochemical and bacteriological characteristics", *J. Appl. Sci. Environ. Manag.*, 6(1) (2002) 39-44.
[54] J.M. Kim et al., "Soil pH and electrical conductivity are key edaphic factors shaping bacterial communities of greenhouse soils in Korea", *J. Microbiol.*, 54(12) (2016) 838-845.
[55] E. Lloret et al., "Sewage sludge addition modifies soil microbial communities and plant performance depending on the sludge stabilization process", *Appl. Soil Ecol.*, 101 (2016) 37-46.
[56] J. Rousk et al., "Soil bacterial and fungal communities across a pH gradient in an arable soil", *ISME J.*, 4(10) (2010) 1340-1351.
[57] J.C.A. Pietri and P.C. Brookes, "Substrate inputs and pH as factors controlling microbial biomass, activity and community structure in an arable soil", *Soil Biol. Biochem.*, 41(7) (2009) 1396-1405.

Appendix

$$\% \text{ genus presence} = \frac{\text{no. of a genus in the site}}{\text{no. of all other genera on the site}} \times 100$$

$$\% \text{ species presence} = \frac{\text{no. of a species in the site}}{\text{no. of all other species on the site}} \times 100$$

$$\% \text{ frequency of a genus} = \frac{\text{no. of a genus in the site}}{\text{no. of sites}} \times 100$$

$$\% \text{ frequency of a species} = \frac{\text{no. of a species in site}}{\text{no. of sites}} \times 100$$

CFU= (no. of colonies x dilution factor) / volume of culture plate

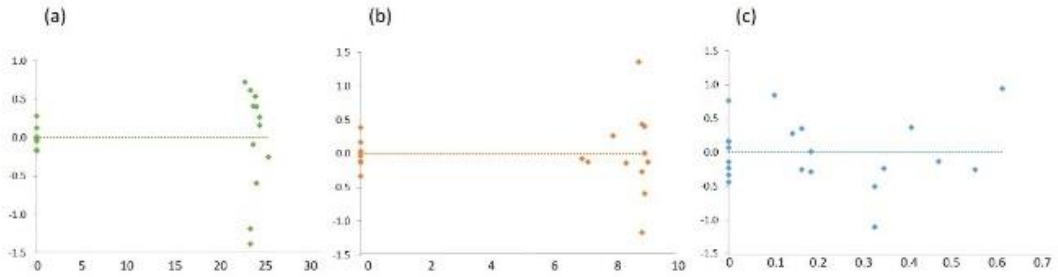

Supplementary (1) Multiple regression analysis showing correlation between three physicochemical variables and fungal species based their presence or absence: (a) correlation between temperature and the presence of fungi, (b) correlation between pH and the presence of fungi, and (c) correlation between EC and the presence of fungi

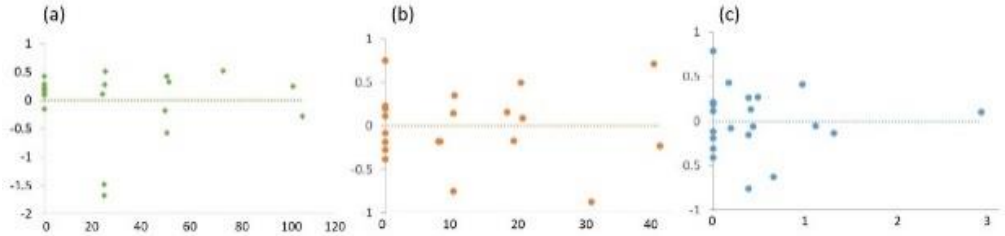

Supplementary (2) Multiple regression analysis showing correlation between three physicochemical variables (a) temperatures (b) pH and (c) EC and variation of fungal community

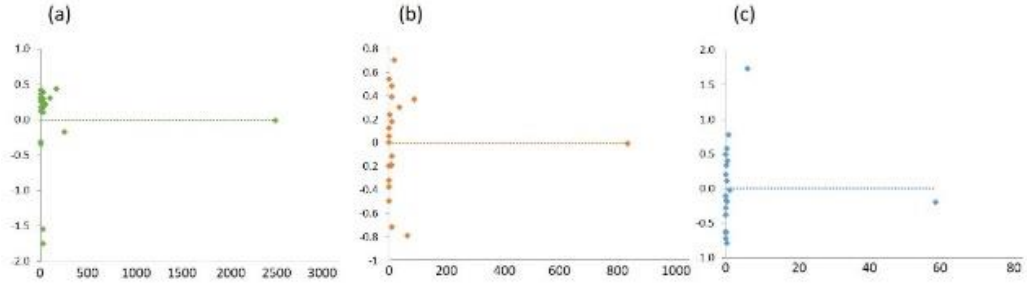

Supplementary (3) Multiple regression analysis showing correlation between three physicochemical variables (a) temperature, (b) pH, and (c) EC and rate of fungal community (CFU)

 ISSN (print) 1813-2065, (online) 2309-1673

IRAQI JOURNAL OF APPLIED PHYSICS
Vol. 19, No. 1, January-March 2023, pp. 21-28

Comparative Study of Gamma and Beta Rays Exposure Effects on Manganese Sulphide Thin Films for Solar Cell Applications

Rawaa E. Mohammed[1]
Issam M. Ibrahim[2]
Akram M. Ali[3]

[1] *Department of Physics, College of Education for Pure Sciences, University of Anbar, Ramadi, IRAQ*
[2] *Department of Physics, College of Science, University of Baghdad, Baghdad, IRAQ*
[3] *Department of Physics, College of Science, University of Anbar, Ramadi, IRAQ*

Ionization-radiation such as charged particles and gamma radiation highly affects the properties of semiconductors' thin films by different mechanisms including the ionization process, and crystal-defect formation. In this work, the effect of beta and gamma radiations on the properties of deposited MnS thin films by spray pyrolysis, and the effect of defect formation on the current-voltage characteristic of the MnS/Si heterojunction for solar cells application were studied. The prepared thin films were examined by XRD, FE-SEM, and UV absorbance before and after exposure to a pure beta source (Sr-90) and gamma source (Co-60). The results show highly effect of the gamma exposure compared with the beta radiation on the structural properties by reducing crystallinity. The surface morphology and optical properties are highly affected by the two radiations. The photovoltaic properties of Mn/Si heterojunction enhanced with limited exposure time of beta radiation despite the structural changes which may be due to the increase of the charge carriers generated, while low enhancement by gamma radiation.

Keywords: MnS; Beta radiation; Gamma radiation; Structural properties; Solar cells
Received: 22 November 2022; **Revised:** 22 November 2022; **Accepted:** 22 November 2022;

1. Introduction

Many researchers are interested in renewable energy applications such as solar cells to meet the huge global demand for energy [1], as an alternative to combustion energy that leads to an increase in harmful environmental pollution to living organisms including human beings [2]. There are many effects that may harm the efficiency of solar cells, such as exposure to high temperatures [3] or exposure to ionizing radiation in large doses. Solar cells can be applied in locations with a high radiation background such as in scientific [4], and space applications [5].

Photons and high-energy particles are two main forms of ionizing radiation [6]. Exposure of thin films to ionizing radiation may lead to changes in their microstructure, formation of crystalline defects, or the occurrence of ionization of some atoms that affect their physical properties such as structural, optical, and electrical properties [7]. Among the forms of structural defects in crystalline semiconductors are atomic displacements that lead to the creation of interstitial atoms and gaps, lattice stress, and other crystalline defects [7]. The type of radiation and energy have a significant impact on the amount of spatial damage it causes [8]. The material parameters and, consequently, the performances of the heterojunctions are altered by these changes [9]. The nature of this change depends on the type and energy of the radiation. In the literature, low-dose irradiation's effects on the structural, morphological, and optical characteristics of thin films were investigated. A low dose of radiation may enhance crystallization [10].

Aklo (2019) studied the effect of irradiation with fast neutrons on the structural properties of MnS thin films for use in optical detectors. He observed an increase in the bandgap energy with increasing doses [11]. Obodo et al, (2020) investigated the effect of copper ions radiation with different doses on Co_3O_4 NiO-ZnO nanostructures. They showed that low doses of radiation improve the nanostructure, while high doses cause structural defects and disorder in the crystal structure, and increase in the level of the defects with increasing doses [12].

In this work, a comparison between two types of radiations namely gamma and beta on the surface morphology, structural properties, and optical properties of the prepared MnS thin films by spray pyrolysis were investigated, and their outcome on the current-voltage characteristics of heterojunction solar cells.

2. Experimental Part

Manganese sulfide (MnS) thin films were deposited on glass slides as shown in Fig. (1) by spray pyrolysis technique using 0.1 M concentration of mixed manganese chloride ($MnCl_2$:$2H_2O$) of purity ≥99% and Thiourea of purity ≥99% (Sigma-Aldrich Co.) at Mn:S of (1:1) atomic ratio in (1:1) alcohol to distilled water solution. The powders manganese

chloride and Thiourea were dissolved were dissolved in distilled water by a magnetic stirrer and then added to alcohol. The atomizer is fixed at 30 cm above the controlled temperature substrates at 400°C. The spray rate was fixed at about 1.5 ml/min using compressed air at 5 bar pressure by a controlled valve. The thin film thickness was determined using a reflectance probe (SR300 Angstrom Sun Technologies) which was about 250±20 nm.

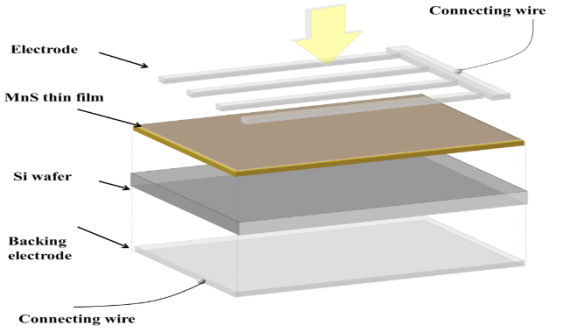

Fig. (1) Schematic diagram of MnS/Si solar cell device

Strontium-90 source (Sr-90) of pure beta radiation of 545.9 keV was used to irradiate the thin films sample at a distance of 5 cm for 3 days inside a shielded zone. Gamma exposure was done using Co-60 for 2 days.

The as-prepared MnS thin films and the irradiated samples were tested by the XRD (Shimadzu XRD 6000), FE-SEM and EDS (Inspect F50), and UV visible spectroscopy. Heterojunctions of MnS/ n-type Si wafer were prepared based on the as-deposited and the exposed- samples. Aluminum comb-like electrodes at the front of the MnS surface and back electrode were deposited by thermal evaporation under high vacuum by Edward coating unit using appropriate masks. The I-V characteristics were determined in dark and under a halogen lamp of 100 mW/cm^2 irradiance using a Keithley electrometer.

3. Results and discussions

Figure (2) illustrates the XRD patterns for the as-deposited MnS thin film on glass slides, beta-exposed, and gamma-exposed samples. The pure phase of polycrystalline cubic MnS structure appeared for the three patterns according to the JCPDS card No. 96-900-5946. The crystallinity was reduced, while line broadening increased for the exposed sample indicating a reduction in the crystallite size. The preferred orientation was along (200) direction at 36.67°. Crystallization drops after beta exposure and is more affected by gamma radiation. The diffraction lines were widened after the two types of radiation due to decrease in the crystallite size, according to Scherrer's principle [13]. In addition to a few shifts of diffraction angles for the irradiated sample due to the creation of some lattice strain as a result of defects formation [14].

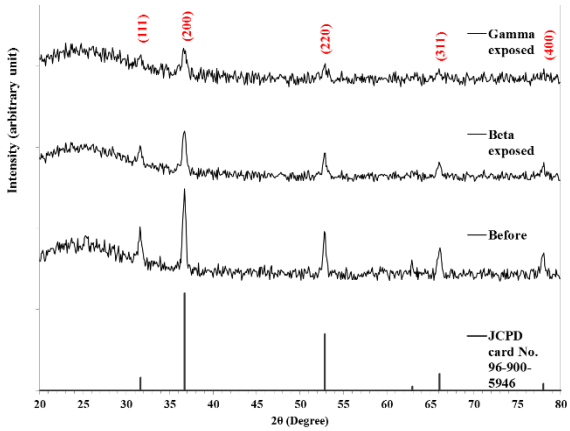

Fig. (2) XRD patterns for as-prepared MnS thin films and after exposure to beta and gamma radiations compared with the standard diffraction lines

The interplanar spacing (d_{hkl}) was determined according to Bragg's law [15]:

$$n\lambda = 2d_{hkl}\, sin\theta \qquad (1)$$

where θ is the diffraction angles, λ is the used wavelength of x-ray tube for Cu-K$_\alpha$ transition, and n is the diffraction order.

The crystallite size (D) was determined using Scherrer's formula [15]:

$$D = \frac{0.94\,\lambda}{\text{FWHM Cos}\theta} \qquad (2)$$

where FWHM is the full-width at half maximum, and the lattice strain is given by the following equation [16]

$$\varepsilon = \frac{\text{FWHM Cos}\theta}{4} \qquad (3)$$

Table (1) illustrates the XRD parameters including *2θ, d_{hkl}, FWHM, D*, and Miller indices for the diffraction lines for MnS thin films before and after exposure to beta and gamma rays. The average crystallite size for the as-prepared thin films was 22.1 nm and reduced to 20.5 nm after exposure to beta radiation and to 18.1 nm after exposure to gamma radiation. The lattice strain increased after the exposure due to the increase of lattice defects [17].

Table (1) XRD characteristics of as-deposited MnS thin films and after exposed to beta and gamma radiations compared with the standard d_{hkl} values

Sample	2θ (Deg)	FWHM (Deg)	d_{hkl} Exp. (Å)	D (nm)
Before	31.6200	0.3840	2.8273	21.5
	36.6700	0.4110	2.4487	20.4
	52.9110	0.3960	1.7291	22.4
	66.0690	0.4210	1.4130	22.5
	78.0228	0.4310	1.2237	23.7
Beta exposed	31.6251	0.4224	2.8269	19.5
	36.6756	0.4521	2.4484	18.5
	52.9216	0.4356	1.7287	20.4
	66.0721	0.4631	1.4130	20.5
	78.0228	0.4310	1.2237	23.7
Gamma exposed	31.6302	0.4608	2.8264	17.9
	36.6812	0.4932	2.4480	17.0
	52.9322	0.4752	1.7284	18.7
	66.0751	0.5052	1.4129	18.8

 ISSN (print) 1813-2065, (online) 2309-1673

(continued)

Sample	2θ (Deg)	d_{hkl} Std. (Å)	hkl	ε×10³
Before	31.6200	2.8261	(111)	1.61
	36.6700	2.4475	(200)	1.70
	52.9110	1.7306	(220)	1.55
	66.0690	1.4131	(311)	1.54
	78.0228	1.2237	(400)	1.46
Beta exposed	31.6251	2.8261	(111)	1.77
	36.6756	2.4475	(200)	1.87
	52.9216	1.7306	(220)	1.70
	66.0721	1.4131	(311)	1.69
	78.0228	1.2237	(400)	1.46
Gamma exposed	31.6302	2.8261	(111)	1.93
	36.6812	2.4475	(200)	2.04
	52.9322	1.7306	(220)	1.86
	66.0751	1.4131	(311)	1.85

The FE-SEM images of the deposited MnS thin film and samples exposed to beta for 3 days and gamma radiation for 2 days were shown in Fig. (3). The as-prepared film has shown a rough surface with small scattered nanoparticles at different dimensions staked on its surface. The sample surface converted to an extremely porous structure after the beta exposure. The surface nanostructures were reduced in number after the gamma exposure and the film became less cohesive and appeared intermit.

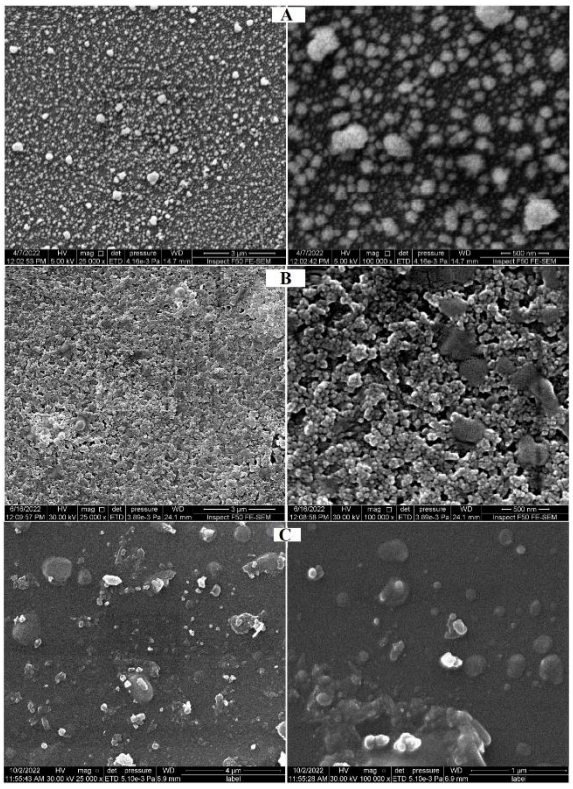

Fig. (3) FE-SEM image for as-prepared MnS thin films at two magnifications (A), exposed sample to beta radiation for 3 d (B), and exposed sample to gamma radiation for 2 d (C)

The quantitative element analysis is implemented by energy-dispersive x-ray spectroscopy (EDS) which based on the principle that each element has unique emitted lines of electromagnetic emission after excitation by x-ray. Figure (4) shows the EDS spectra for the as-deposited MnS samples on glass substrates, the sample exposed to beta radiation for 3 days, and the sample exposed to gamma radiation for 2 days. The spectra show emitted lines for manganese metals (Mn), sulphur (S), and oxygen (O) come from oxidized states and chlorine element as a residual element from the started precursors. Additional emitted lines corresponding to glass substrate such as silicon (at about 1.7 keV) and other trace elements have appeared as well. The peak intensities vary according to their existence in the samples. The EDS map shows decreasing distribution density for Mn and S after the irradiation process.

We note that after using the gamma rays the thin film was greatly affected, which made the intensity of Mn and S lines reduced after exposure to both beta and gamma rays (The highest affected by γ), and the Si peak was dominant. Table (2) lists the atomic and weight percentage for the elements. The EDS map for the Mn and S elements were shown next to the figure. It seems that the uniformly distributed of both elements over the sample surface.

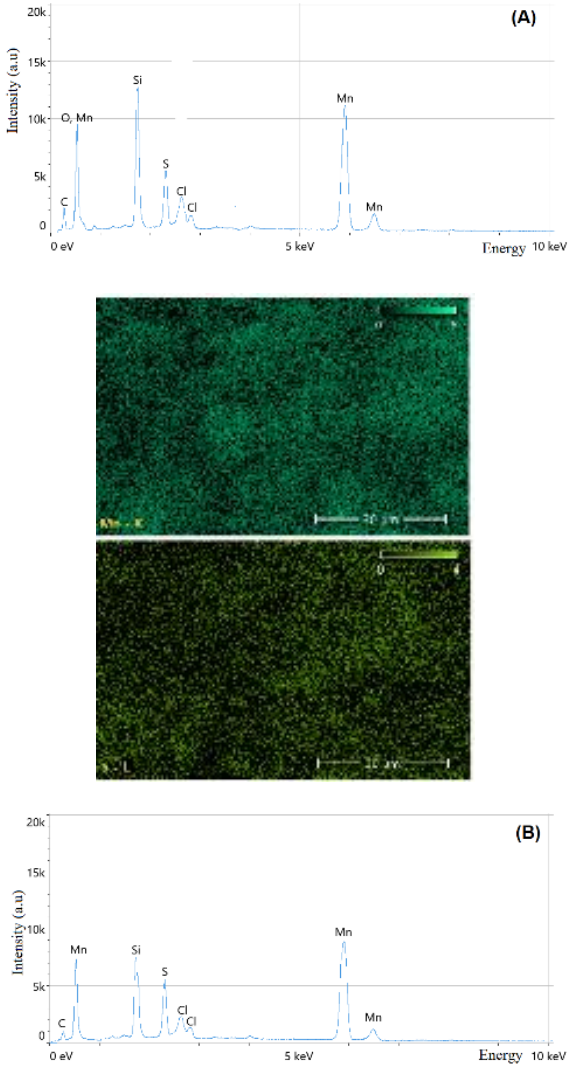

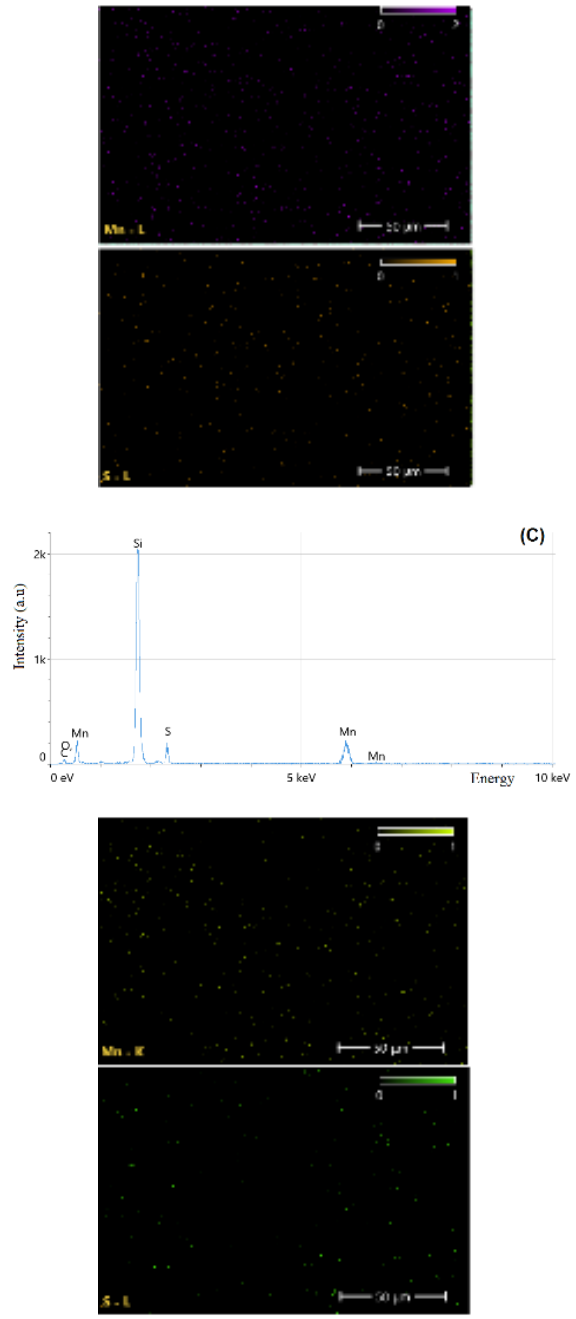

Fig. (4) EDS analysis for the as-deposited MnS sample on glass substrates (A), exposed sample to beta radiation for 3 d (B), and exposed sample to gamma radiation for 2 d (C)

Table (2) Quantitative EDS analysis for the as-deposited MnS thin films on glass substrates, exposed to beta radiation for 3 d, and exposed to gamma radiation for 2 d

Element	As- deposited		Beta exposed		Gamma exposed	
	At. %	Wt. %	At. %	Wt. %	At. %	Wt. %
C	5.10	1.88	6.25	2.24	5.31	2.50
O	8.60	3.71	3.40	1.42	17.10	8.38
Si	25.50	22.09	14.00	12.10	30.20	27.30
S	**29.80**	**15.43**	**33.65**	**17.30**	**20.32**	**11.53**
Cl	3.20	3.31	8.24	8.53	4.47	5.73
Mn	**27.80**	**53.58**	**34.46**	**58.41**	**22.60**	**44.56**

Figure (5) shows the UV-visible absorption spectra for the as-prepared and the irradiated MnS thin films with beta and gamma. The absorption was slightly increased after irradiation due to crystal defects that act as scattering centers [18], while gamma rays reduce absorption may be due to the decomposition of thin films creating gaps that allow light to pass through and get trapped inside the film.

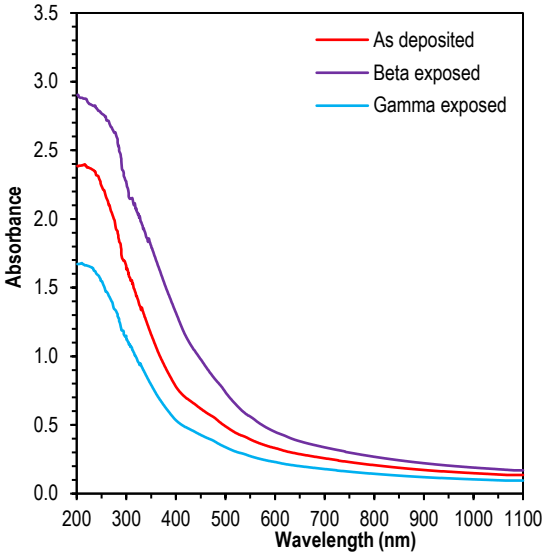

Fig. (5) Absorption spectra the as-prepared MnS thin films and the irradiated sample with beta and gamma

The optical bandgap energy (E_g^{opt}) were measured using Tauc's formula, as shown in Fig. (6). The value of (E_g^{opt}) decreased from 3.14 to 2.90 eV after exposure to beta radiation due to the creation of defect levels near the valence and conduction bands leading to narrow the bandgap energy. On the other hand, the value of (E_g^{opt}) increased to 3.30 eV after exposure to gamma radiation due to a high reduction in crystallite size as a result of the quantum confinement effect [19].

The *Urbach* energy (E_u) is created near the absorption edges by structural defects. It is proportional to the density of crystallinity defects. In this region, the absorption coefficient is given by [7]

$$\alpha = \alpha_o \exp(\frac{h\nu}{E_u}) \qquad (4)$$

Here, E_u is equal to the inverse of the slope of the linear part of the logarithm of the absorption coefficient ($Ln\alpha$) against photon energy ($h\nu$), as presented in Fig. (7). E_u increased from 1.22 to 1.26 and 1.28 eV after exposure to beta and gamma radiation, respectively, indicating the formation of defect states near the valance and conduction bands with a higher effect of gamma rays than beta particles.

 ISSN (print) 1813-2065, (online) 2309-1673

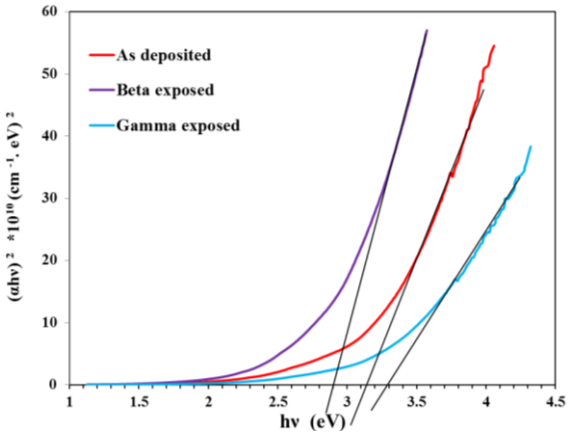

Fig. (6) Relationship of $(\alpha h\nu)^2$ versus hν plot for the MnS thin film before and after beta exposure

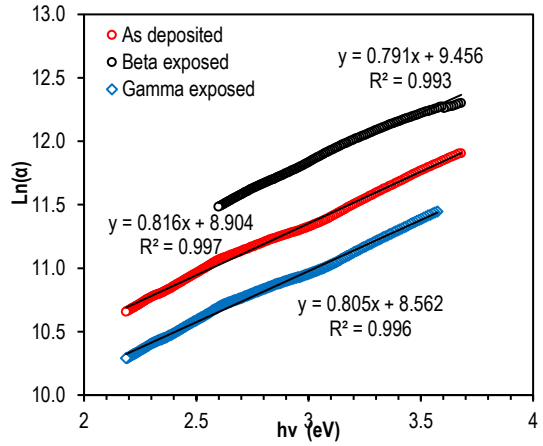

Fig. (7) relationship of Ln(α) against $h\upsilon$ for as-prepared MnS thin films and after 3d exposure to beta and gamma

Hall effect measurements for as-deposited MnS thin film on glass slides and the irradiated samples by beta and gamma radiations were shown in Table (3). By using of Hall effect the charge carrier (n_H) and mobility (μ_H) were determined. All samples appeared as p-type. In all samples, the charge carrier concentration increases after beta irradiation as a result of creating more new charge carriers by ionization. While, the mobility (μ_H) has the opposite behavior as decreased for all samples. Such behavior is expected as a result of increasing the sample porosity due to displacement and damage effect by radiation. Reducing the crystalline size cause to create more grain boundaries against conducting the charge current [20]. A few factors, including particle size, content, defects, and surface roughness, affect the conductivity of thin films. The electrical characteristics of the films would alter if these properties changed [21]. Though reducing the carrier mobility the conductivity of the sample increased as a result of increasing the carrier concentration. Gamma irradiation has the same manner as beta irradiation but with a higher effect on all samples due to its higher penetration ability.

Table (3) Hall effect parameters for the as-deposited Sn_2S_3, CuS_2, and MnS thin films and irradiated samples with beta and gamma

Sample	R_H ($cm^{-3}.C^{-1}$)	n×10^{15} (cm^{-3})	μ_H ($cm^2/V.s$)	σ_{RT} ($\Omega^{-1}.cm^{-1}$)
As deposited	2100	2.98	37.80	0.018
Beta irradiated	910	6.87	30.94	0.034
Gamma irradiated	770	8.12	16.17	0.021

The I–V characteristics of the prepared MnS/n-Si heterojunction before and after exposure to beta and gamma radiation, in dark and under the illumination of simulated solar power of 100 mW/cm^2 were illustrated in Fig. (8). The non-ideality factor of the junctions was calculated from the slope of the linear part of Ln(I) against V, for the forward part of the dark curve as shown next to the I-V curves.

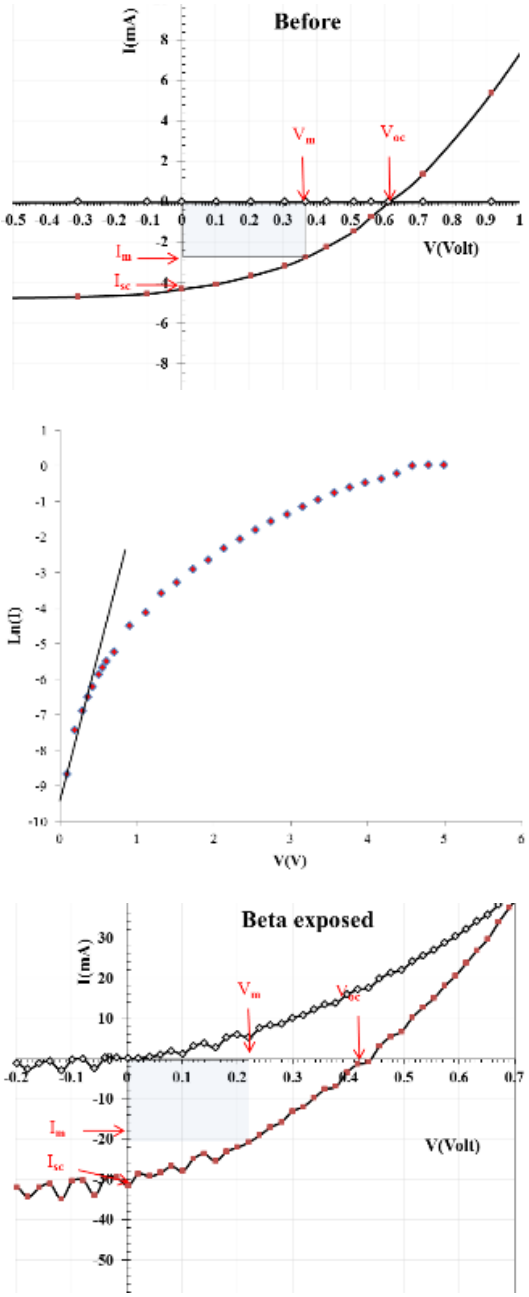

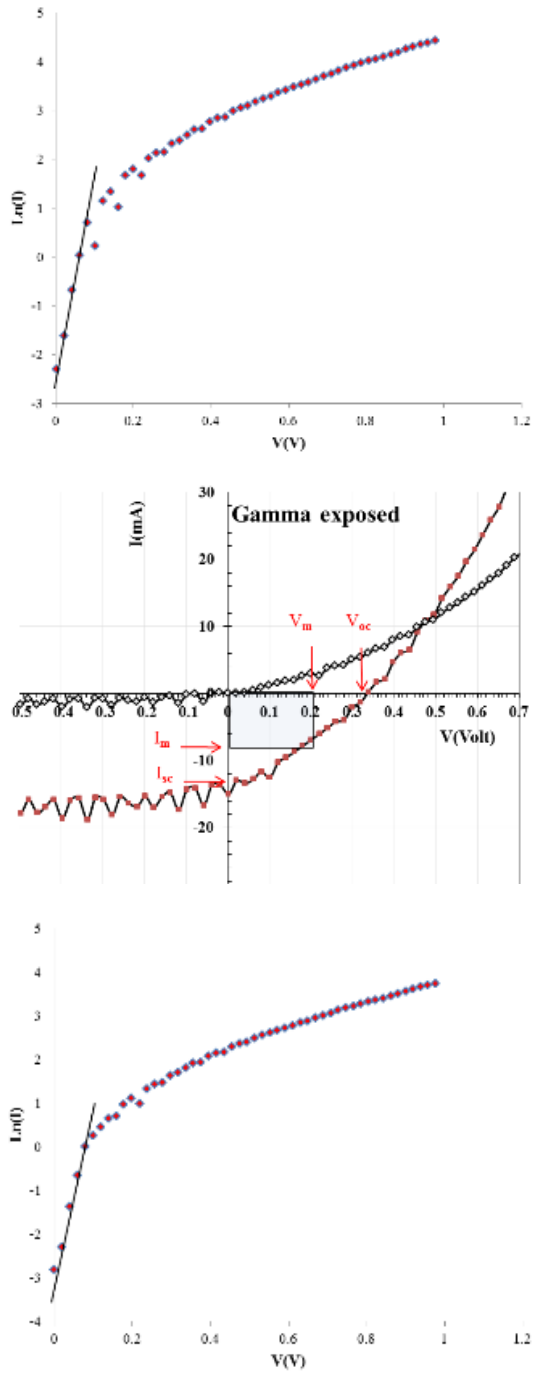

Fig. (8) I-V curves (in dark and under illumination) and the non-ideality factor calculation for MnS/Si heterojunction and after exposure to beta and gamma radiations

The maximum power point was determined by plotting the power against voltage (P-V) as shown in Fig. (9). The maximum points for the as-prepared, beta-exposed, and gamma-exposed heterojunctions were 1.00, 4.56, and 1.41 mW at 0.37, 0.22, and 0.18 V, respectively.

The fill factor is calculated according to the relation:

$$FF = \frac{I_m V_m}{I_{sc} V_{oc}} \qquad (5)$$

where I_m, V_m, I_{SC} and V_{OC} represent the current and voltage at maximum harvesting power, short current circuit, and open-circuit voltage, respectively. The maximum harvesting efficiency is calculated using the following relation:

$$\eta_{max} = \frac{P_m}{P_{in}} \times 100\% \qquad (6)$$

where P_m is the maximum power and P_{in} is the input solar power

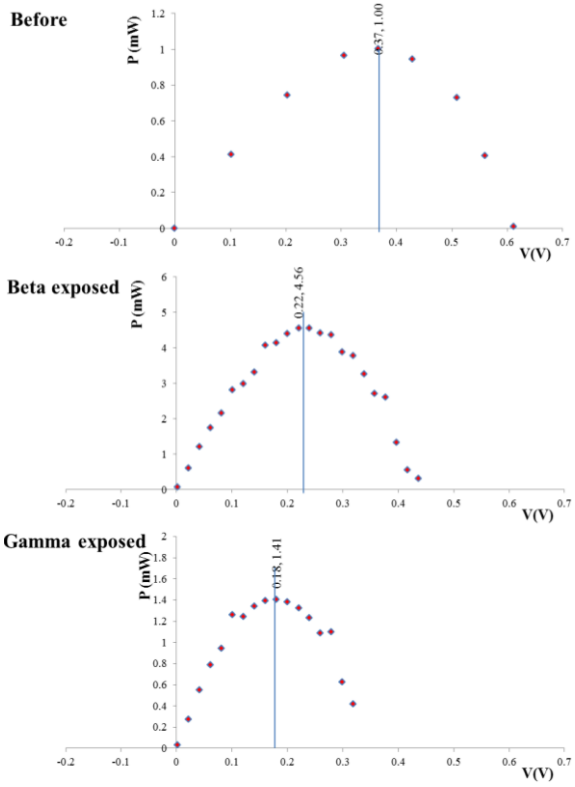

Fig. (9) P-V characteristics under illumination for the fabricated MnS/Si heterojunction and after exposure to the two radiations

The photovoltaic parameters are illustrated in Table (4). The samples exhibit photovoltaic effects with different efficiencies depending on the active layer properties. The efficiency increased from 1.01 to 4.55% after the beta irradiation process. These values are comparable with previously achieved efficiency for photovoltaic based on manganese sulfide thin films [22]. A noticeable decrease in the open-circuit voltage after beta irradiation, is caused by the creation of localized states in the bandgap due to the structural defects formation. On the other hand, we notice a significant increase in the short circuit current from 4.40 to 30.00 mA and to 14.00 mA after beta and gamma irradiation, respectively, which due to the emergence of additional charge carriers in the sample after irradiation, as shown by the Hall effect test, which contributes in transfer the electric current. Despite all the changes in the structural and optical properties, the efficiency enhanced, which may be due to the increase of the charge carriers generated due to the ionization process when exposed to radiation [23]. After gamma exposure, the efficiency

 ISSN (print) 1813-2065, (online) 2309-1673

becomes 1.41% for the MnS/n-Si heterojunctions. Further decrease in the open-circuit voltage was observed after gamma irradiation that may be attributed to its high effect to form structural defects and hence localized states within the bandgap. Some increment in the short circuit current is due to the emergence of additive charge carriers by the ionization process of some lattice atoms by gamma radiation, which contribute to electric current. The values of the non-ideality factor were acceptable in all samples. A clear correlation can be observed between the V_{oc} and E_u, where the increase in the E_u of the cause to reduce the V_{oc}. This implied that the value of E_u is an indicator of the quality of the heterojunction solar cell [24,25].

Table (4) Photovoltaic parameters for the MnS/Si heterojunction and after exposure to the two radiations

Sample	I_{sc} (mA)	V_{oc} (V)	I_m (mA)	V_m (V)	F.F	H (%)	β
Before	4.40	0.63	2.72	0.37	0.36	1.01	6.04
Beta	30.00	0.43	20.70	0.22	0.35	4.55	1.03
Gamma	14.00	0.34	7.82	0.18	0.30	1.41	1.08

4. Conclusions

The exposure of MnS thin films prepared by spray pyrolysis to beta and gamma radiations causes noticeable crystallite defects including displacement of atoms from their sites. Limited exposure of thin film semiconductors to ionization radiations cause controlled defect which can enhance or retard their physical properties. The result shows great effect of gamma ray compared with beta radiation exposure on structural properties and surface morphology of the prepared MnS thin films, by reducing the crystallization and minimizing the crystallite size. The light absorbance increased with beta radiation due to scattering from the created defect centres while it decreased with gamma radiation. The optical bandgap reduced with beta radiation and increased with gamma radiation as a result of the quantum confinement effect. *Urbach* edge increased after exposure to both types of radiation. The photovoltaic performance of MnS/Si heterojunction enhanced with limited exposure time to beta radiation despite the structural changes which may be due to the increase of the charge carriers as a result of vacancies formation.

References

[1] V. Blay et al., "Research Frontiers in Energy Related Materials and Applications for 2020–2030", *Adv. Sustain. Syst.*, 4(2) (2020) 1900145.
[2] A.A. Qureshi et al., "Facile formation of SnO_2–TiO_2 based photoanode and Fe_3O_4@rGO based counter electrode for efficient dye-sensitized solar cells", *Mater. Sci. Semicond. Process.*, 123 (2021) 105545.
[3] F. Kersten et al., "Degradation of multicrystalline silicon solar cells and modules after illumination at elevated temperature", *Sol. Ener. Mater. Sol. Cells*, 142 (2015) 83-86.
[4] S.K. Sen et al., "Effect of gamma (γ-) irradiation on the structural, morphological, optical and electrical properties of spray pyrolysis-deposited h-MoO_3 thin films", *Surf. Interfaces*, 17 (2019) 100377.
[5] I. Cardinaletti et al., "Organic and perovskite solar cells for space applications", *Sol. Ener. Mater. Sol. Cells*, 182 (2018) 121-127.
[6] Ö.F. Özpolat et al., "Phy-X/ZeXTRa: a software for robust calculation of effective atomic numbers for photon, electron, proton, alpha particle, and carbon ion interactions", *Rad. Environ. Biophys.*, 59(2) (2020) 321-329.
[7] M. Ezzeldien et al., "Electron beam irradiation-induced changes in the microstructure and optoelectronic properties of nanostructured Co-doped SnO_2 diluted magnetic semiconductor thin film", *The Euro. Phys. J. Plus*, 137(8) (2022) 905.
[8] I.G. Madiba et al., "Effect of neutron irradiation on the structural, electrical and optical properties evolution of RPLD VO_2 films", *Nucl. Instrum. Meth. Phys. Res. Sec. B: Beam Interact. Mater. Atoms*, 443 (2019) 25-30.
[9] M. Souli et al., "Improved structural properties, morphological and optical behaviors of sprayed Cu_2ZnSnS_4 thin films induced by high gamma radiations for solar cells", *Mater. Sci. Semicond. Process.*, 83 (2018) 50-57.
[10] B. Oryema et al., "Effects of low-dose γ-irradiation on the structural, morphological, and optical properties of fluorine-doped tin oxide thin films", *Rad. Phys. Chem.*, 176 (2020) 109077.
[11] K.N. Aklo, "Irradiation of the thin films of MnS with fast neutrons and the possibility of using the new characteristics in optical detector", *Energy Procedia*, 157 (2019) 290-295.
[12] R.M. Obodo et al., "8.0 MeV copper ion (Cu^{++}) irradiation-induced effects on structural, electrical, optical and electrochemical properties of Co_3O_4-NiO-ZnO/GO nanowires", *Mater. Sci. Ener. Technol.*, 3 (2020) 193-200.
[13] M. Ravikumar et al., "Fabrication of Eu doped CdO [Al/Eu-nCdO/p-Si/Al] photodiodes by perfume atomizer based spray technique for opto-electronic applications", *J. Mol. Struct.*, 1160 (2018) 311-318.
[14] H.S. Sen et al., "Interface-Driven Strain in Heavy Ion-Irradiated Zr/Nb Nanoscale Metallic Multilayers: Validation of Distortion Modeling via Local Strain Mapping", *ACS Appl. Mater. Interfaces*, 14(10) (2022) 12777-12796.

[15] L.K. Dintle et al., "Compositional dependence of optical and electrical properties of indium doped zinc oxide (IZO) thin films deposited by chemical spray pyrolysis", *Physica E: Low-dimen. Syst. Nanostr.*, 99 (2018) 91-97.
[16] K. Ghosh and R.K. Pandey, "Fractal and multifractal analysis of In-doped ZnO thin films deposited on glass, ITO, and silicon substrates", *Appl. Phys. A*, 125(2) (2019) 98.
[17] V.S. Vavilov, **"Effects of Radiation on Semiconductors"**, Springer (US, 1965).
[18] K.W. Böer and U.W. Pohl, **"Optical Properties of Defects",** in Semiconductor Physics, Springer Int. Pub. (2018) 629-676.
[19] A. Goudarzi et al., "Study of optical properties of ZnS and MnZnS (ZnS/MnS) nanostructure thin films; Prepared by microwave-assisted chemical bath deposition method", *Mater. Chem. Phys.*, 275 (2022) 125103.
[20] I. Vladimirov et al., "Energy barriers at grain boundaries dominate charge carrier transport in an electron-conductive organic semiconductor", *Sci. Rep.*, 8(1) (2018) 14868.
[21] S.S. Hegde et al., "Vacuum annealed tin sulfide (SnS) thin films for solar cell applications", *Surf. Interfaces*, 10 (2018) 78-84.
[22] S.A. Fadaam et al., "Improving efficiency of solar cell for MnS through annealing", *AIP Conf. Ser.*, 2307 (2020) 020030.
[23] H. Wei and J. Huang, "Halide lead perovskites for ionizing radiation detection", *Nat. Commun.*, 10(1) (2019) 1066.
[24] B. Subedi et al., "Urbach Energy and Open-Circuit Voltage Deficit for Mixed Anion–Cation Perovskite Solar Cells", *ACS Appl. Mater. Interfaces*, 14(6) (2022) 7796-7804.
[25] J. Chantana et al., "Examination of Relationship between Urbach Energy and Open-Circuit Voltage Deficit of Flexible Cu(In,Ga)Se_2 Solar Cell for Its Improved Photovoltaic Performance", *ACS Appl. Ener. Mater.*, 2(11) (2019) 7843-7849.

 ISSN (print) 1813-2065, (online) 2309-1673

IRAQI JOURNAL OF APPLIED PHYSICS
Vol. 19, No. 1, January-March 2023, pp. 29-34

Hiba S. Rasheed

Investigation of Some Structural and Optical Properties of PMMA-PVA/PDA Nanocomposites

Department of Physics,
College of Education,
Al-Mustansiriyah University,
Baghdad, IRAQ

The poly(methylmethacrylate) (PMMA) and poly(vinylalcohol) (PVA) hybrid films were doped by different weight percentages of polydopamine (PDA) nanoparticles (0.5, 2, 3.5 and 5 wt.%) prepared by solution cast method. The structural and optical characteristics of nanocomposites have been investigated. The optical properties of PMMA-PVA/PDA nanocomposites revealed that the coefficient of extinction, coefficient of absorption, absorbance, index of refraction, imaginary and real dielectric constants of PMMA-PVA blend increased as the polydopamine concentrations of nanoparticles increased, while the energy band gap and the transmittance decreased. The indirect allowed energy gap decreased from 3.58 eV to 3.18 eV and the energy indirect forbidden gap reduced from 2.9 eV to 2.4 eV. The findings of applications for PMMA-PVA/PDA nanocomposites reveal that the x-ray attenuation coefficients increase with the concentration of nanoparticles, which is connected to the absorption or reflection of x-ray by PMMA-PVA/PDA nanocomposites.

Keywords: Nanocomposites; Polydopamine; Nanoparticles; Structural properties
Received: 20 October 2022; **Revised:** 14 November 2022; **Accepted:** 21 November 2022

1. Introduction

Nanotechnology is one of the most popular areas for current study and development in virtually all technological disciplines [1,2]. The including polymer science and technology, and investigations in this subject include a wide variety of problems [3]. Polymer nanocomposites have to bring more significant attention due to its higher effectiveness. This is imputed to the influence of the nanofillers on the mechanical, structure and other properties. Nevertheless, the nanofillers are lighter weight and less required reinforcements in comparison with other matrix components. Therefore, many investigations were focused on the design and model various factors to improve the mechanical properties of different nanocomposite materials [4,5]. For instance, G. Han et al. [6] investigated the effects of acid hydrolysis on the characteristics of cellulose nanoparticle-reinforced poly (methyl methacrylate) composites by assuming that the interaction takes place between the dispersed particles and the matrix. They discovered that adding CNPs to the PMMA matrix reduced the nanocomposites' optical transparency. Rajendran et al. [7] have focused on the addition of lithium tetrafluoroborate ($LiBF_{4-X}$) on the PVA/ PMMA to fabricate a solid polymer electrolyte film, where X is EC, PC, DEC and GBL. The solvent casting method was applied to prepare these films using DMF as a solvent, then samples were stirred under at 70 ^{o}C temperature until the mixture gets homogeneous. In other way Yakuphanoglu and Erten [8] used the spectral measurements across the UV/VIS spectrum regions to study the behavior of the refractive index of PMMA/PVA thin films. Small variations in optical constants and the influence of PMMA concentration on the refractive index can be detected using this approach. Tripathi et al. [9] have engaged the solution casting method to fabricate a PMMA/ PVA to investigate their characteristics and optical properties. In their work, 100 ml of benzene (C_6H_6) was used to dissolve 5 g of PMMA, whereas 100 ml of distilled water was used to dissolve 5 g of PVA. Yang et al. [10] have briefly discussed the recent developments in the fabrication of MOF-polymer composites and their applications. Due to the fact that the union of these two distinct components can give birth to a variety of desired qualities that are not always provided by the separate components, such architectures are becoming increasingly popular in recent literature.

The PMMA polymer was chosen for this investigation because of various qualities, including its safety and chemical inertness. It has also been stated that it is suited for a wide range of imaging and non-imaging microelectronics and sensors. Since PVA is commonly blended with other polymer compounds such as biopolymers and other hydrophilic polymers. The addition of an inorganic substance to the polymeric matrix improves the chemical, structural, and physical characteristics [11]

Polydopamine (PDA), a versatile polymer for surface modification, was developed after being inspired by the process of mussel adhesion. Various PDA-modified nanoparticles have been sought after as drug carriers due to their unique properties such as extraordinary adhesiveness, excellent biocompatibility, low synthesis requirements, distinct drug loading approach, strong photothermal conversion capacity, and reactive oxygen species (ROS) scavenging capability [12].

The aim of this study is to prepare and synthesize the PMMA-PVA thin film mixture and dope it with

different concentrations of PDA nanoparticles using the solution cast method. Then the structural and optical properties of the prepared nanocomposites were studied.

2. Material and Methods

Optical microscopy, Fourier-transform infrared (FTIR) spectrometry and optical properties measurements were carried out to provide a general explanation of the materials used in this work. These materials are PMMA and PVA , while the additive PDA nanoparticles was purchased as a powder from Zhengzhou Dongyao Nano Materials company (China) with a grain size of 50nm and a purity of 99.9%.

The nanocomposites were prepared by dissolving 0.5 g of PMMA with 0.5 g of PVA in 40 ml of pure chloroform using the magnetic stirrer in order to mix the materials to make the solution more homogeneous at room temperature for 30 minutes. After that, the nanoparticles were gradually added to obtain high homogeneity between the mixture and the nanoparticles as the percentage weights of the PDA nanoparticles added to the mixture were 0.5, 2, 3.5, and 5 wt.%. Then the mixture was allowed to stabilize for 15 minutes to get much more homogenous mixture and avoid cracks in the formed composite.

3. Results and Discussion

Figure (1) shows the images of PMMA-PVA/PDA nanocomposite samples with different concentrations of PDA nanoparticles taken at 10X power of magnification 10x. However, it is shown very clearly the differences in the samples labeled A, B, C, D and E.

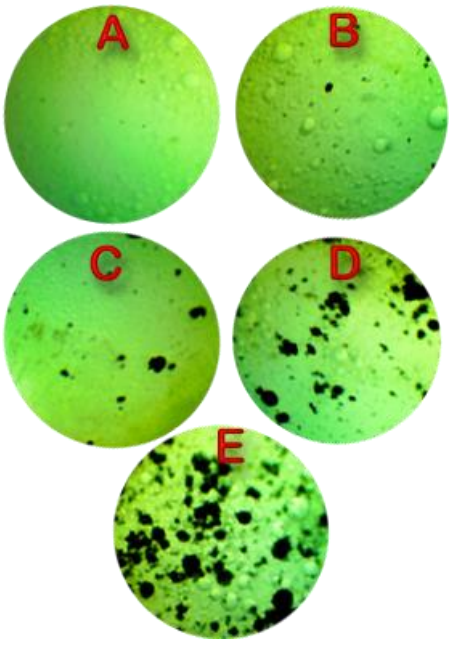

Fig. (1) Photomicrographs (10X) for PMMA-PVA blend (A) and for PMMA-PVA/PDA nanocomposites: (B) 0.5 wt.% PDA, (C) 2 wt.% PDA, (D) 3.5 wt.% PDA, and (E) 5 wt.% PDA

This figure shows that at lower concentrations of PDA nanoparticles, they assemble in a cluster. When increasing the concentrations of PDA nanoparticles in the PMMA-PVA mixture, the nanoparticles create a network of routes.

Throughout investigating the optical properties of PMMA-PVA/PDA, the effect of adding different concentrations of PDA nanoparticles can be determined. This section also identifies the types of electronic transitions and estimating energy gaps, as well as the absorption coefficient, extinction coefficient, and other optical constants.

Figure (2) depicts the absorption spectra of PMMA-PVA/PDA nanocomposite samples as a function of incoming light wavelength. This figure shows that the absorbance for all films is highest at wavelengths around the fundamental absorption edge (310nm), then decreasing as the wavelengths get longer. In the near infrared and visible and regions, the film absorbance is often low. To explain this behavior, when incident photons have insufficient energy to interact with atoms at long wavelengths, the photon will transmit. The interaction between incident photon and substance occurs at shorter wavelengths as the absorbance increases [13-16].

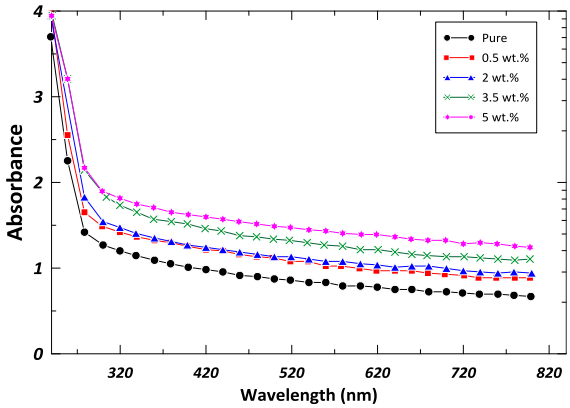

Fig. (2) Absorbance as function of wavelength for PMMA-PVA blend and PMMA-PVA/PDA nanocomposites

The absorption characterized as the ratio of the intensity of light absorbed by the material (I_A) to that of light incident on the material as

$$A = \frac{I_A}{I_0} \quad (1)$$

while the transmittance (T) is given by the ratio of intensity of transmitted light (I_T) to the intensity of incident light (I_0) as:

$$T = \frac{I_T}{I_0} = \exp(-2.303A) \quad (2)$$

and reflectance (R) can be roughly calculated from the law of energy conservation by the relation:

$$R + T + A = 1 \quad (3)$$

Figure (3) illustrates the optical transmittance spectra of PMMA-PVA/PDA films as a function of incident light wavelength when different concentrations of PDA nanoparticles are added. As this concentration increases, the transmittance decreases because PDA nanoparticles with electrons

 ISSN (print) 1813-2065, (online) 2309-1673

in their outer orbits may absorb incident light's energy and go to higher energy levels. Some of the incident light is absorbed by the material and does not pass through it, but the PMMA-PVA mixture has higher transmittance since there are no free electrons. This indicates that electrons are bound to atoms by covalent bonds, because breaking the electron bond and shifting it to the conduction band requires a high-energy photon [14-16].

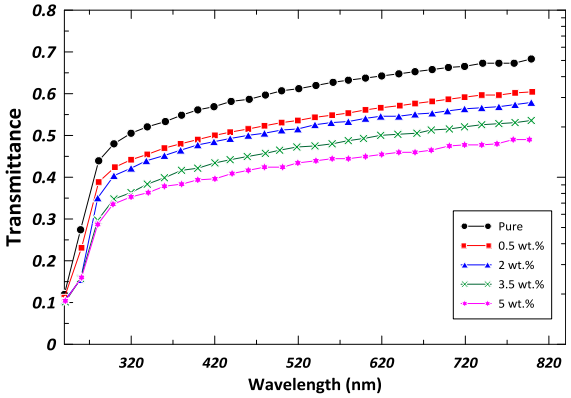

Fig. (3) The transmittance as function of wavelength for PMMA-PVA blend and PMMA-PVA/PDA nanocomposites

Absorption coefficient (α) of PMMA-PVA/PDA composite is defined by following equation:

$$\alpha = 2.303\frac{A}{t} \qquad (4)$$

where A is the absorbance and t is the sample thickness

The energy band gap of the film can be determined by the following formula:

$$\alpha h\nu = B(h\nu - Eg)^r \qquad (5)$$

where B is a constant, $h\nu$ is the photon energy, E_g is the optical energy band gap, r equals 2 for allowed indirect transition and 3 for forbidden indirect transition

Figure (4) depicts the variation of the absorption coefficient for PMMA-PVA/PDA nanocomposites with incident light photon energy. It is clear that the absorption coefficient of nanocomposites is high at higher energies. This means that the electron transition has a high probability; that is, the energy of the incident photon is sufficient to transport the electron from the valence band to the conduction band, which is higher than the energy band gap [15,16]. It is predicted that direct electron transitions would occur when the material's absorption coefficient is high (>10^4 cm^{-1}). When the material's absorption coefficient is low (<10^4 cm^{-1}), it is predicted that indirect electron transitions would occur. The absorption coefficient of PMMA-PVA/PDA nanocomposites is lower than 10^4 cm^{-1}, which indicates that the electron transfer is indirect.

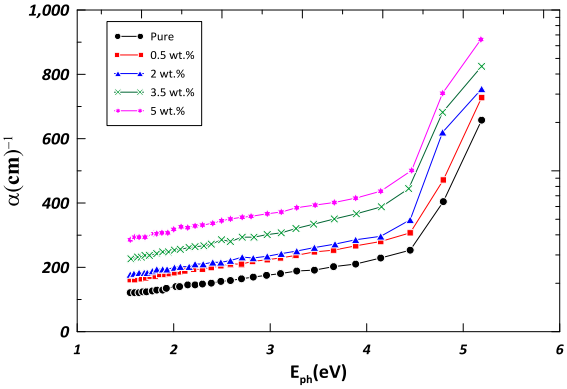

Fig. (4) Variation of absorption coefficient (α) as function of photon energy for PMMA-PVA blend and PMMA-PVA/PDA nanocomposites

The refractive index (n) of the PMMA-PVA/PDA nanocomposite is given by following equation:

$$n = \left(1 + R^{1/2}\right)\left(1 - R^{1/2}\right) \qquad (6)$$

Figure (5) depicts the relationship between the absorption edge $(\alpha h\nu)^{1/2}$ for PMMA-PVA/PDA nanocomposites and photon energy. By drawing a straight line from the upper part of the curve toward the x-axis at the value of $(\alpha h\nu)^{1/2}=0$, the optical energy gap for the allowed indirect transition is obtained. Table (1) shows the obtained results.

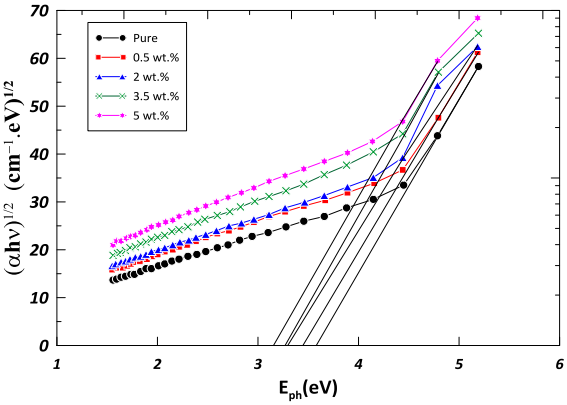

Fig. (5) Variation of $(\alpha h\nu)^{1/2}$ with photon energy for PMMA-PVA blend and PMMA-PVA/PDA nanocomposites

Figure (6) depicts the relationship between photon energy and the absorption edge $(\alpha h\nu)^{1/3}$ for PMMA-PVA/PDA nanocomposites. It can be noticed that when the weight percentage of PDA nanoparticles added to the PMMA-PVA mixture is increased, the value of optical energy gap decreases. This is due to the formation of site levels in the forbidden optical energy gap and the transition in this case occurs in two stages, with the transition of electrons from the valence band to the local levels to the conduction band as a result of increasing the weight percentage of PDA nanoparticles [17]. This results agreed with previous studies [18-20].

Table (1) Values of energy gap for the allowed and forbidden indirect transition for (PMMA-PVA) blend and (PMMA-PVA/PDA) nanocomposite

PDA Nanoparticles (wt.%)	Optical energy gap for indirect transition (eV)	
	Allowed	Forbidden
0	3.580	2.90
0.5	3.425	2.78
2	3.300	2.68
3.5	3.250	2.58
5	3.180	2.40

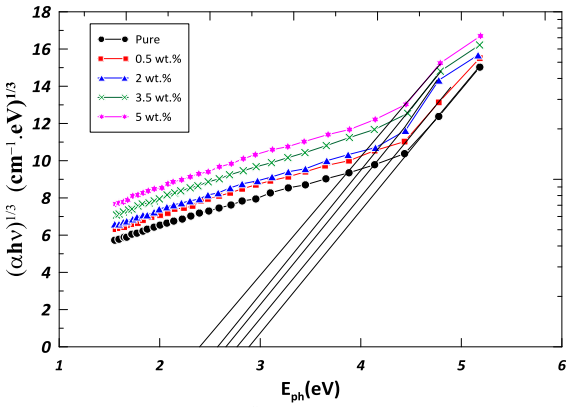

Fig. (6) Variation of $(\alpha h\upsilon)^{1/3}$ with photon energy for PMMA-PVA blend and PMMA-PVA/PDA nanocomposites

The dielectric constant (ε) is divided into two parts real (ε_1) and imaginary (ε_2) those are calculated by the following equations:

$$\varepsilon_1 = n^2 - k^2 \quad (7)$$

$$\varepsilon_2 = 2nk \quad (8)$$

The variation of extinction coefficient of PMMA-PVA/PDA with wavelength is shown in Fig. (7). The obtained results show that increasing concentration of PDA nanoparticles plays a significant role to increase the extinction coefficient owing to increase the optical absorption and photon dispersion in the polymer matrix (PMMA-PVA). Nanocomposites have high values of extinction coefficient in the UV region, which can in turn lead to high absorption by all the nanocomposite samples. The extinction coefficient of nanocomposite increases with wavelength in the visible and near infrared regions as the absorption coefficient is nearly constant in these regions [18-21].

The behavior of refractive index of PMMA-PVA/PDA nanocomposites with incident light wavelength is shown in Fig. (8) as the refractive index of PMMA-PVA/PDA nanocomposites decreases with increasing wavelength. This figure shows that increasing weight percentage of PDA nanoparticles leads to increase the refractive index.

Figure (9) shows the variation of the dielectric constant of PMMA-PVA/PDA nanocomposites with incident wavelength, while figure (10) indicates the influence of adding PDA nanoparticles on the imaginary component of the dielectric constant of PMMA-PVA/PDA nanocomposites. These figures show that when the concentration of PDA nanoparticles is increased, the imaginary and real components of the dielectric constant consequently increase. This result is attributed to an increase in electrical polarization caused by the concentration of nanoparticles in the sample, which means that the increase in dielectric constant of PMMA-PVA mixture indicates a fractional increase in charges inside the polymer. As can be observed, ε_1 is highly dependent on n_2 due to the low value of k_2. Hence the actual dielectric constant increases as the concentrations of PDA nanoparticles is increased. As well, it can be shown that ε_2 is dependent on k, particularly in the visible and near-infrared regions, where the refractive index is nearly constant but the extinction coefficient increases with wavelength according to the relationship between α and k [22,23].

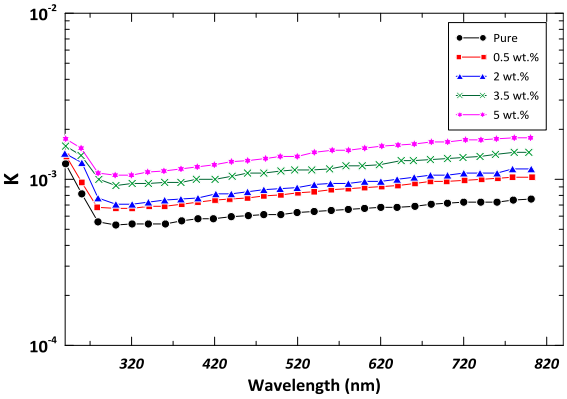

Fig. (7) Variation of extinction coefficient as a function of wavelength for PMMA-PVA blend and PMMA-PVA/PDA nanocomposites

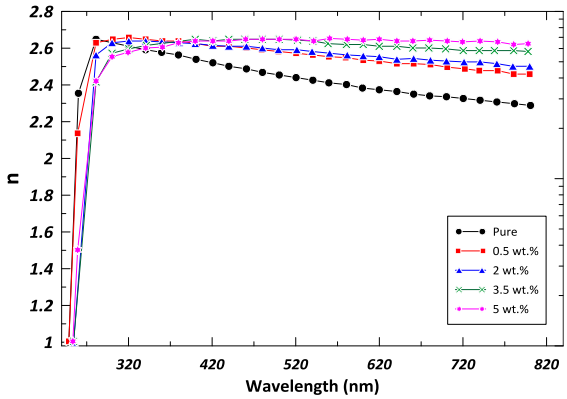

Fig. (8) Variation of the index of refraction with the wavelength for PMMA-PVA blend and PMMA-PVA/PDA nanocomposites

Figure (11) depicts the relationship between optical conductivity and photon energy. The behavior of the PMMA-PVA mixture differs from the behavior of the PDA-doped samples. The optical conductivity increases at low photon energies and subsequently decreases at higher photon energies. This behavior is similar to that of the absorption coefficient since optical conductivity is dependent on the absorption coefficient.

Figure (12) shows the variation of N/N_0 for PMMA-PVA mixture with different concentrations of PDA nanoparticle. As can be seen, the intensity of transmitted radiation decreases as the concentration

 ISSN (print) 1813-2065, (online) 2309-1673

of PDA nanoparticles is increased, which is ascribed to the increase in attenuation. The variation of x-ray attenuation coefficient for the PMMA-PVA mixture as a function of the concentration of PDA nanoparticle is depicted in Fig. (13). According to this figure, the attenuation coefficient increases as the concentration of nanoparticles is increased, which is due to the reflection or absorption of x-rays by the nanocomposite shielding materials. These results are supported by the work of Lu et al. [24].

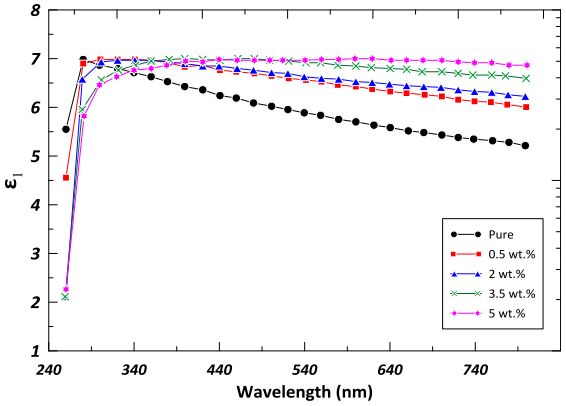

Fig. (9) Variation of real part of dielectric constant with wavelength for PMMA-PVA blend and PMMA-PVA/PDA nanocomposites

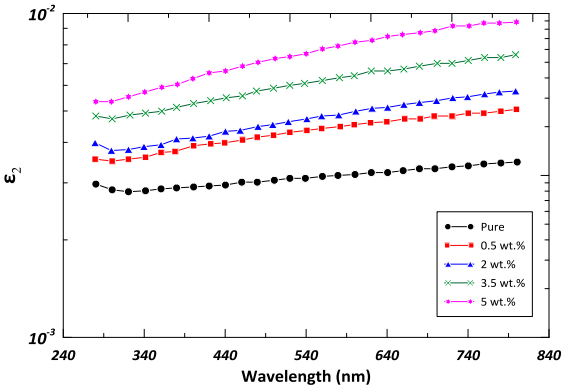

Fig. (10) Variation of the imaginary component of the dielectric constant with wavelength for PMMA-PVA blend and PMMA-PVA/PDA nanocomposites

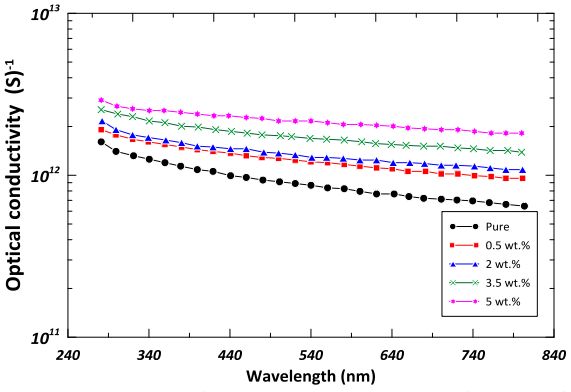

Fig. (11) Variation of optical conductivity as a function of wavelength for PMMA-PVA blend and PMMA-PVA/PDA nanocomposites

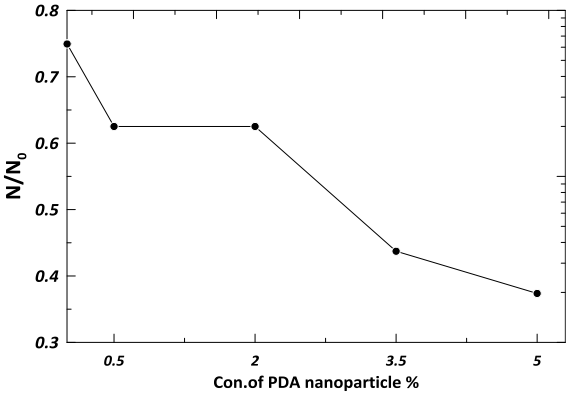

Fig. (12) Variation of N/N_0 with concentration of PDA nanoparticles in PMMA-PV blends

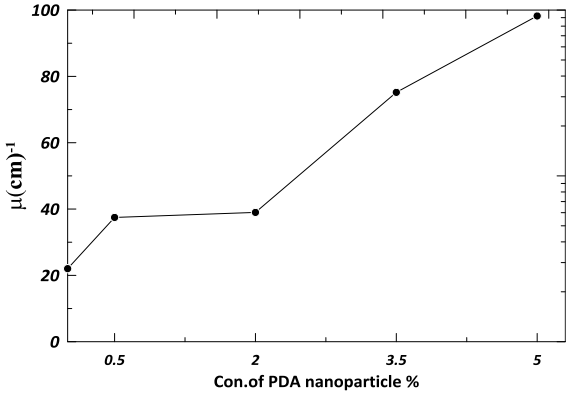

Fig. (13) Variation of x-ray attenuation coefficient with concentration of PDA nanoparticles in PMMA-PV blends

4. Conclusion

The PMMA-PVA/PDA nanocomposites were synthesized in this work using the solution cast process with different weight percentages of PDA nanoparticles (0.5, 2, 3.5, and 5 wt.%). The structural and optical characteristics of these nanocomposites were introduced. It was found that the absorption coefficient, refractive index, extinction coefficient and dielectric constant (real, imaginary) of these nanocomposites increase with increasing the concentrations of PDA nanoparticles added to the PMMA-PVA mixture. On the other hand, the transmittance and energy gap of these nanocomposites was found to decrease with increasing the concentration of PDA nanoparticles. As an application of these nanocomposites, their attenuation coefficient for x-ray was found to increase with increasing the concentration of PDA nanoparticles.

References

[1] D.R. Paul and L.M. Robeson, "Polymer Nanotechnology: Nanocomposites", *Polymer*, 49 (2008) 3187-3204.

[2] N. Taniguchi, "On the Basic Concept of Nanotechnology", in Proc. Int. Conf. on Prec. Eng., Tokyo, Part II, Japan Soc. Prec. Eng., (1974) 3187-3204.

[3] R.V. Kurahatti et al., "Applications of Polymer Nanocomposites", *Def. Sci. J.*, 60 (2010) 551-563.
[4] J.H. Koo, **"Polymer Nanocomposites"**, McGraw-Hill Co. (NY, 2006) p. 138.
[5] F. Deng et al., "Effects of anisotropy, aspect ratio, and no straightness of carbon nanotubes on thermal conductivity of carbon nanotube composites", *Appl. Phys. Lett.*, 90(2) (2007) 21914.
[6] G. Han et al., "Effect of Acid Hydrolysis Conditions on the Properties of Cellulose Nanoparticle-Reinforced Poly methylmethacrylate Composites", *Materials*, 7 (2014) 16-29.
[7] S. Rajendran, M. Sivakumar, and R. Subadevi, "Investigations on the effect of various plasticizers in PVA–PMMA solid polymer blend electrolytes", *Mater. Lett.*, 58(5) (2004) 641-649.
[8] F. Yakuphanoglu and H. Erten, "Refractive index dispersion and analysis of the optical constants of an ionomer thin film", *Opt. Appl.*, 35(4) (2005) 969-976.
[9] J. Tripathi et al., "Effect of PVA concentration on bond modifications in PVA-PMMA blend films", *AIP Conf. Proc.*, 1731 (2016) 1-4.
[10] S. Yang et al., "Enhancing MOF performance through the introduction of polymer guests", *Coord. Chem. Rev.*, 427 (2021) 213525.
[11] R. Etefagh et al., "Synthesis and antimicrobial properties of ZnO/PVA, CuO/PVA, TiO_2/PVA nanocomposites", *Sci. Iran.*, 24 (2017) 1717-1723.
[12] A. Jin et al., "Nanoparticles modified by polydopamine: Working as "drug" carriers", *Bioact. Mater.*, 5(3) (2020) 522-541.
[13] L.N. Ismail et al., "Optical Properties and Surface Morphology of (PMMA-TiO_2) Nanocomposites Thin films", *J. Adv. Mater. Res.*, 364 (2012) 105-104.
[14] M. El-Dahshan, **"Introduction to Material Science and Engineering"**, 2nd ed., King Saud University Press (Saudi Arabia, 2002).
[15] S. Salman, N. Bakr and M.H. Mahmood, "Preparation and study of some optical properties of (PVA-Ni$(CH_3COO)_2$) composites", *Int. J. Curr. Res.*, 6(1) (2014) 9638-9643.
[16] N.B. Rithin Kumar, V. Crasta and B.M. Praveen, "Advancement in microstructural, optical, and mechanical properties of PVA (Mowiol 10–98) doped by ZnO nanoparticles", *Phys. Res. Int. J.*, (2014) 742378.
[17] V. S. Sangawar and M. C. Golchha, "Evolution of the optical properties of Polystyrene thin films filled with Zinc Oxide nanoparticles"', *Int. J. Sci. Eng. Res.*, 4(6) (2013) 2070-2075.
[18] S. B. Aziz et al., "From Insulating PMMA Polymer to Conjugated Double Bond Behavior: Green Chemistry as a Novel Approach to Fabricate Small Band Gap Polymers", *Polymers*, 9(11) (2017) 626.
[19] M.K. Mohammed, G. Al-Dahash and A. Al-Nafiey, "Fabrication and Characterization of the PMMA/G/Ag Nanocomposite by Pulsed Laser Ablation (PLAL)", *Nano Biomed. Eng.*, 14(1) (2022) 15-22.
[20] R.S. Al-Khafaji, K.A. Jasim and A.M. Ibraheim, "Optical and Thermal Characterizations of PMMA Composites", *Eng. Technol. J.*, 37B(2) (2019) 61-67.
[21] K. Khurana, A. K. Patel and K. Das, "Refractive Indices Studies on PVA and PVP Blends", *Int. J. Sci. Res. Develop.*, 4(1) (2016) 984-985.
[22] O.G. Abdullah, "Influence of Barium Salt on Optical Behavior of PVA Based Solid Polymer Electrolytes", *Euro. Sci. J.*, 10(33) (2014) 406-417.
[23] S.HO. Noshi, "Study the Optical and Mechanical Properties of (PMMA-TiO_2) Nanocomposite", M.Sc. thesis, University of Babylon (2014).
[24] W. Lu, Z. Meng and C.H. Zhao-Bin, "Research Progress of Shielding and Shielding Materials of Nuclear Radiation", *Chinese J. Appl. Chem.*, 38(12) (2021) 1576-1587.

 ISSN (print) 1813-2065, (online) 2309-1673

IRAQI JOURNAL OF APPLIED PHYSICS
Vol. 19, No. 1, January-March 2023, pp. 35-40

Eman A.A. Fadhil[1]
Manal M. Abdullah[1]
Fadhel M. Lafta[2]

[1] *Department of Physics, College of Science, University of Baghdad, Baghdad, IRAQ*
[2] *Department of Biology, College of Science, University of Baghdad, Baghdad, IRAQ*

Synthesis of NAC-CdTe/CdS Core-Shell Quantum Dots for Optical Biosensing Applications

This study was set to investigate the utility of quantum dots (QDs) to prepare an optical biosensor with the potential to distinguish damaged DNA (largely associated with malignant diseases) from intact DNA (extracted from healthy individuals). Water-soluble NAC-capped CdTe core shielded with CdS nanocrystals (expressed as CdTe/CdS/NAC nanocrystals) using N-acetyl cysteine as a stabilizer was prepared for biosensing application. Based on the optical characterization of the prepared QDs, the XRD results revealed the formation of the NAC-CdTe/CdS QDs with a grain size of 6.2 nm, while the EDX results emphasized their content of Cd, S and Te elements. The SEM results proposed that the spherical size of the NAC-CdTe/CdS QDs lies within 10-80nm. The demonstrated mono-dispersed lattice structure of NAC-CdTe/CdS QDs that has superior PL emission properties at 573nm and absorption peak at 350nm. The energy gap measurement through PL and UV-visible was found to be 2.1 and 2.5, respectively. Additionally, following the interaction between the synthesized QDs and the extracted genomic DNA (both cancer damaged DNA and healthy undamaged DNA), the results showed a shift in the maximum fluorescence emission intensities (observed at 562nm for a damaged sample and 550nm for a reference cell). Based on the obtained fluorescence results, the present study reached the conclusion that the prepared core/shell QDs could be employed as probes for diagnosing genetically disrupted DNA that is associated with malignant diseases.

Keywords: NAC-CdTe/CdS core/shell nanocrystals; Biosensors; Fluorescence probe; Nucleic acid
Received: 19 December; **Revised:** 23 January 2023; **Accepted:** 30 January 2023

1. Introduction

Quantum dots (QDs) and nanoparticles-based technology represents a major area of interest in the field of developing optical biosensors. with a large number of biomedical applications.This due to their distinctive electronic and optical characteristics including narrow emission bands, broad absorption band, excellent quantum yields, and increased photo-bleaching resistance compared to conventional organic materials [1,2]. The DQs optical properties are surface electronic quantum status dependent. These properties (called states of a surface) are attributed to QDs surface area ratio to volume high [3]. Such characteristics can be either improve or reduce the photo-generated charge carriers' transfer rate. Other characteristics, such as aging effects, the intensity of brilliance and spectrum brands, optical absorption (photoluminescence excitation), quantum efficiency are also seem be affected by the surface states of the QDs [4]. The outer CdS shell of CdTe/CdS quantum dots effectively confines the electron and hole wave-functions inside quantum dots QDs. Thus, QDs are fast becoming key components of a growing area of research exploring their utility for a large number of biomedical applications. These including the preparation of fluorescent probes for the investigation of their use in cell visualization, medical imaging, fluorescent labeling of genomic loci, and many others applications to meet different biological and medical needs [5,6]. Recent trends in QDs research have focused on investigating for their usefulness as fluorescent probes for DNA analysis, which constitutes the genetic makeup of all living organisms [7,8]. It is demonstrated that the prepared QDs were able to distinguish between the different synthesized DNA sequences.These results were based on the optical properties analysis of the interactions between the prepared QDs with the different components of the DNA nucleotides (e.g. the four different DNA nitrogen bases: adenine (A), guanine (G), cytosine (C) and thiamine (T)) that gave different fluorescent emission maximums and intensities [9].

In this paper, the synthesized core/shell structure of NAC capped CdTe core and CdS shell QDs were water-soluble and biocompatible due to utilizing of N-acetyl cysteine as stabilizer. The water-solubility and biocompatibility of the synthesized nanocrystals are attributed to the polar carboxylic acid group of NAC on the out surface of NAC-CdTe/CdS core/shell, and also accessible to interact with various bio-macromolecular including nucleic acids, e.g. DNA. There are relatively few publications in the literature that discuss how core/shell QDs behaves in connection to DNA sequence variation. Thus, this study concentrates on the synthesis of biological sensor concerns with the NAC-CdTe/CdS nanocrystals as a quantitative fluorescent probe for the differentiation between the undamaged (from

normal cells) and the damaged DNA (from malignant cells).

2. Experimental Work

The process of preparing of NAC- CdTe included making two solutions: The first solution was prepared by liquefying 0.189 gm of sodium borohydride ($NaBH_4$) with 0.125 tellurium powder (Te) in 25 ml of distilled water. Then the solution was put into a two-necked round flask with presence of magnetic stirrer to homogenize the solution. Thereafter, nitrogen was pumped in to replace the air and this step was followed by heating the mixture to 70°C. Then the solution was put under nitrogen safeguard for 30 minutes (reaction takes place in the presence of nitrogen to expel oxygen to prevent oxidation), allowing the solution to turn into a dark crimson color. Ultimately, the prepared NaHTe solution was preserved under nitrogen to be used again at room temperature.

The second solution was prepared by adding up to 0.180gm of cadmium chloride ($CdCl_2$) and 0.275 of N-acetyl cysteine (NAC) in 200 ml distilled water. The pH of the mixture was adjusted to 12.0 by dropwise addition of 1.0 M NaOH solution with stirring at room temperature for 1 hour. NAC-capped CdTe nanoparticles were prepared as colloids. The second solution reaction was transferred into a three-necked flask, where nitrogen was added to replace the air. Then, 1mL of the second solution of NaHTe was added by syringe with stirring at room temperature. The mixture then heated to 90°C for 30 minutes. This step was followed by immediately cooling of the heated mixture to room temperature. At the end of the synthesis, excessive NAC–Cd complexes was removed by adding isopropanol to the mixture, the CdTe core QDs were precipitated. The precipitate was re-dispersed in ultrapure water after being produced.

Next, the preparation of NAC-capped CdTe/CdS QDs was performed by adding NAC-capped CdTe core QDs to the nitrogen-saturated solution (containing 0.183g $CdCl_2$, 0.015g Na_2S and 0.815g NAC). In a three-necked flask, the 80 mL CdTe/CdS precursor solution was put after removing the air from the system, and replacing it with nitrogen. The mixture was then heated to 90°C and allowed to react for 20 minutes at this temperature. NAC-capped CdTe/CdS core/shell QD was obtained after cooling into room temperature. The NAC-capped CdTe/CdS core/shell QDs were precipitated by adding isopropanol, and the precipitate was then re-dispersed in ultrapure water [10].

The prepared QDs were assessed for their utility to directly distinguish DNA from different biological sources. Genomic DNA was extracted from blood samples of leukemia patients (representing damaged DNA) and healthy volunteers (representing undamaged DNA). DNA extraction was performed according to the manufacturer instructions using ReliaPrep™ Blood gDNA Miniprep System, Promega, USA. The quality and the concentration of the extracted DNA samples were measured by nanordop (ThermoScientific NanoDrop, USA) [11].

The experimental setting of this part of the study included two main steps: In the first place, an assessment to optical characteristics of the prepared QDs alone was performed. This was performed using characterization measurements including x-ray diffraction patterns (XRD), field-emission scanning electron microscopy (FE-SEM), energy-dispersive x-ray spectroscopy (EDX), Fourier-transform infrared (FTIR) and UV-visible (absorption), and photoluminescence (PL) spectroscopy in order to describe the structures, morphology and spectroscopic characteristics of the prepared QDs.

In the second step, the optical assessment of mixing the prepared core/shell (at different concentrations) with of 3µL of undamaged DNA carried out. This was done using ELISA test that gives the absorption intensity of the different tested samples. Within this context, the absorption intensity refers to the strength of the correlation between the DNA and the QDs. This step helps in determining the optimal correlation between the quantum dots and the DNA for the next step. Similarly, samples composed of 3µL of damaged DNA were mixed with a volume of 100µL of QDs to assess the mixture absorption intensity and compare it with that obtained from mixing the QDs with the undamaged DNA.

3. Results and Discussion

The XRD analysis was used to determine the crystallographic structure of the prepared NAC-capped CdTe/CdS QDs. The diffraction pattern of NAC-capped CdTe/CdS QDs is shown in Fig. (1), where the broad peaks confirm the nanoscale nature. The diffraction pattern exhibits three peaks at 2θ of 24.95°, 25.75°, 36.95°, 43.75° and 50.45°, which correspond to the planes of (100), (111), (102), (220) and (311), respectively.

The average particle size of the synthesized CdTe/CdS QDs (Table 1) was estimated using Scherrer's equation [12]:

$$D = 0.89\lambda/\beta\, cos\theta \quad (1)$$

where D represents the size of crystallite, λ refers to the wavelength of the x-ray source, (CuKα with 1.5406Å), β is the full-width at half maximum (FWHM), and θ is the diffraction angle. Also, the interplanar spacing was accounted using Bragg's Law ($d=n\lambda/2\sin\theta$).

 ISSN (print) 1813-2065, (online) 2309-1673

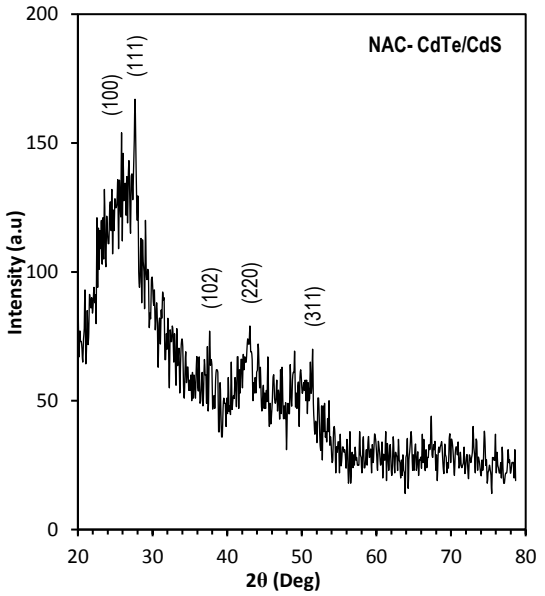

Fig. (1) XRD pattern of the synthesized NAC-capped CdTe/CdS core-shell nanoparticles

Table (1) Determination of grain size of the prepared NAC-capped CdTe/CdS core-shell nanoparticles

Sample	2θ (deg)	FWHM (nm)	d_{hkl} (Å)	D_{ave} (nm)	(hkl)
NAC-CdTe/CdS	24.95	3.2	3.5659	2.5438	(100)
	25.75	6.1	3.4569	1.3365	(111)
	36.95	1.8	2.4308	4.6554	(102)
	43.75	3.4	2. 1134	2. 5102	(220)
	50.45	1.4	1.8074	6.2751	(311)

The FE-SEM image of the prepared NAC-CdTe core with CdS shell QDs nanoparticles is illustrated in Fig. (2a). FE-SEM is a helpful instrument for evaluating the uniformity of material covering across broad areas, as well as the presence of faults or cavities of QDs nanoparticles. Based on that, the surface morphology refers to a non-uniform particle size spreading of NAC-CdTe core with CdS shell QDs nanoparticles on the surface can be evaluated, while the nanoparticles with spherical shapes appeared to be monodispersed with no agglomeration.

Further analysis to the surface view of the prepared NAC-CdTe core with CdS shell QDs reveals the presence of nanoparticles with the circular shapes by particle sizes ranging between 10 to 80 nm. For precise measurements, these profiles were magnified with two different magnification powers; where FESEM test showed an average size of NAC-CdTe/CdS nanoparticles within 200 nm.

As shown in Fig. (2b), there is a typical EDX spectrum verified in the binding energy region of 0-10 keV. This analysis confirms the formation of CdTe:CdS. According to this EDX analysis, the atomic ratio of the cadmium functional group was relatively high. The atomic ratio and weight percentage of Cd is high which reveals the presence of Cd bonding with both S and Te as in the CdS and CdTe compounds. Accordingly, the existence of CdTe quantum dots with pure CdS quantum dots possibly produces materialization of CdTe:CdS nanocomposite [13].

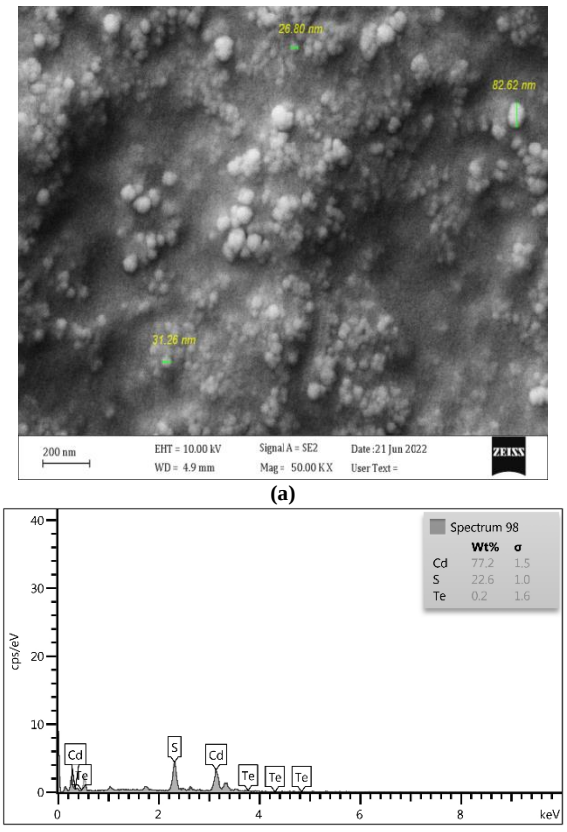

Fig. (2) FE-SEM image (a) and EDX spectrum (b) of the prepared NAC-CdTe/CdS sample

The FTIR spectroscopy is used to certain the conjunction of capping NAC to the CdTe/CdS surface of the prepared quantum dots, as shown in Fig. (3). The characteristic peaks on the NAC curve are located at 3373 and 2550 cm^{-1} and are caused by the asymmetric N-H and stretched S-H vibrations, respectively, of the NAC. Additionally, peaks between 1500 and 1600 cm^{-1}, as well as at 1427 cm^{-1} are indicative of the asymmetric stretching and bending vibrations of the carboxyl group. Furthermore, comparisons between the FTIR spectra of QDs-ANC with those of free NAC revealed clear differences. In which the S-H bond's typical characteristic peak in the QDs -ANC appeared to be vanished, however, the other distinguishing peaks remain unchanged. This demonstrated that the QDs -ANC lacked the S-H bond. These findings indicate that the surface of the QDs had covalent bands connecting the NAC with the cation for QDs. Moreover, the S-H bond in the free NAC contributes to the combination of QDs with DNA. These QDs exhibit exceptional water solubility and effective fluorescence stability, which are shown by the NAC numerous carboxylate groups [14].

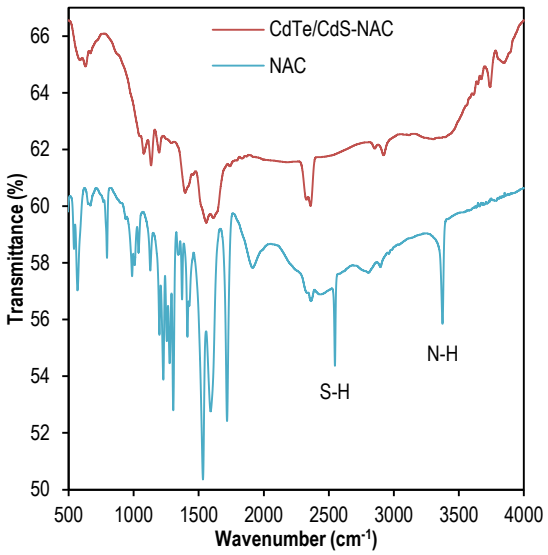

Fig. (3) FTIR spectra of CdTe/CdS -NAC and the free NAC powders

The absorption spectrum of the prepared NAC-CdTe core with CdS shell QDs is shown in Fig. (4). The spectrum of the colloid showed an absorption peak at 288 nm.

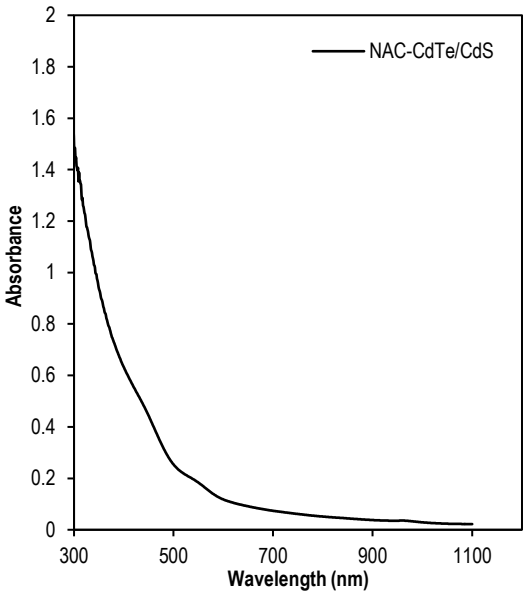

Fig. (4) Absorption spectrum of NAC-capped CdTe/CdS QDs core-shell aqueous solution (colloid)

Additionally, the energy band gap can be determined from the absorption spectra (Tauc's plot) by drawing $(\alpha h\upsilon)^2$ versus $(h\upsilon)$ [15]. The value of the optical direct band gap can be determined by the following relation:

$$\alpha h\upsilon = A(h\upsilon - Eg)^n \quad (2)$$

where α is to the optical absorption coefficient and $h\upsilon$ is the photon energy, A is a constant called band tailing parameter, E_g is the optical band gap, while n is a constant value related to the type of optical transition

The optical absorption coefficient α was determined using the following equation:

$$\alpha = 2.303B/d \quad (3)$$

where B refers to the optical absorbance and d is the sample's thickness or the path length through the quartz cuvette

Furthermore, as illustrated in Fig. (5), the $(\alpha h\upsilon)^2$ versus $h\upsilon$ at which the extrapolation crosses the x-axis is taken as the band gap energy for the NAC-CdTe/CdS QDs sample. The NAC-CdTe/CdS QDs' direct optical band gap energy was determined by extrapolating a line at the linear portion of the curve to be E_g=2.54eV. This coincides with finding presented in Nithyayini and Ramasesha work [16].

The concentration of emitting species, the states relative energies (ground state and excited state), and electronic transitions are precisely examined by PL characteristics. The photons produced by electrons during band-to-band transitions with energy equal to the energy band-gap of the material. Additionally, photons emanate at conduction band (CB) defect levels before attenuating at defect levels in the valence band (VB). Thus, peaks may form below the energy band-gap value, but the outcomes may be impacted by the various transitions. Therefore, the peaks can occur below the energy bandgap value, but the results can be affected due to the different transitions. The PL spectrum results (Fig. 6) showed an emision spectrum of broad band between 547 to 604 nm with a peak located at about 577 nm, as shown in Fig. (6). Energy gap can be calculated from the relation (E_g=1240/λ), which represents the peak of emission in PL [21]. The energy gap obtained for the prepared NAC-CdTe/CdS QD was 2.149 eV. The FWHM of the as-prepared NAC-CdTe/CdS QD is given as in (Fig. 6).

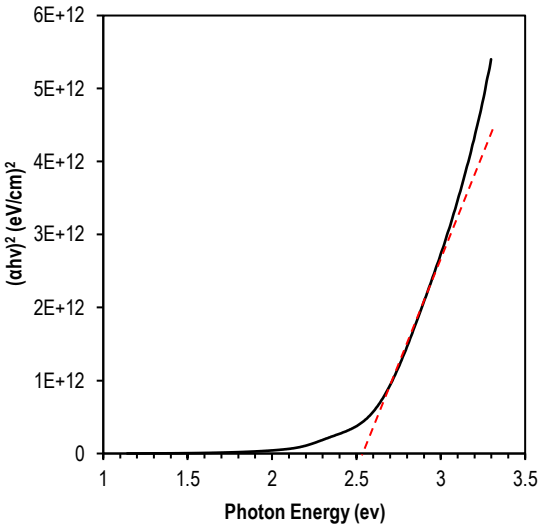

Fig. (5) Relationship of $(\alpha h\upsilon)^2$ vs. photon energy for NAC-capped CdTe/CdS QDs nanoparticle

 ISSN (print) 1813-2065, (online) 2309-1673

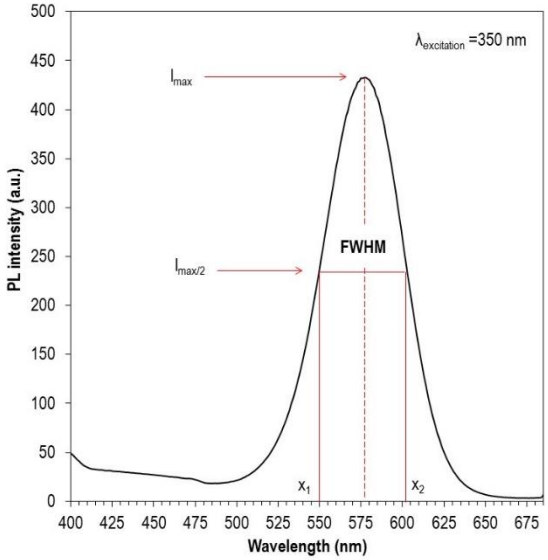

Fig. (6) The photoluminescence (PL) spectrum of the prepared colloidal of NAC-capped CdTe/CdS QDs nanoparticles

The absorption measurement was performed for samples prepared by mixing 3µl of DNA (exracted from healthy individauls) and 100µl of NAC-capped CdTe/CdS at 25µM concentration, which were then placed in 96 well plates in the plant pipets to reach the optimum conditions of the mixing, as shown in Fig. (7). The plate was then inserted in a fully automatic ELISA reader to measure the intensity of absorbency spectrophotometry at different wavelengths (405, 450, 492 and 630nm) were used to assess the absorption spectrum for the mixture. It was found that the best absorption was at wavelength 492 nm which is close to the energy gap calculated for the quantum dots used in the research.

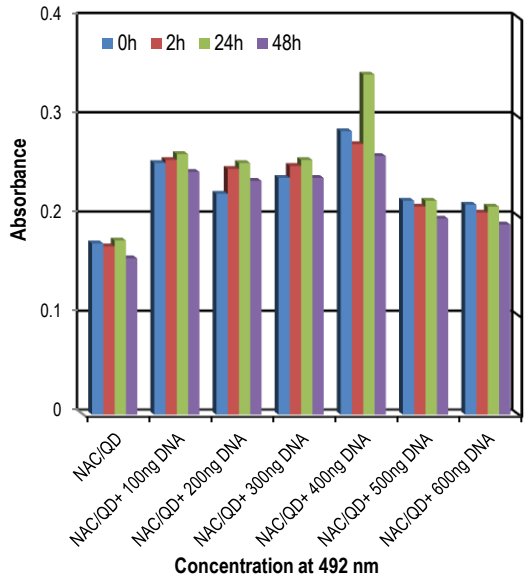

Fig. (7) The relationship between absorbance of NAC-capped CdTe/CdS QDs with different concentrations of reference DNA from healthy subjects

The intensities of absorption spectrum QDs were tested at different concentrations of DNA (Fig. 4). The results showed that the best absorption spectrum intensity was at DNA concentration of 400ng within a time window of 24 hours post conjugation with the prepared QDs. This finding suggests that the NAC-CdTe/CdS core/shell QDs reacted with the DNA to form a complex.

The characteristics of fluorescence of the prepared NAC-capped CdTe/CdS with the presence and without DNA (reference and defective DNA) were recorded to disclose the ability and efficacy of the NAC/QDs in distinguishing damaged from undamaged DNA. After mixing 25µM of the QDs with the best concentration of the conjugated DNA (400ng/µL), the mixture was assessed by fully automatic ELISA reader to measure the intensity of the absorbency spectrophotometry of the aqueous solution of undamaged DNA. The results showed that maximum emission peak of NAC/QDs was shifted from 580 to 550 nm by the interaction with the undamaged DNA. However, at the same concentrations of damaged DNA conjugated with NAC/ QDs, emission maxima peak of the NAC/QDs was shifted from 580 to 562 nm (Fig. 8 and Table 2). This varies clearly and significantly from that of the undamaged DNA samples (550nm). Collectively, comparing these values exhibits a distinguishable shift of 30nm for the reference DNA samples, and 12nm for the damaged DNA samples Based on the FWHM analysis, the fluorescent emission spectra for the damaged DNA samples is wider and more intense from those of the undamaged DNA samples. Through this result CdTe/CdS/NAC can be used for the development of fluorescent probe for detection of damage DNA that represents the root of a number of health problems [9].

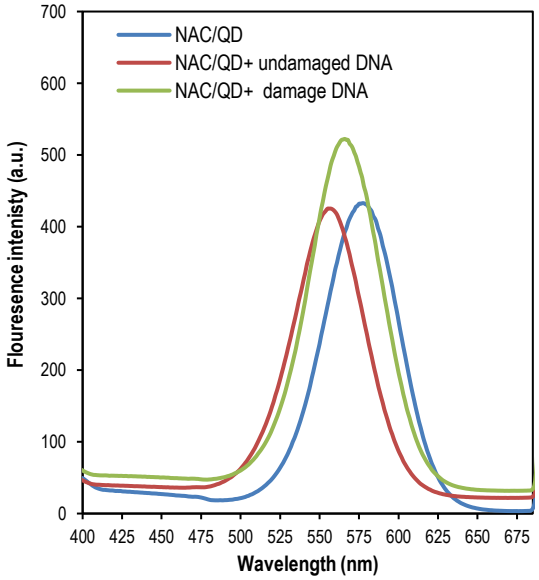

Fig. (8) The fluorescence spectra of the NAC/QDs control, the NAC/QDs with damaged DNA, and NAC/QDs with undamaged DNA

Table (2) data of fluorescence parameters for the prepared and the conjugated core-shell QD

Sample	Peak (nm)	FWHM (nm)	Maximum Intensity (a.u.)	E_g (eV)
QD_S	580	57	439	2.137
QD_S+ undamaged DNA	550	56	422	2.254
QD_S+ damaged DNA	562	61	514	2.206

4. Conclusions

Based on the varying and distinguishable fluorescence spectra observed by conjugating the prepared NAC-capped CdTe/CdS QDs with damaged and undamaged DNA extracted samples, the present study reached to conclude that the synthesized NAC-CdTe core with CdS shell QDs could be employed in developing optical biosensors for a variety of biomedical applications, especially those related to the detection of genomic integrity.

References

[1] A.V. Isarov and J. Chrysochoos, "Optical and photochemical properties of nonstoichiometric cadmium sulfide nanoparticles: surface modification with copper (II) ions", *Langmuir*, 13 (1997) 3142-3149.

[2] Y. Yin and D. Talapin, "The chemistry of functional nanomaterials", *Chem. Soc. Rev.*, 42 (2013) 2484-2487.

[3] W. Chidawanyika et al., "Photophysical study of a covalently linked quantum dot–low symmetry phthalocyanine conjugate", *J. Photochem. Photobiol. A: Chem.*, 212 (2010) 27-35.

[4] B. Sun et al., "Microminiaturized immunoassays using quantum dots as fluorescent label by laser confocal scanning fluorescence detection", *J. Immunolo. Meth.*, 249 (2001) 85-89.

[5] H. Zhang, L. Wang and W. Jiang, "Label free DNA detection based on gold nanoparticles quenching fluorescence of Rhodamine B", *Talanta*, 85 (2011) 725-729.

[6] Z. Liu et al., "A novel quantum dots-based OFF–ON fluorescent biosensor for highly selective and sensitive detection of double-strand DNA", *Sens. Actuat. B: Chem.*, 176 (2013) 1147-1153.

[7] J. Tian et al., "Detection of influenza A virus based on fluorescence resonance energy transfer from quantum dots to carbon nanotubes", *Anal. Chim. Acta*, 723 (2012) 83-87.

[8] A. Moulick et al., "Application of CdTe/ZnSe quantum dots in in vitro imaging of chicken tissue and embryo", *Photochem. Photobiol.*, 91 (2015) 417-423.

[9] A. Moulick et al., "Using CdTe/ZnSe core/shell quantum dots to detect DNA and damage to DNA", *Int. J. Nanomed.*, 17 (2022) 1609-1611.

[10] S. Huang et al., "A CdTe/CdS/ZnS core/shell/shell QDs-based "OFF–ON" fluorescent biosensor for sensitive and specific determination of L-ascorbic acid", *RSC Adv.*, 4 (2014) 46751-46761.

[11] F.A.A. Shafi et al., "Effect of exercise, synthetic anabolic steroids and protein intake on DNA damage in trained and untrained men", *Meta Gene*, 24 (2020) 100685.

[12] S.K. Mustafa, R.K. Jamal and K.A. Aadim, "Studying the Effect of Annealing on Optical and Structure Properties of Zno Nanostructure Prepared by Laser-Induced Plasma", *Iraqi J. Sci.*, 60(10) (2019) 2168-2176.

[13] G. Ramalingam et al., "Structural and Optical Properties of CdSe/CdTe Core-Shell Quantum Dots", *J. Nanomater.*, (2022) Article 6316716.

[14] Q. Xiao et al., "Facile synthesis and characterization of highly fluorescent and biocompatible N-acetyl-L-cysteine capped CdTe/CdS/ZnS core/shell/shell quantum dots in aqueous phase", *Nanotechnol.*, 23 (2012) 495717.

[15] I.N. Mihailescu (ed.), **"Synthesis and Modification of Nanostructured Thin Films"**, MDPI (Basel, 2020), 153.

[16] Z.Gu et al., "One-pot synthesis of highly luminescent CdTe/CdS core/shell nanocrystals in aqueous phase", J. Nanotechnol., 19 (2008) 135604.

[17] E.A. Fadhil and M.M. Abdullah, "CdSe/ZnS core/shell for luminescent solar concentrator", *Iraqi J. Sci.*, 61(7) (2020) 1645-1649.

 ISSN (print) 1813-2065, (online) 2309-1673

IRAQI JOURNAL OF APPLIED PHYSICS
Vol. 19, No. 1, January-March 2023, pp. 41-46

Comparative Analytical Study of Some Stainless Steels Using LIBS, XRD, XRF and EDS Techniques

Hyder A. Salih[1]
Qusay A. Abbas[2]
Khaleel I. Hassoon[1]

[1] *Department of Applied Sciences, University of Technology, 10066 Baghdad, IRAQ*
[2] *Department of Physics, College of Science, University of Baghdad, IRAQ*

The ability to identify stainless steel using precise and fast techniques can be critical in engineering applications. Moreover, the ability to sort different types of stainless steel is crucial in recycling of scrapes as well as in engineering applications. In this work, we present a comparative study to identify commercial stainless steel using laser induced breakdown spectroscopy technique (LIBS) and three other traditional techniques namely, x-ray diffraction (XRD), x-ray fluorescence (XRF) and energy dispersive x-ray spectroscopy (EDS). This study attempts to compare the ability of LIBS and the three conventional techniques of characterization between the three more common types of stainless steel namely, stainless steel 304 (SS304), stainless steel 316 (SS316), and Ferritic stainless steel (SSFER). The standard XRD technique is also used to study the crystalline structure of the stainless-steel. The results showed that LIBS and XRF techniques are more sensitive to the elemental components than the others. However, EDS has an advantage of giving the elemental surface distribution. It is recommended to use the above techniques collectively since one technique can be more sensitive to certain elements than the others.

Keywords: Stainless steel; LIBS; X-ray fluorescence; Biomedical engineering
Received: 30 November 2022; **Revised:** 11 December 2022; **Accepted:** 18 December 2022

1. Introduction

Stainless steel (SS) is an important material with numerous applications in food preparation, culinary tools, kitchen sinks, surgical tools and biomedical applications [1-5]. Identification of the toxic metals that released from SS and recycling process of SS need to accurate, fast, portable, and low-cost devices to classify both the diverse types and components of SS [6]. In the past, several standard techniques have been used to identify various kinds of SS such as x-ray fluorescence (XRF) [7,8], energy dispersive x-ray spectroscopy (EDS) [9], Fourier-Transform Infrared (FTIR) spectroscopy [10], and atomic absorption spectroscopy [11]. However, in the last decade some researchers started to use laser-induced breakdown spectroscopy technique (LIBS) as a fingerprint for some metals and alloys. For example, Fadhil *et al.* [12] used LIBs technique to identify two forms of silver. Khalil *et al.* [13] studied some parameters for plasma generated from austenitic stainless steel by using LIBS technique. The spectrum is recorded in the UV region. The group noted that the intensity of line (Fe I 275.01) resulted from double pulses could be higher by a factor about 60 times compared with single pulse. In 2015, Kshiwakura and Wagatsuma [6] used a laboratory-built LIBS system to study the feasibility of using LIBS for sorting of several types of binary alloys such as Fe–Ni, Fe–Cr and Fe–Mo. They confirmed that by utilizing some parameters like longer gate width, shorter delay, and a greater number of laser shots time, the LIBS system can be used for sorting process by detecting the amount of molybdenum, chromium, and nickel in the samples. In another study,

In 2018, Lang *et al* [14] used LIBS to detect contaminations of some elements such as Cs and Sr on the surface of SS304 type. They found that some emission lines such as Cs I (894.35 nm) and Sr II (407.77 nm) lines might be easily separated from the total emission spectra. In the same year, Noll *et al.* [15] reviewed developments of LIBS research from 2014 to 2018. In another study, Lévesque *et al.* [16] showed that some spectral lines emitted from the impurities in SS and Al can be clearly identified in the UV-visible regions when a focused laser beam with high electric field that is about 10 times the air electrical breakdown. It is worthwhile to mention that stainless steel analysis is challenging due to the wide variability in elemental concentrations when compared to the low alloy family of steels. Low alloy steels contain of at least 90% of iron alloyed and 10% of other elements, such as C, Cr, Ni, Mo, Si and Al. SS304 and SS316 are the most common stainless steel [17]. These two types are widely used in cutlery, cookware, and kitchen tools. Compared with SS304, SS316 contains some molybdenum to increase resistance against acids and certain localized attacks such pitting and crevice corrosion. Ferritic stainless steel or SSFER is another type of the stainless-steel families. Using human senses, it is quite difficult to differentiate between SS304 and SS316 since there is no tangible difference between the two. One method

is to test them chemically. The main difference between SS304 and SS316 stainless steel is that SS316 has additional amount of molybdenum [18]. There are many researches that suggest using LIBS system as a fast device to differentiate between diverse types of stainless steel [6]. However, little works have been devoted to compare the results of LIBS with the other standard techniques.

In this work, we employed LIBS and several standard techniques to identify the differences between three common types of stainless steel.

2. Experimental Part

The LIBS's system used in this study consists of an Nd:YAG pulsed laser (HUAFEI) with wavelength of 532nm (second harmonic generation mode) and frequency of 1 Hz, a lens with a focal length 10 cm, an optical fiber, a THORLAB CCS100 compact spectrophotometer (SP) with dimensions of 29.5x79x122mm^3 (350-700 nm). Figure (1) displays a schematic diagram of the used system.

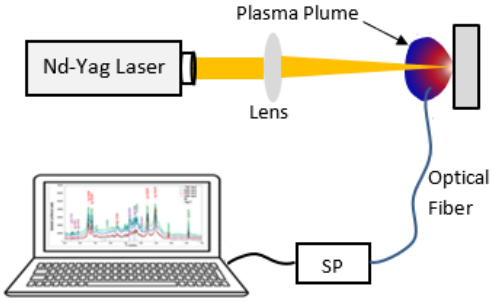

Fig. (1) Schematic diagram of LIBS setup to identify emission lines of SS304, SS316 and SSFER

The signal from the compact spectrometer (Czerny-Turner) was integrated on the ICCD detector. To analyze the emission signal from the sample, the number of laser shots are varied from 1 to 10. The measurement was conducted five times to choose the one with the most obvious spectrum. Since the purpose is to identify and sort stainless samples, we used only commercial samples of SS304, SS316 and SSFER with dimensions (2x2x0.1cm^3). Spectrum Analyzer 1.7 software [19] was used to match the emission lines with input data from NIST data base [20]. Only the first ionization emission lines are recorded. Energy-dispersive x-ray (EDS) spectroscopy was achieved by Axia Chemi EDS with mapping facility. XRF measurements were done by Spectro model XEPOS. The data for structural properties were measured using Haoyuan X-ray diffractometer and the x-ray data have been analysed with the help of Match software.

3. Results and Discussion

In general, LIBS spectroscopy can show many intense lines of Cr, Ni and Mo that appeared in the ultraviolet region. However, in this work, the spectral range 370-570nm was chosen since the line emissions of the elements are clearly distinguished at this range and relatively free from iron interference.

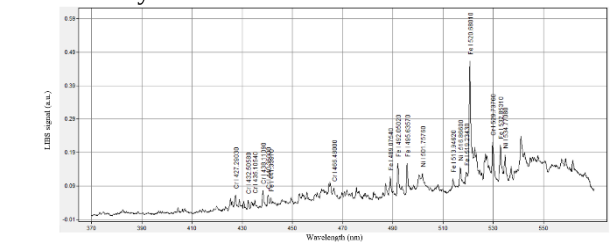

(a)

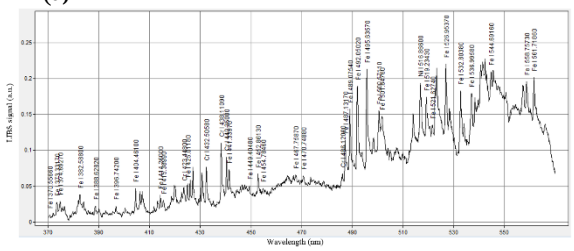

(b)

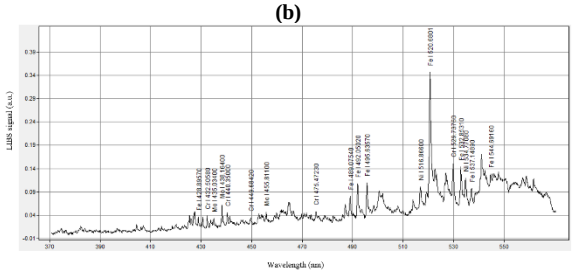

(c)

Fig. (2a) shows emission lines of LIBS for Ferritic martensite stainless (FERSS). There are three strong lines for iron and the most prominent one is Fe(I) 520.68 nm. There are also two strong lines for Cr, and Ni where no Mo emission lines are identified in this phase.

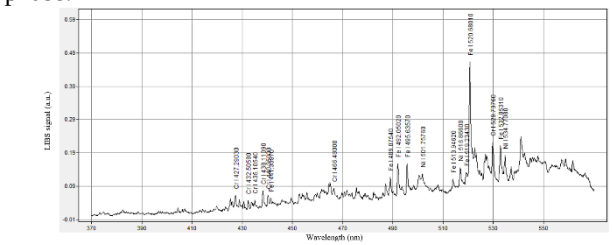

(a)

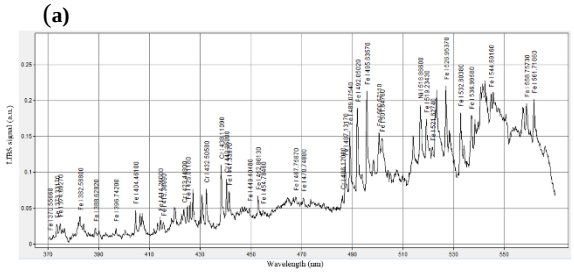

(b)

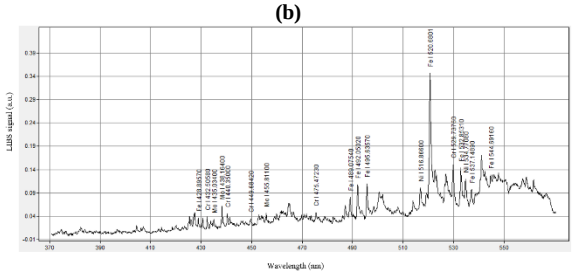

(c)

 ISSN (print) 1813-2065, (online) 2309-1673

Fig. (2b) indicates LIBS emission lines of SS316 with two lines for molybdenum.

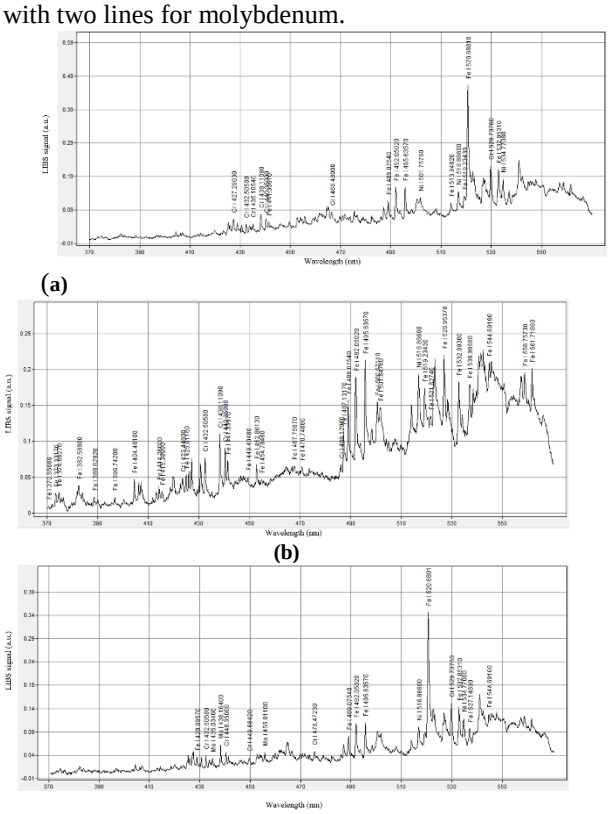

(a)

(b)

(c)

Fig. (2c) reveals LIBS for SS304 with three lines for iron and the most prominent one in this study is Fe(I) 520.68 nm. There are also two lines for chromium with one interfered with at molybdenum at 438.16 nm. Other peaks for Fe, Cr, Ni, Mo, Si are also available but they are a bit tiny. The strongest spectral lines are indicated in Table (1).

Table (1) Wavelengths of spectral lines of three types of stainless steel

SSFER	Wavelength	SS316	Wavelength	SS304	Wavelength
Fe I	441.334	Fe I	492.05	Fe I	492.05
	489.075		495.64		495.64
	492.050		519.23		520.68
	485.636		526.95		
	513.946		532.80		
	519.234		537.00		
	520.680		558.76		
	532.853		561.72		
Cr I	438.110	Cr I	432.51	Cr I	427.29
	529.740		438.11		438.11
	-		486.12		
Ni I	501.760	Ni I	516.86	Ni I	501.76
	516.860		534.77		516.86
	534.770		-		534.77
Mo	-	Mo	438.16	Mo	438.16
	-		455.18		455.18

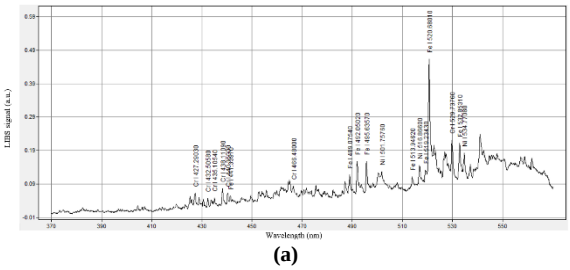

(a)

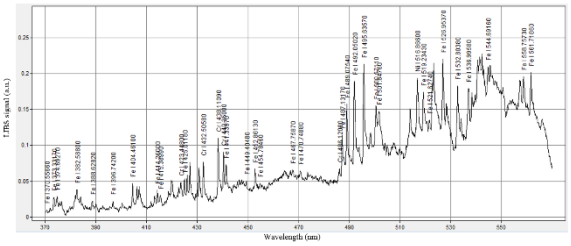

(b)

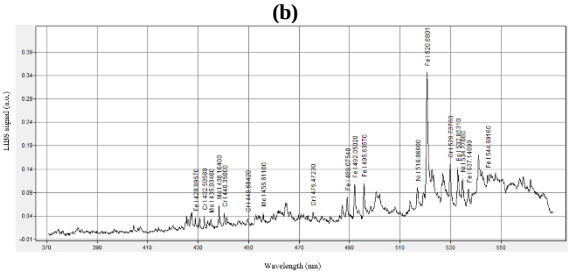

(c)

Fig. (2) LIBS signal as a function of wavelength in nanometer unit for (a) SSFER (b) SS304 (c) SS316.

The XRD patterns of SS304, SS316 and SSFER are shown in Fig. (3), where there are three peaks for SS304 and SS316 and only two peaks for SSFER. These samples revealed peaks at 2θ=43.8°, 50.8° and 74.8° corresponding to crystalline planes (111), (200) and (220), respectively. The peaks are almost sharp (with narrow FWHM). So, the samples have a crystalline structure. The figure indicates that SSFER has a different XRD pattern from SS304 and SS316 and this feature can be utilized to differentiate SSFER from other phases. The phases SS304 and SS316 have almost the same pattern. This is due to SS304 and SS316 have face centered cubic crystalline structure called γ-Fe or Austenite while Ferritic SS has a body centered cubic crystalline structure called α-Fe or martensite. Moreover, the phase structure and diffraction peaks namely α-Fe (110) and (211) of SS304 is composed of α-Fe martensite phase and γ-Fe phase. The d-values of the observed peaks are calculated using Bragg's equation nλ=2dsinθ, as shown in steel (**SS304, SS316 and SSFER)**

Table (2) with λ=0.1518nm. The slight difference between the locations of 2θ in SS304 and SS316 is due to different elements composition ratios. The results are compatible with previous studies [21, 22].

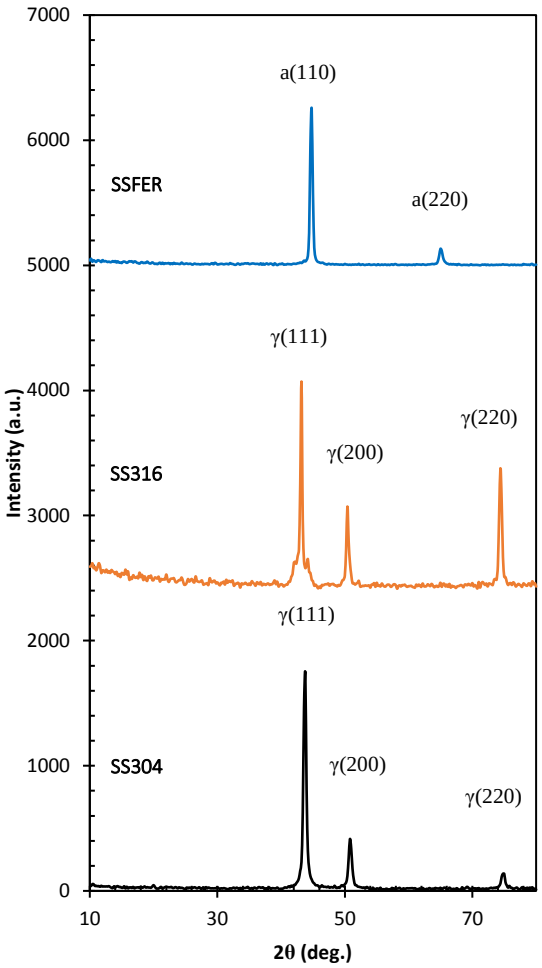

Fig. (3) XRD patterns of three commercial types of stainless steel (SS304, SS316 and SSFER)

Table (2) X-ray parameters for three types of stainless steel. (θ) Bragg's angle, (β) the full-width at half maximum, (d) d-spacing, (a) lattice constant, (D) crystallite size. Scherrer's analysis was used to calculate the crystallite size (D). Defects density ($\delta = 1/D^2$)

Sample	2θ (deg)	β (deg.)	d (nm)	a (nm)	D (nm)	δ (x10^{11}) cm^{-2}
SS304	43.8	0.40	0.206	0.358	22.4	2.00
	50.8	0.60	0.179	0.359	15.3	4.26
	74.8	0.80	0.127	0.359	13.1	5.85
SS316	43.2	0.40	0.209	0363	22.3	2.00
	50.4	0.40	0.181	0.362	22.9	1.89
	74.4	0.60	0.127	0.361	17.4	3.31
SSFER	44.8	0.40	0.20	0.350	22.4	1.98
	65.1	0.60	0.14	0.287	16.4	3.70

Table (3) Chemical composition of stainless steel in mass (%)

SS Structure	Cr	Ni	Mo	Si	Mn	Co	Fe
SS304	17.45	9.60	0.12	-	0.41	0.41	Balance
SS316	17.06	9.80	0.33	-	0.30	0.30	Balance
SSFER	0.110	0.28	0.04	-	0.34	0.34	Balance

In general, XRF analysis can provide with dependable quantitative information about the elemental composition of SS304, SS316 and SSFER [23]. However, in this study, XRF analysis for SS316 did not show an appreciable content of Mo (Fig. (4). Table (3) shows that the main components of SS304 and SS316 are Fe, Cr and Ni. The results like those in references [24] and [25]. The results of EDS examination are displayed in Fig. (4). In that figure, the signal of EDS for stainless steel is plotted as a function of electron energy in keV unit. All the peaks belong to the elemental components of stainless steel namely Fe, Cr, C, Ni and Mo. The results are in a good agreement with Costa et al. [26].

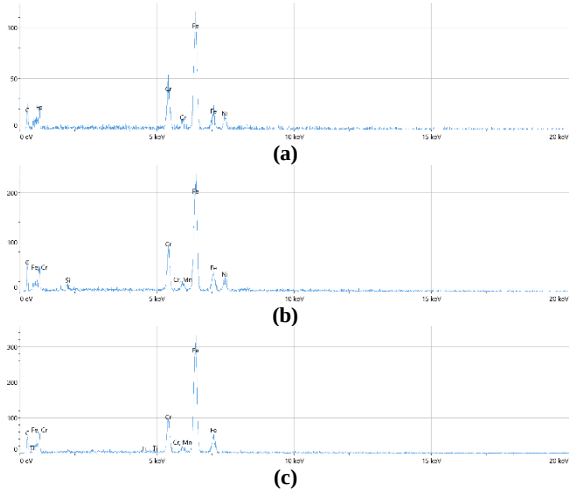

Fig. (4) EDS results of three commercial types of stainless steel (SS304, SS316 and SSFER)

Figures (5), (6) and (7) show EDS mapping for SS304, SS316 and SSFER, respectively. Unlike point analysis, these figures reveal the elements distribution across the scanned area. During the EDS measurement, different areas were focused and scanned. Using atomic absorption spectroscopy and XRF as analytical techniques, Ognjanović and Grgur [27] have shown that austenite and ferrite stainless steel had a different chemical composition than the nominal composition. This means that XRF can give a smaller content of chromium than the nominal content. Moreover, smaller content of carbon was also expected.

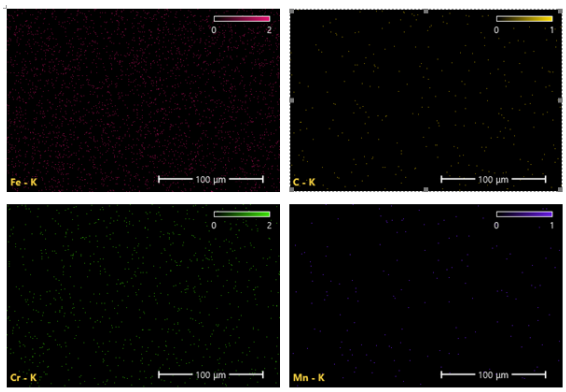

Fig. (5) EDS mapping images for SS304 showing the surface distribution for Fe, Cr, Ni, and C

 ISSN (print) 1813-2065, (online) 2309-1673

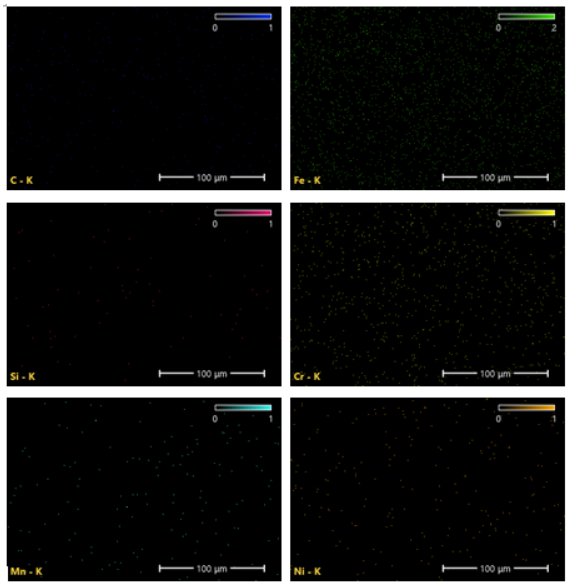

Fig. (6) XRF mapping images for SS316 showing the surface distribution for Fe, Cr, Ni, and C

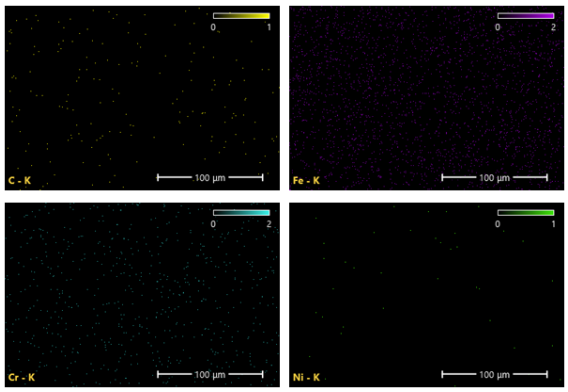

Fig. (7) EDS mapping for SSFER showing the surface distribution for Fe, Cr, Ni, Mn, Si and C

4. Conclusions

For the identification of the most common kinds of stainless-steel, LIBS, XRD, XRF and EDS spectroscopy can be used. LIBS is shown to be the fastest technique to give an accurate identification for stainless-steel. XRD can be used to identify α phase samples of stainless-steel. LIBS and XRF are more sensitive to the elemental components than the others. However, EDS has an advantage of giving the elemental surface distribution. Finally, for more accurate classification, it is recommended to use LIBS, XRF and EDS techniques collectively since one technique is more sensitive to certain elements than the others.

References

[1] A.K. Dewangan, A.D. Patel and A.G. Bhadania, "Stainless steel for dairy and food industry: a review", *J. Mater. Sci. Eng.*, 4(5) (2015) 1-4.
[2] H.A. Abdullah, A.M. Al-Ghaban and R.A. Anaee, "Deposition of CeO_2/TCP thin film on stainless steel 316 L by RF sputtering", *Eng. Tech. J.*, 39(4) (2021) 625-631.
[3] R.B. Durairaj et al., "Effect of plasma sprayed α-tri-calcium phosphate (α-TCP) deposition over metallic biomaterial surfaces for biomedical applications", *Dig. J. Nanomater. Biostruct*., 15(2) (2020) 345-358.
[4] S. Al-Rubaiey, I. Abdl Aziz and A. Khashin, "Effect of applied stresses on corrosion behavior of 304 stainless steel in 1N H_2SO_4", *Eng. Tech. J.*, 34(3) (2016) 609-612.
[5] J. Kuligowski and K.M. Halperin, "Stainless steel cookware as a significant source of nickel, chromium, and iron", *Arch. Enviro. Contam. Toxicol.*, 23(2) (1992) 211-215.
[6] S. Kashiwakura and K. Wagatsuma, "Rapid sorting of stainless steels by open-air laser-induced breakdown spectroscopy with detecting chromium, nickel, and molybdenum", *Iron Steel Inst. Japan Int.*, 55(11) (2015) 2391-2396.
[7] D. Garai et al., "Structure of the surface region of stainless steel: bulk and thin films", *phys. stat. sol. (b)*, 259(4) (2022) 2100513.
[8] R. Dalipi et al., "Study of metal release from stainless steels in simulated food contact by means of total reflection X-ray fluorescence", *J. Food Eng.*, 173 (2016) 85-91.
[9] A. Kocijan, I. Milošev and B. Pihlar, "The influence of complexing agent and proteins on the corrosion of stainless steels and their metal components", *J. Mater. Sci.: Materials in Medicine*, 14(1) (2003) 69-77.
[10] A. Rajasekar and Y.P. Ting, "Role of inorganic and organic medium in the corrosion behavior of Bacillus megaterium and Pseudomonas sp. in stainless steel SS 304", *Ind. Eng. Chem. Res.*, 50(22) (2011) 12534-12541.
[11] P. Haudrechy et al., "Nickel release from 304 and 316 stainless steels in synthetic sweat. Comparison with nickel and nickel-plated metals. Consequences on allergic contact dermatitis", *Corr. Sci.*, 35(1-4) (1993) 329-336.
[12] H.M. Fadhil, K.I. Hassoon and H.A. Salih, "Structural and spectroscopic analysis for silver bulk and nanoparticles", *Karbala Int. J. Mod. Sci.*, 8(2) (2022) 52-62.
[13] A.I. Khalil et al., "Double pulse UV laser induced breakdown spectroscopy of stainless steel", *J. Appl. Spectro.*, 73(5) (2006) 735-742.
[14] A. Lang et al., "Analysis of contaminated nuclear plant steel by laser-induced breakdown spectroscopy", *J. Hazard. Mater.*, 345 (2018) 114-122.
[15] R. Noll et al., "LIBS analyses for industrial applications – an overview of developments from 2014 to 2018", *J. Anal. Atom. Spectro.*, 33(6) (2018) 945-956.
[16] L. Luc, K. Woodcock and D. Prezgot, "Laser-induced emission spectra of stainless steels and aluminum irradiated with nanopulse lasers without

setting delay: potential applications to remote sensing and laser micromachining", *Appl. Opt.*, 61(27) (2022) 7937-7947.
[17] L. Kamerud, A.K. Hobbie and K.A. Anderson, "Stainless steel leaches nickel and chromium into foods during cooking", *J. Agricul. Food Chem.*, 61(39) (2013) 9495-9501.
[18] Y. Helmi, **"Machining of Stainless Steels and Super Alloys"**, John-Wiley & Sons (2016) 12.
[19] Z. Navrátil et al., "A software for optical emission spectroscopy - problem formulation and application to plasma diagnostics", *Czechoslovak J. Phys.*, 56(suppl. B) (2006) B944-951.
[20] physics.nist.gov/PhysRefData/ASD/lines_form.html
[21] B. Uzer and D. Canadinc, "The effect of plastic deformation on the cell viability and adhesion behavior in metallic implant materials", *Process. Prop. Des. Adv. Cer. Comp. II*, 261 (2017) 187.
[22] S.Y. Lee et al., "Dynamic strain evolution around a crack tip under steady-and overloaded-fatigue conditions", *Metals*, 5(4) (2015) 2109-2118.
[23] P. Dhaiveegan et al., "Corrosion behavior of 316L and 304 stainless steels exposed to industrial-marine-urban environment: field study", *RSC Adv.*, 6(53) (2016) 47314-47324.
[24] E.A. Eid, M.M. Sadawy and A.M. Reda, "Computing the dynamic friction coefficient and evaluation of radiation shielding performance for AISI 304 stainless steel", *Mater. Chem. Phys.*, 277 (2022) 125446.
[25] A.K. Hamzat, A.M. Memon and L.M. Alhems, "Novel assessment of in-operations mapped stainless steel elbow pipe internal wall for detection of corrosion and scale deposition", *Int. J. Corros. Scale Inhib.*, 11(4) (2022) 1496-1515.
[26] G.C. Costa et al., "Oxidation behavior of stainless steels 304 and 316 under the Venus atmospheric surface conditions", *Corros. Sci.*, 132 (2018) 260-271.
[27] V. Rajaković-Ognjanović and B.N. Grgur, "Corrosion of an austenite and ferrite stainless steel weld", *J. Serbian Chem. Soc.*, 76(7) (2011) 1027-1035.

 ISSN (print) 1813-2065, (online) 2309-1673 PRINTED IN IRAQ

Iraqi Journal of Applied Physics Letters (IJAPLett) returns back again

By
Oday A. Hammadi
Editor-In-Chief, IJAP

In April 2008, the first issue of Iraqi Journal of Applied Physics Letters (IJAPLett) was released as a new journal derived from the Iraqi Journal of Applied Physics (IJAP) to publish research letters on the same disciplines of IJAP but rather extended to include Alternative & Renewable Energy, Applied Mechanics & Thermodynamics, Applied Optics & Optical Design, Biophysics & Bioengineering, Cryptography & Applications, Electromagnetic Fields, Electronic Materials & Devices, Energy Generation & Conversion, Fluids Physics & Mechanics, Imaging, Microscopy & Spectroscopy, Laser Physics & Applications, Magnetism & Applications, Instrumentation, Measurements & Metrology, Nanostructures & Applications, Nonlinear & Ultrafast Optics, Nuclear Physics & Engineering, Optical Communications & Systems, Optoelectronics Devices & Applications, Organic Materials, Devices & Applications, Physical Chemistry & Biochemistry, Plasma, Discharge Physics & Applications, Quantum Physics & Spectroscopy, RF & Digital Communications, Semiconductors & Devices, Simulation & Modeling Research, Solar Energy & Devices, Solid State Physics & Applications, Structure & Properties of Matter, Superconductivity & Related Devices, Surfaces, Interfaces & Films, Thin Films & Applications, and Vacuum Science & Technology.

The first issue contains 7 letters, while the second issue released in September 2008 contains 6 letters only. However, the editorial board chose to continue publishing IJAPLett in order to give a better chance for Iraqi and foreign researchers to submit their short articles for publication after reviewed according to the same reviewing standards of IJAP. Therefore, 3 issues were released in January, April and October 2009 containing 8, 5 and 10 letters, respectively. The idea of IJAPLett was appreciated and admired by the community of applied physics in Iraq.

In January 2010, the first issue of the third volume of IJAPLett was released containing 6 letters. Surprisingly, the promotion committees in some Iraqi universities decided not to consider the letters published in IJAPLett as a published articles and hence not accepted for academic promotion for Iraqi faculty members. Accordingly, the rights of authors of these letters would be taken for no logical reason. Therefore, the editorial board decided to stop publishing IJAPLett in April 2010 and transferred all accepted letters to IJAP for publication.

With the exceptional success of IJAP to attract researchers from inside Iraq and abroad to publish their research works as well as the progress to propose IJAP for Scopus index, which was happened in July 2021, the Editorial Board found that the existence of IJAPLett to publish the letters on the disciplines mentioned before is a requirement. Therefore, the decision to re-publish IJAPLett was not late and taken in September 2020. IJAPLett returned back with the first issue of volume 4 released in January 2021 containing 6 letters. By December 2021, 4 issues of this volume were released. Similarly, 4 issues of volume 5 were released in 2022. The editorial board of IJAPLett was re-configured to include experts and professors from different Iraqi universities and of different fields of specialty in order to introduce it for as many as possible researchers.

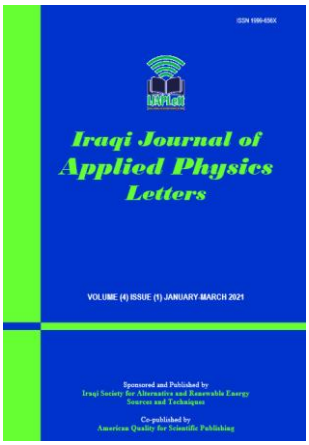

In December 2022, IJAPLett (ISSN 199-656X, eISSN 2958-6488) was proposed for Scopus index as it has satisfied the scientific, technical and administrative requirements for this step. Even though, IJAPLett will keep published to provide a fast and extended platform for the research works on applied physics and related disciplines.

IJAPLett receives the original contributions to be published at the mailing address:

P. O. Box 88052, Baghdad 12631, IRAQ
Website: www.iraqiphysicsjournal.com
Emails: editor@iraqiphysicsjournal.com
editor_ijap@yahoo.co.uk
ijaplett.editor@gmail.com

IRAQI JOURNAL OF APPLIED PHYSICS

Volume (19) Issue (1) January-March 2023

CONTENTS